Next Generation Inverters Equipped with Virtual Synchronous Compensators for Grid Services and Grid Support

Doctoral Dissertation
Doctoral Program in Electrical, Electronic and Communication Engineering
(XXXIII cycle)

Next Generation Inverters Equipped with Virtual Synchronous Compensators for Grid Services and Grid Support

Fabio Mandrile

* * * * *

Supervisors
Prof. Radu Bojoi, Supervisor
Prof. Eric Armando, Co-supervisor

Politecnico di Torino
January 4, 2021

I hereby declare that, the contents and organisation of this dissertation constitute my own original work and does not compromise in any way the rights of third parties, including those relating to the security of personal data.

. . . . . .

Fabio Mandrile

Turin, January 4, 2021

Summary

The technological advancements and the decarbonization requirements have pushed towards generating more electricity from renewable energy sources and the transportation electrification. This guarantees a more sustainable energy sector, but it also has a heavy impact on the grid infrastructures. In fact, the shift from a synchronous generators (SG)-based electricity production towards static converters is impairing the stability of the grid. For this reason, it is important to find out new control strategies for power converters, which can guarantee a seamless substitution of the traditional SG-based generation.

A promising technology is the emulation of SGs using virtual synchronous machine (VSM) algorithms. This would enable static converters provide the so-called ancillary services (frequency regulation, reactive support...), which are necessary to the correct operation of the electric power system.

The goal of this thesis is, therefore, to propose a VSM model called Simplified Virtual Synchronous Compensator (S-VSC), which can provide each of these ancillary services. This dissertation first presents an overview of the existing VSM strategies and then describes and experimentally validates the S-VSC. Finally, a state-space modeling technique, called component connection method, is extended and applied to the S-VSC model, in order to obtain a simulation model that can be used to analyze larger power systems with an high penetration of power converters.

Acknowledgements

I will start from the gratitude to my supervisor Radu and my co-supervisor Eric, who are there every time I need them (even at weekends!) and have stimulated me with many enriching projects beyond my PhD activities. Then, I would like to express a heartfelt thanks to prof. Carpaneto, who gave me an important technical guidance beyond his duties during my PhD.
I am also grateful to Aalborg University and in particular to Frede and Tomislav for hosting me during my exchange period there. Their guidance has been very precious.
Thanks to all the people I have worked with during the last three years: my fellow colleagues (both in Torino and in Aalborg), from whom I have learned so much, and the master students, who helped me with their theses. Finally, a special "thank you" to my friends and family, who have been supporting during all my PhD.

"Dipinte in queste rive
son dell'umana gente
le magnifiche sorti e progressive"

G. Leopardi

Contents

List of Tables

List of Figures

Chapter 1

Introduction

Thanks to the favorable properties of electrical energy, its easy transmission and transformation, modern societies strongly rely upon it in every sector: industrial, commercial and residential. Typically, electrical energy is obtained from a primary energy source (e.g. fossil fuels, water energy or nuclear energy) using synchronous generators (SGs), transmitted and then delivered to the final user through the electric power system.

The power system was initially designed, as depicted in Fig. 1.1, for a traditional centralized generation and distributed load structure, where the generation units were large thermal or hydroelectric plants, located as close as possible to the primary energy source (i.e., rivers, dams, sea) to optimize the energy production process.

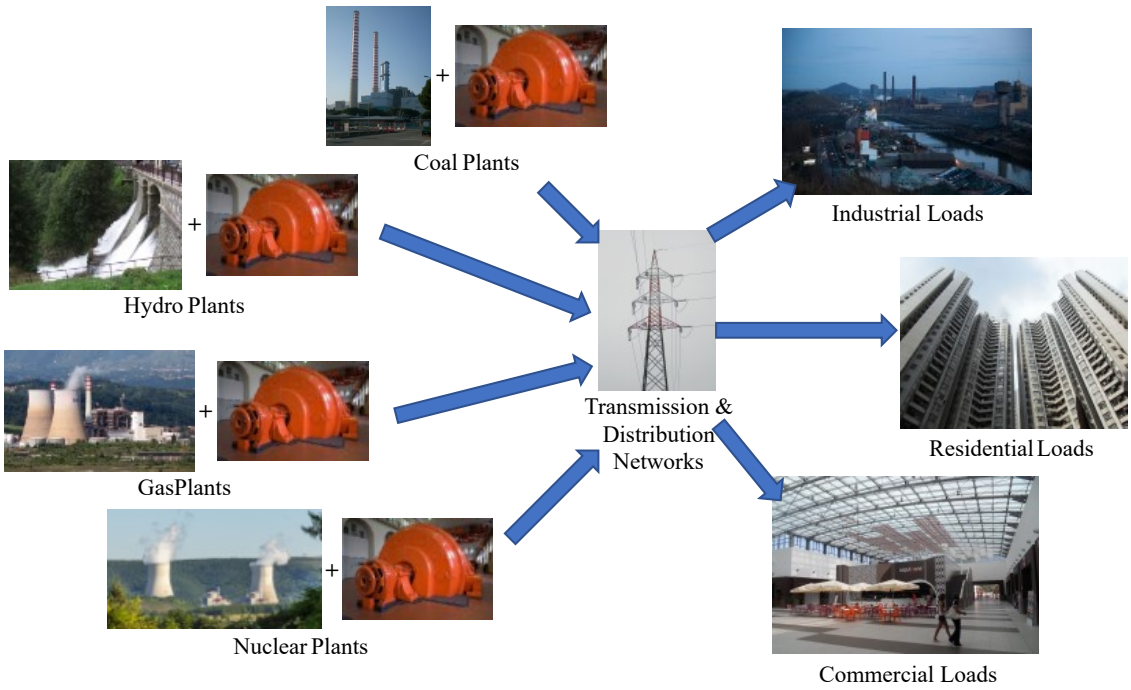

Figure 1.1: Structure of traditional power systems. Pictures from Wikimedia Commons.

Under this paradigm, the generation of electricity can be programmed by acting on the primary energy source and the power is then delivered in ac through the highly efficient transmission lines and transformers to each and every load that requires it (i.e., industrial customers, residential and commercial loads).

This paradigm have been applied for roughly a century and it is still prevalent. However, in the last decades, thanks to the technological advancements in renewable energy technology (efficiency of solar panels and the exploitation of wind power) and the run for decarbonizing the energy sector, the traditional power system architecture have experienced a radical modification, converging to the structure shown in Fig. 1.2. This modern structure still features large centralized generation plants, but with a reduction of traditional power sources, such as fossil fuels and nuclear power [1], in favor of renewable energy sources, such as wind and solar PV. Moreover, also numerous smaller distributed prosumers (i.e., electricity users and providers at the same time) have been spreading. These prosumers are the traditional final electricity users, who have integrated a local generation system, such as rooftop solar panels or cogeneration units for both heat and electricity production. This modifies the active power flows at system level: from the old paradigm of unidirectional power flow from the generation to the loads, through the transmission and distribution networks, to the contemporary bidirectional power flow, where both centralized and distributed generation are feeding the energy transmission network.

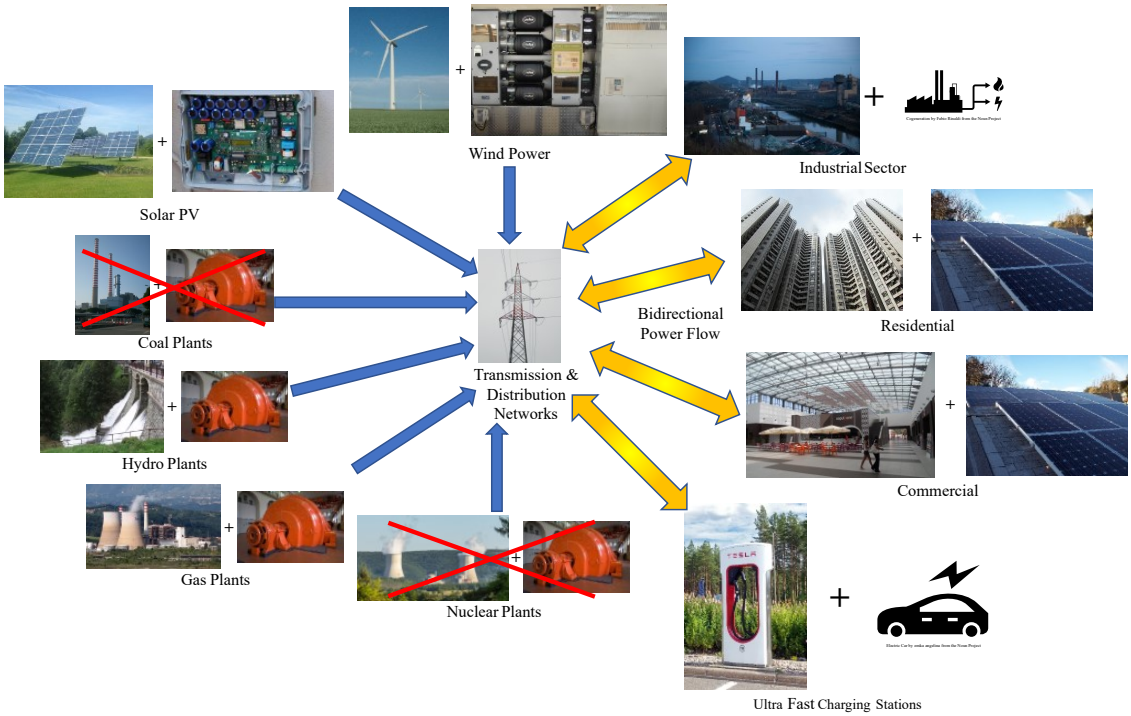

Figure 1.2: Structure of a modern power systems. Pictures from Wikimedia Commons.

Another paradigm shift is the transportation electrification. In the present years, the terrestrial mobility is shifting towards electric or hybrid propulsion, therefore requiring the installation of charging networks for electric vehicles. This means that a large number of electronic loads will be connected to the grid, ranging from the reduced power on-board-chargers (few kW) up to the recent fast or ultra fast chargers (charging power up to hundreds of kW) to quickly recharge electric cars while covering long distances. This faces the grid with new challenges in terms of active power delivery and consumption, but it also represents an opportunity for distributed storage systems and compensators, thanks to the vehicle to grid (V2G) technologies.

While the electrical layout has changed, the operation of the electrical power system still follows the original arrangement. The grid management is structured in a hierarchical structure, as represented in Fig. 1.3. This control structure is organized in three layers:

Primary control layer: this is the innermost control layer and it operates at unit level. It represents the frequency/excitation control of synchronous generators in traditional power plants or the inner current/voltage controllers in power converters. This layer is usually implemented as a standalone controller, not interacting with the other generation units. This layer features short time constants and operates in the time span of seconds or less (ms for power converters);

Secondary control layer: this second layer is in charge of the integral regulation of voltage and frequency for a given electrical region (e.g., a country). This regulation is performed by a centralized measurement of frequency (whole region) and voltage (several key nodes) and a centralized controller which feeds the power references to the controlled units. This secondary layer is slower than the primary and operates in the span of minutes;

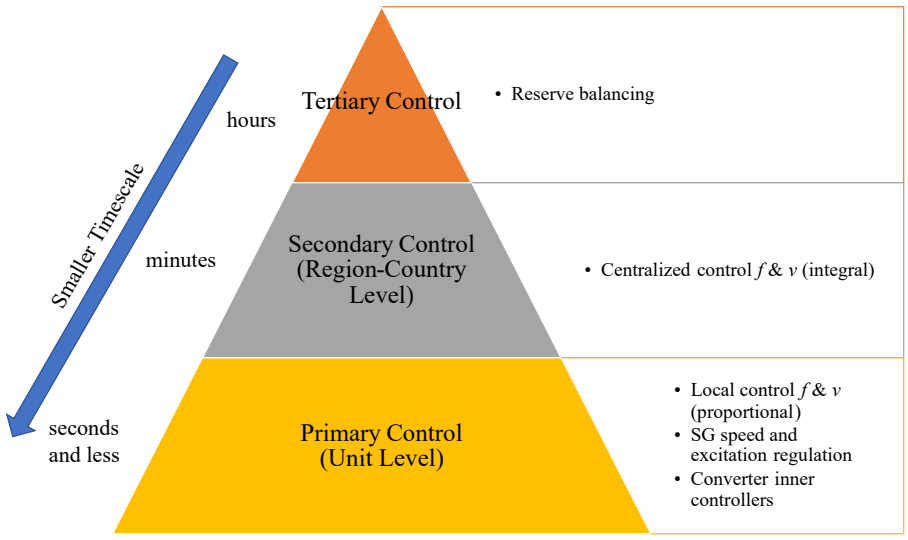

Figure 1.3: Hierarchical control of power systems.

Tertiary control layer: the uppermost layer is in charge of the slow modifications of the active and reactive power generation planning, with the goal of restoring the power reserve of the generation units. This is the slowest regulation. It is performed manually by the grid operator and it operates in the hours time span.

In summary, the modern power systems are, on one hand, becoming very different from the past from the hardware point of view, as the power flows are inverting and the way electricity is generated is shifting towards renewables. On the other hand, however, its control structure and the relative experience must be preserved, as it would be impossible to operate a radical modification of the power systems from their roots.

It seems obvious the necessity to find new ways of integrating the new energy sources and the distributed generation paradigm into the existing grids, by slightly altering the existing control paradigm (e.g. tuning of the control layers) and adapting it to the new reality. This goal can be achieved by emulating SGs using static converters.

Therefore, this thesis deals with the emulation of synchronous machines with power converters. The motivation of this research lies in the rising amount of inverter-based energy conversion connected to the electric grid, in particular power generation from renewable energy sources (RESs) and charging stations for electric vehicles (EVs) and the consequent issues from the power system perspective (lack of inertia, harmonics...).

In this introduction, which are the required SG features and why it is necessary to implement them will be explained. Moreover, the relevance of this research topic will be corroborated with data on the market of both renewable generation and electric mobility. Finally, the main contributions of this research and the detailed outline of this thesis will be presented.

1.1 Ancillary Services for the Power System

The design and structure of contemporary electric power systems find their roots in a more than a century old paradigm [2]. This paradigm relied on a centralized power generation from programmable sources (e.g., coal power plants), through SGs, using the transmission lines and distribution networks to deliver the energy in a unidirectional way to the ac loads (i.e. motors, lamps, heaters...).

Therefore, the correct operation of such power systems was designed around the synchronous generators. This meant that the quality indicators in power systems were defined starting from the behavior and control of these synchronous machines.

These indicators are [2]:

- A constant frequency (e.g., 50 Hz or 60 Hz);
- A constant voltage amplitude;
- Protection of the system in case of faults;

- A sinusoidal voltage supply with low harmonic content and limited harmonic interactions.

The SGs were, and still are, able to support and preserve these indicators, by providing the so called ancillary services.

In the following sections, these services will be described more into detail. Moreover, the differences between traditional SGs and modern power electronics-based generating plants from the grid perspective will be highlighted.

1.1.1 Frequency Control and Inertia

The first power grid quality aspect is the constancy of the frequency. As it is designed, the power system guarantees the equilibrium between the active power demand and its consumption by keeping the grid frequency close to its nominal setpoint [3]. Moreover, it is also important to keep the grid frequency within the given specifications to ensure the correct rotational speed of electrical machines directly connected to the grid, which are still widespread in industrial applications.

This frequency regulation, during load transients (load increases or generation decreases), is performed by SG-based plants into three sequential phases, as depicted in Fig. 1.4.

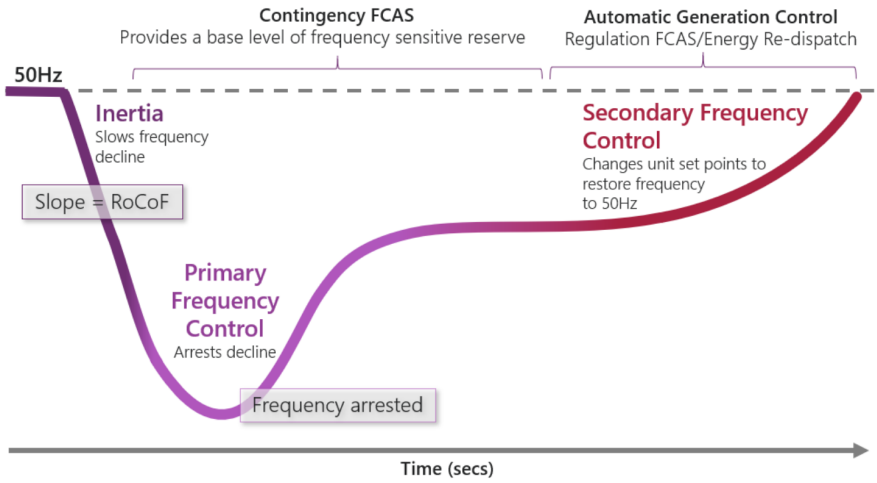

Figure 1.4: Frequency profile and frequency control intervention after a generation reduction. Extract from [4].

In the first instants of the unbalance, the SGs automatically accelerate or slow down to counteract the frequency variation (inertial effect). This way, the variation of their kinetic energy is employed to reduce both the maximum frequency variation and the rate of change of frequency (RoCoF), i.e., the frequency derivative.

After this first phase of the transient (few seconds), the primary regulation of the frequency (proportional frequency control) comes into action (minutes timescale). The generating units which feature this optional service modify their operating point (active power injection) and contribute to restore the correct frequency setpoint.

Finally, in the span of tens of minutes, the frequency of a grid portion (e.g., a country) is restored to its setpoint by the secondary frequency control, which is a centralized integral control, setting the active power references of the generation units taking part to it.

In case of severe faults (too large or too fast frequency variations), the power systems are equipped with frequency protection relays. These relays monitor both the absolute value of the frequency and its derivative and automatically disconnect loads (load shedding) and generating units in case of severe faults, trying to preserve the correct grid frequency and protecting the electrical equipment.

On the other hand, electronic converters do not automatically provide these features. Regarding the inertial effect, being static without moving parts, there is no kinetic energy available to inject or rotors to accelerate to counteract sudden frequency variations. Moreover, power converters behave as constant power sources (e.g., PV plants) or loads (e.g., EV charging stations) with non-programmable power setpoints. In fact, speaking of power generation from RESs, the converters are controlled according to a maximum power point tracking (MPPT) logic [5], with the goal of exploiting the RES as much as possible. With regard to electronic loads, they always absorb the needed active power, independently on the frequency and the voltage level of the grid (within rated conditions). This latter aspect means that no primary nor secondary regulation of the frequency is compatible with the MPPT logic, since the active power setpoints do not depend from the plant operator but from the RES available power.

For this reason, recent grid codes prescribe clear requirements for the RES converters connected to the grid regarding the frequency control [6–8]. Specific active droop curves are provided, as the example of Fig. 1.5. These curves prescribe different droop coefficients (in the range 2–5 %) for different frequency ranges. Besides, to reduce the sensitivity of the droop controller to very small frequency variations, a deadband is usually implemented around the nominal grid frequency.

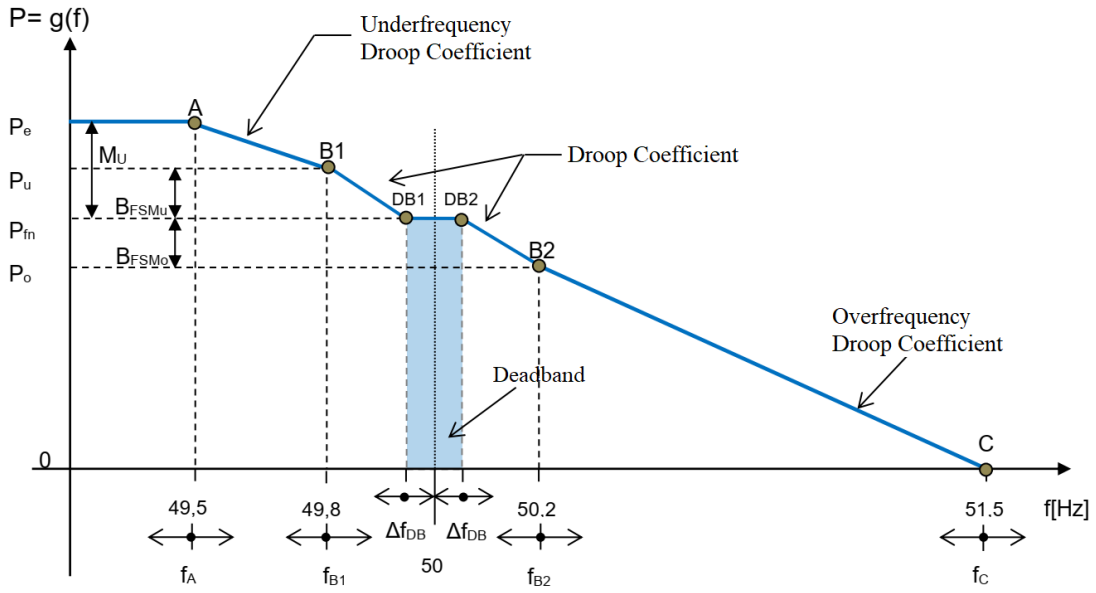

Figure 1.5: Example of power-frequency curve for a PV plant. Extract from [6].

Moreover, inertial action is currently mandatory for wind turbine interfaced to the HV grid [6, 9] and it can be obtained by exploiting the wind turbine rotor. This is not the case for PV plants, where no mechanical parts are involved and some kind of energy storage must be employed (e.g., batteries, capacitors...) [10].

The key concepts of frequency control and how RESs differ from SGs can be summarized as follows:

- The grid frequency and its constancy is a key quality aspect for power systems;
- SGs preserve the grid frequency leveraging their rotor inertia and the modification of the active power setpoints of the primary generating units;
- Too severe or too fast deviations from the frequency setpoint may lead to the interruption of the supply;
- Converters do not embed inertial capabilities;
- RESs and electronic loads as fast-charging stations are not programmable and their power flow is not modified according to a frequency regulation logic;
- Contemporary grid standards are prescribing precise frequency regulation coefficients and require inertial action from wind turbines.

Case Studies

The difficulties of integrating RESs into the electric grid have been confirmed by several power outages, which can be partially imputed to the non optimal or wrong behavior of power converters. It is of interest mentioning two recent exemplary cases taken from the Australian power grid, which demonstrate the impact of state-of-the-art RES plants connected to the grid. These outages are useful to analyze the really necessary features for grid-tied converters and corroborate the need of more advanced control techniques for inverters, such as the emulation of SGs.

The first example is the South Australia (SA) blackout, dated 26th September 2016. From the technical analysis of this fault [11], the following chain of events emerged:

1. Atmospheric events caused a sequence of six voltage dips over a two-minutes period;
2. Nine wind farms reduced their power generation, as their control system could only withstand a limited number of voltage dips in that period span;
3. The generation reduction led to a larger power import towards SA and the consequent overload trip of the interconnection with the Victoria region;
4. The load shedding protections failed to trip, due to the too fast decay of the frequency (see the profile in Fig. 1.6);
5. The SA blackout occurred as the power balance could not be maintained.

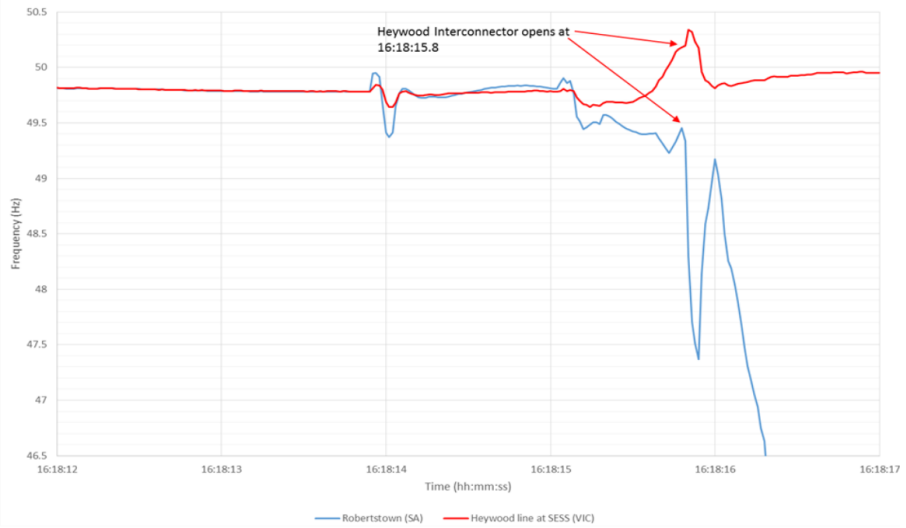

Figure 1.6: Frequency profile after SA grid separation. Extract from [11].

From this event, two main conclusions [11] are drawn:

1. RESs plants must be equipped with suitable controllers, able to withstand multiple fault events;

2. A larger inertia is necessary. This would limit the RoCoF and enable the protection relays to intervene.

The second example is a recent grid separation fault (4th January 2020), which happened again in the Australian network [12]. In this case, the severe bushfires which afflicted Australia in the summer caused an outage of multiple 330 kV transmission lines. This led to a grid separation between the regions of Victoria and New South Wales. In this case, the grid separation did not lead to a black out in either regions as it happened in 2016 and the frequency could be maintained within the specifications, as reported in Fig, 1.7. However, this fault highlighted that at least 40–50 % of the distributed PV systems did not behave according to the most recent Australian technical standards and tripped untimely. This means that the technical standards for distributed PV units must be improved under the aspect of fault ride-through capabilities and a more accurate verification of the actual fault ride through (FRT) capabilities is necessary.

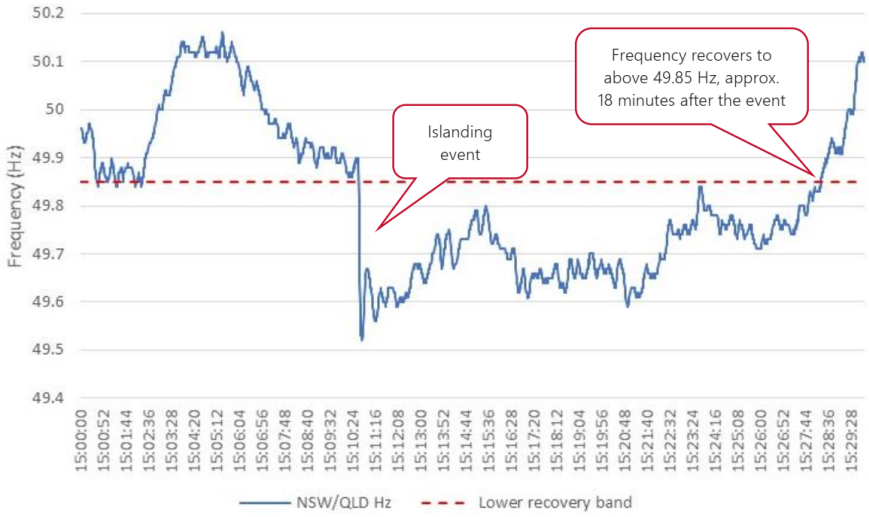

Figure 1.7: Frequency profile of the Victoria–New South Wales grid separation. Extract from [12].

1.1.2 Voltage Regulation - Static Voltage Regulation

The second cornerstone of power systems is the constancy of the voltage level. The amplitude of the voltage must be kept within the standard prescriptions [13] and its variation is strongly related to the reactive power (at least in mainly inductive networks).

To accomplish this task, there are several options, which operate the so called static (steady-state, long term) voltage regulation:

- Voltage regulation of the generation plants;
- Variable ratio transformers and autotransformers;
- Capacitive and inductive compensators.

Dealing with the generation aspect, this thesis will focus only on the first solution. Also in this case, there are several layers of regulation. The first layer operates on single generating units. SGs are equipped with an automatic voltage regulator (AVR), which directly operates on the excitation of the machine, so that their terminal voltage tracks its reference. This first regulation layer can also receive extra signals, such as from a power system stabilizer (PSS) to compensate the voltage drop of the interconnection transformer or provide damping of the electromechanical oscillations of the rotors [2, 14].

The second level of regulation is a centralized voltage regulation, controlling the voltage level at key grid nodes, representative of their regions. This secondary control operates the static compensators and shares the reactive power load among the generating units.

This is again designed for SGs units. They can in fact modify their operating point to exchange reactive power with the grid within the limits of the so called capability curves [2]. In this case, static converters can be equipped (and are, according to the technical standards [6–8, 15, 16]) with suitable control techniques in order to implement the required capability curves. Such curves, as the example of Fig. 1.8, prescribe the reactive power (per unit of the plant maximum power) that must be injected depending on the converter terminal voltage. Referring to Fig. 1.8, the generation unit is not simply asked to inject active power, but must be able to operate in any point of the red region, according to the specific reactive power/voltage law ($Q = f(v)$) given by the grid operator.

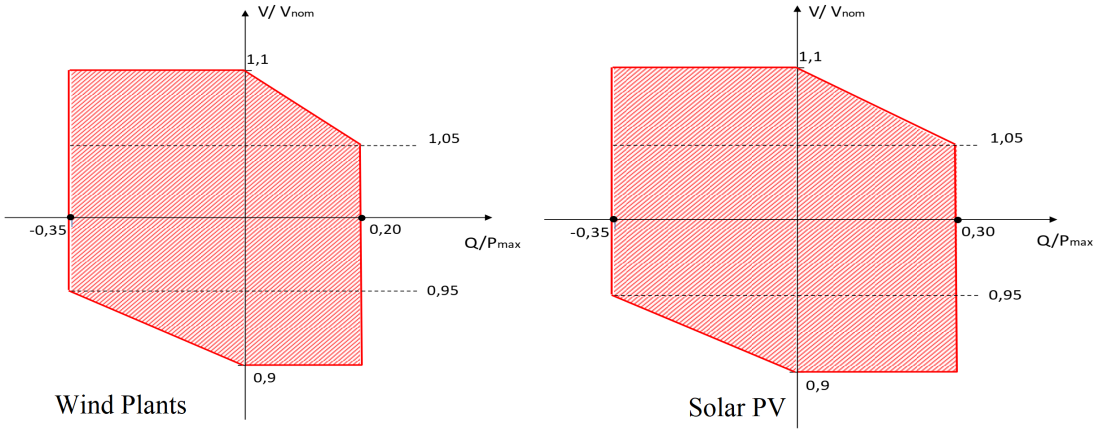

Figure 1.8: Example of reactive capability curves for a wind and solar PV unit connected to the HV grid. Extract from [6, 7].

To summarize:

- Static voltage stability depends on the reactive power equilibrium;
- SGs are equipped with AVR and must be able to inject/absorb reactive power according to capability curves;
- Also static converter plants (e.g., PV) must be able to exchange reactive power with the grid according to capability curves, defined by the technical standards.

1.1.3 Voltage Regulation - Dynamic Voltage Regulation

The structure of the power system must withstand and clear short circuits. This means that the transmission and distribution networks are protected by breakers (e.g., equipped with overcurrent relays) to isolate faulty branches of the network and clear the fault.

Again, SGs are appropriate to trigger such protections. In fact, in case of voltage reductions at their terminals (as it happens when there is a short circuit in the network), they automatically inject a fault current. Depending on the electrical distance from the point of fault (i.e., depth of the voltage reduction at the machine terminals), they inject a larger or smaller peak current. For near faults, they can easily inject a short circuit current few times larger than their rated value (e.g., 4–5 pu) without incurring into thermal protections, thanks to their long thermal time constant. Therefore, they are able to remain connected to the grid and ride through the fault and support the grid in abnormal conditions.

On the other hand, power converters must first be equipped with suitable control strategies to detect a fault condition, generate the correct current references [5] and ride through the fault, according to the technical requirements [6–8]. Secondly, due to the much shorter thermal time constants, they cannot be overloaded and can only inject their rated current, even for short transients. Finally, generating units also have a key role during asymmetrical faults. Such faults are the most common and require fault current both in the positive and negative sequence to attenuate the overvoltages on the healthy phases. Again, SGs feature FRT capabilities and can provide positive-negative sequence current to satisfy these requirements, while static generation plants must be equipped with more complex control strategies if required to provide such behavior [5, 17]. Therefore, the rising installed capacity of power generation has pushed the transmission system operators (TSOs) to introduce more strict regulations to interface new plants to the grid. As an example, the Germany grid code VDE-AR-4120:2018 [8] prescribes that power generating modules must ride through symmetrical and unsymmetrical grid faults and provide dynamic reactive current support both in the positive and negative sequence for an arbitrary sequence of multiple faults.

To synthesize the dynamic voltage regulation aspect:

- The grid is equipped with protections against short circuit faults;
- SGs trigger these protections by injecting large short circuit currents (4–5 times the nominal current);
- SGs can ride through symmetrical and asymmetrical faults and can inject positive and negative sequence fault current;
- Static converters cannot inject large short circuit currents (no overload);
- Static converters require additional control algorithm to guarantee the FRT requirements and the injection of positive and negative sequence currents;
- Recent grid codes are requiring more stringent performance from static converters, forcing the implementation of advanced fault control techniques.

1.1.4 Harmonics

The electric grid requires a sinusoidal voltage with low distortion in steady-state conditions [13]. In fact, the presence of harmonic and interharmonic components [18] in the supply voltage may lead to the following detrimental effects:

- Additional high frequency losses in electrical equipment and/or loads (e.g., transformers, motors...);
- Worse performance of electric motors and generators directly connected to the grid;
- Poorly (or non-) damped resonances between different components connected to the same grid;
- Disturbances in electronic equipment;
- Unwanted intervention of protection devices (e.g. breakers).

Therefore, it is important to avoid injecting harmonics into the grid and to compensate any harmonic content as much as possible.

Thanks to their electromechanical construction, SGs are able to generate a voltage with a very low total harmonic distortion (THD) and are, therefore, highly suited to this purpose. Moreover, they are able to inject harmonic current when supplied with distorted voltage, as their stator offers a low impedance path to frequency components other than the fundamental.

On the other hand, electronic converters generate a wide spectrum of frequencies, related to the switching of the power transistors, their control strategy and to the resonance frequency of the grid side filters. They are, therefore, more prone to underdamped high

frequency oscillations, as demonstrated by the accidents reported in Fig. 1.9 [19] and [20].

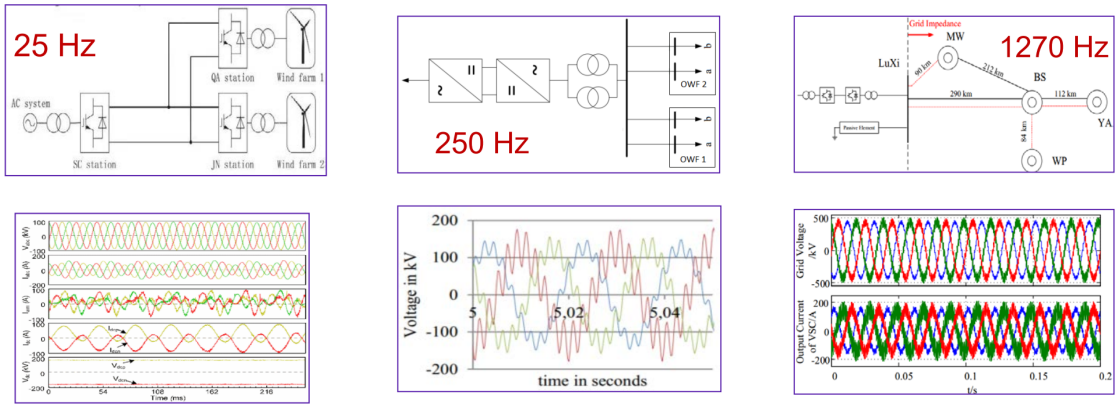

(a) (b) (c)

Figure 1.9: Reported wideband oscillations in power systems with power electronics converters. Source [19]. From left to right:
a) Low frequency oscillations. Nanao, China, 2013;
b) Medium frequency oscillations. Borwin, Germany, 2009;
c) High frequency oscillations. Yunnan, China, 2017.

Moreover, electronic loads (e.g. thyristor or diode rectifiers) distort the grid voltage, due to their harmonic current absorption. For these reasons, power converters must be equipped with suitable controller so that they do not amplify resonances and can also compensate the harmonic distortion generated by the loads.

For these reasons, there is a growing interest in the modeling and control of the harmonic emissions and interactions of converters (in particular wind turbines [21], as reported in Fig. 1.10) in order to standardize the harmonic modeling and their integration at power system level. Moreover, grid operators are already requiring simulation models of the single generating plants for simulation purposes [6, 7].

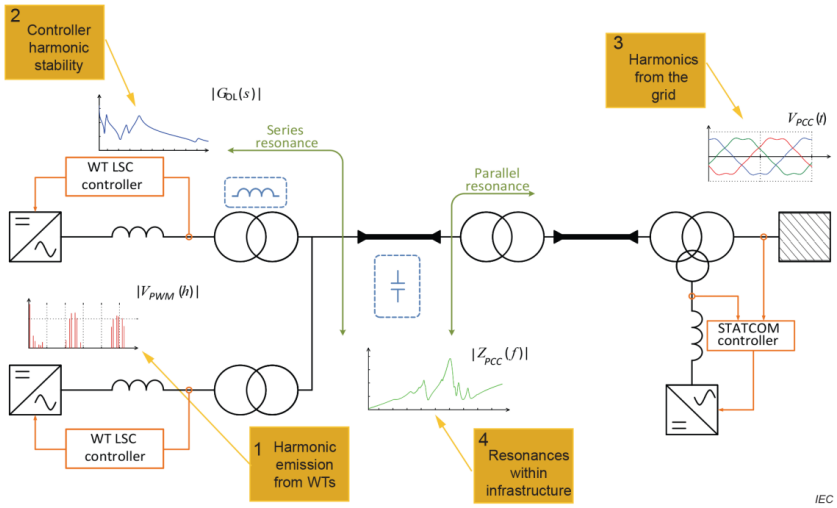

Figure 1.10: Example of wind power plant components for harmonic studies. Extract from [21].

In summary:

- A sinusoidal supply with limited harmonic content is necessary for the correct operation of the grid;
- SGs do not generate high frequency harmonics and contribute to compensate them;
- Harmonic components may lead to adverse interactions among grid connected converters;
- Technical standards are regulating the harmonic modeling and the harmonic requirements of generating power plants [6, 7, 21].

1.2 The Role of Virtual Synchronous Machines

As mentioned before, a particularly promising technology is the SG emulation using virtual synchronous machines (VSMs) [10]. This means that, thanks to its VSM control algorithm, an electronic power converter provides one or more of the features of a real SG, therefore supporting the grid providing the aforementioned ancillary services. This idea is graphically represented in Fig. 1.11.

In this section, a brief overview of the possibilities of the VSMs will be carried out.

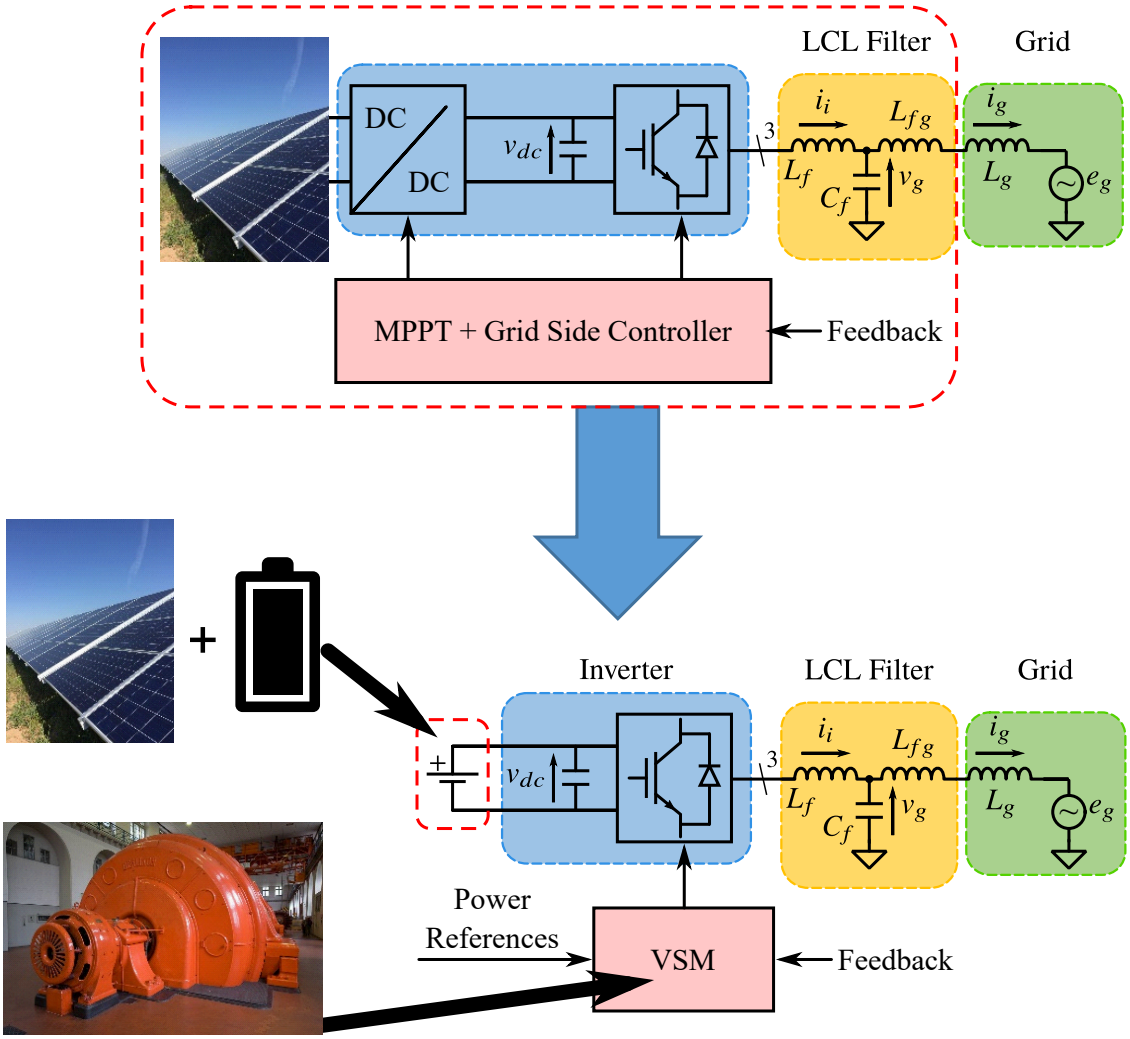

Figure 1.11: Simplified diagram of the VSM concept: the RES converter is transformed into a VSM with a suitable control algorithm.

The first aspect that can be emulated by a converter is the inertial action of a SG. Since there are no rotating parts, this feature is called virtual (or synthetic) inertia and it is defined as an active power injection, negatively proportional to the grid frequency derivative (RoCoF) [22]. In most models, this feature is obtained by implementing the so called swing equations of SGs [2]:

$$P_m - P_e = 2H\frac{d(\omega_r - \omega_g)}{dt} + D_p(\omega_r - \omega_g) \tag{1.1}$$

where P_m is the mechanical power at the machine's rotor, rotating at ω_r, P_e is the electrical power generated by the SG; the grid frequency is ω_g. The machine is characterized by the inertia constant H and the damping coefficient D_p.

This equation let the control model generate an additional inertial power term as follows:

$$P_{inertia} = -2H\frac{d\Delta\omega_r}{dt} \tag{1.2}$$

therefore, satisfying the balancing needs of the power system in the very first instants of a power imbalance.

From the energetic point of view, it is necessary to provide such additional power from the converter dc side. This power cannot be in fact obtained from a mechanical rotor as in real SGs. Only when dealing with wind turbines, this additional power can be absorbed from the kinetic energy of the turbine rotor; on the other hand, solar PV plants require either the curtailment of the PV power, or the integration of some kind of storage system on the DC side. It must be noted that this storage system does not need a high energy content, as it only operates transiently (few seconds) and can be recharged more slowly.

As seen in section 1.1, not only inertial behavior, but also frequency regulation is required from RES converters. In this case, the control strategy is much simpler, as a simple proportional frequency control can be added to generate the suitable power references. However, a larger reserve is necessary, compared to the inertial action. While the power injection is limited (few pu of the rated power), the duration of this injection is prolonged in time, requiring again power curtailing strategies during ordinary operation or the integration with energy storage systems.

On the other hand, the other grid ancillary services (voltage regulation and harmonic control) do not require the integration of energy storage systems (neither long nor short term) as they deal with reactive power exchange. In this case, the critical part is represented by the AC converter itself, which must be rated to carry both the rated active power flow and the necessary reactive power exchange, leading to a global oversize of the switches (larger current rating) and the dc-link capacitors. Regarding the control part, suitable algorithms are available for both the reactive power control [5] and the filtering action [23]. In this matter, VSMs can provide the reference signals for such regulators, by implementing a virtual excitation control, regulating the voltage at the terminals of the machine. Moreover, the virtual stator, if implemented correctly, can generate the necessary current references to compensate the voltage harmonics in the grid.

1.3 An Outlook on Renewable Energy Sources and Fast Chargers

After having described the needs of the power systems and the criticality of electronics power converters connected to the grid, it is interesting to provide figures of the market and penetration of such converters into the grid. The last decades have, in fact, witnessed a strong increase in the grid applications of power electronics converters. In particular,

the advancements in power electronics technology enabled the electrification of two key sectors: energy generation from renewable energy sources and electric mobility.

The first market of interest is the energy generation from renewable energy sources, such as solar PV and wind. Only these two sources are considered in these thesis, as they are mainly interfaced to the grid by means of a power electronics converter. Starting from Fig. 1.12, it is clear that the installed solar PV and wind power capacity has been rising in a nearly exponential way. This rise means that larger and larger shares of the electricity consumption will be covered by this technology. For solar PV, this coverage is already significant in some countries (i.e., Italy and Germany), reaching almost 10 % of the electrical energy consumption, as shown in Fig. 1.13.

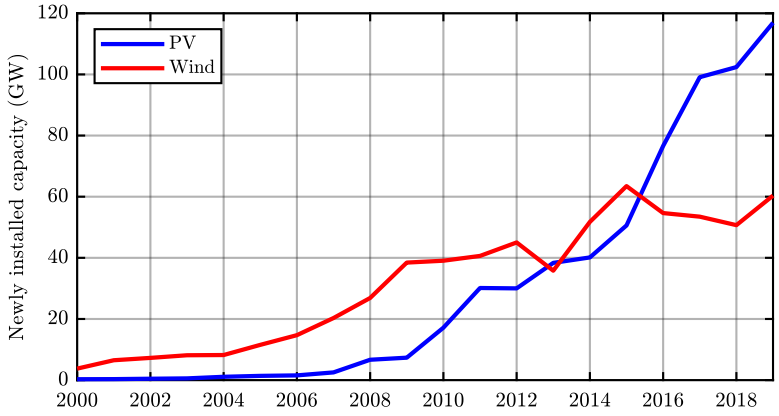

Figure 1.12: Worldwide newly installed solar PV [24] and wind [25] capacity in the years 2000–2019 .

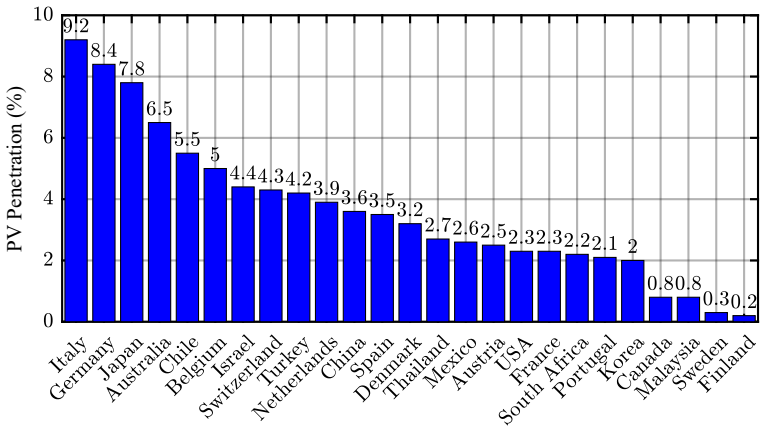

Figure 1.13: Share of electricity consumption covered by PV power in 2018 [26].

The second emerging market is the electric mobility one. The amount of EV sales is foreseen to rise steadily (as shown in the statistic of Fig. 1.14) in the next decade. As a consequence, fast and ultra fast chargers (UFCs) for electric vehicles (including AC 43 kW chargers, DC chargers, Tesla Superchargers and inductive chargers) installations have been rising almost exponentially in the past few years, as it emerges from Fig. 1.15. This market is at the moment uniquely considered as a load connected to the grid. However, it provides great potential for VSM applications. In fact, each charging station is interfaced to the grid by a converter and usually features a local storage system for peak load shaving. If such converters were properly designed (bidirectional power flow), they could greatly improve the quality of the grid, acting as distributed static compensators, providing partially or fully the grid services mentioned in section 1.1.

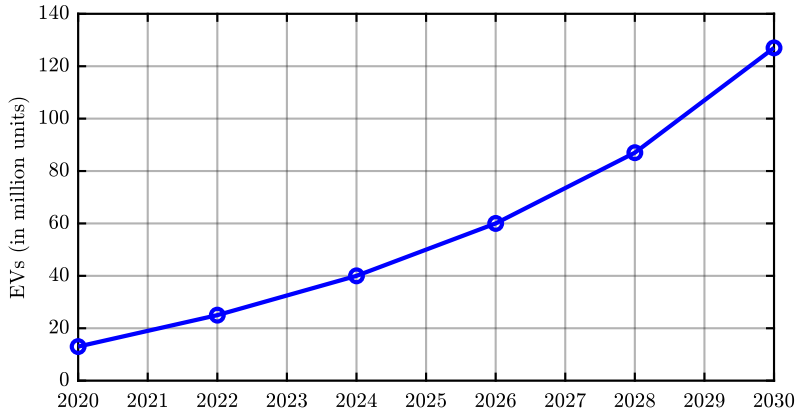

Figure 1.14: Forecast of the EV sales in the years 2020–2030 [27].

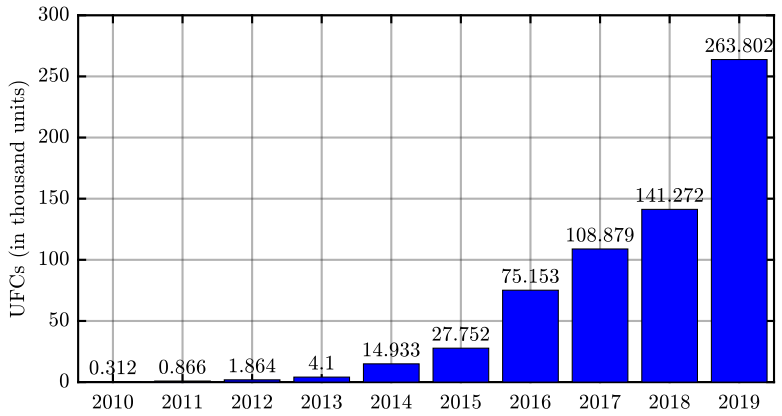

Figure 1.15: Cumulative number of fast chargers installed worldwide in the years 2010–2019 [28].

This dramatic increase in the electrification is opening up many new challenges for both power electronics designers and power system operators, in relation to the grid requirements and reported accidents of section 1.1. Moreover, due to ecological and safety reasons, many countries are reducing the share of generation from synchronous machines. A key example in this direction is Germany, which planned to close nuclear power plants by 2022 [1] and coal power plants by 2038 [29]. As it can be seen in Fig. 1.16, Germany is still strongly dependent on coal and nuclear power (a total of 47% of the electrical energy production). Therefore, the only viable way to accomplish these decarbonization goals is to strongly increase the generation from both natural gas (SG-based) and from renewables such as wind and solar PV (today covering 35 % of the production). **However, in order to seamlessly integrate the new installed power capacity it will be necessary to include smarter control strategies, such as VSMs.**

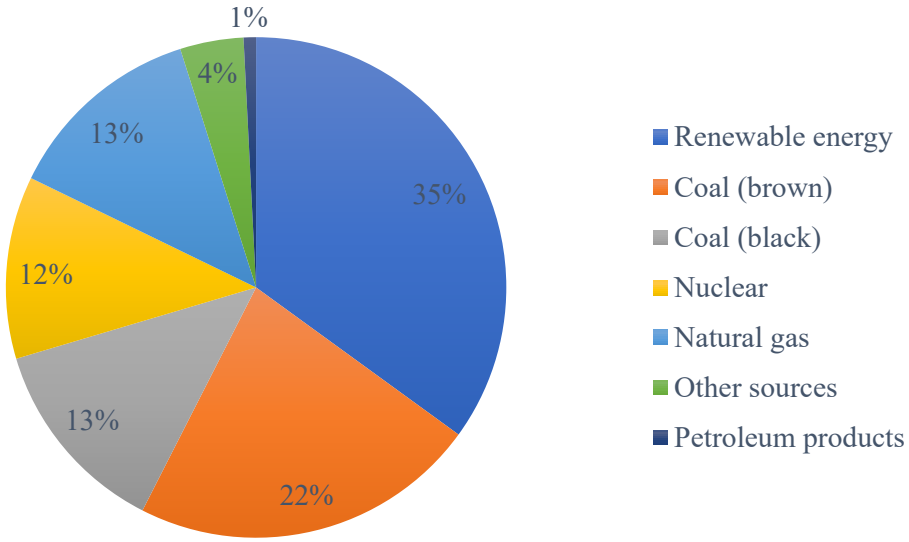

Figure 1.16: German electrical energy sources mix for the year 2019 [30].

1.4 Goal of the Thesis and Research Contributions

This thesis deals with the analysis, implementation and validation of a new VSM model called Simplified Virtual Synchronous Compensator (S-VSC). The goal is to develop a parallel VSM structure, only providing ancillary services to the grid.

1.5 Thesis Outline

The main results and novelties of this research are summarized as:

- The S-VSC model is intended as a plug-in for a traditional grid-feeding, current controlled inverter, as the majority of the RES converters and fast chargers. The

advantage of this solution is the easy current limitation and the larger control bandwidth, compared to a voltage-controlled inverter.

- The S-VSC generates additive power contributions to the inverter references, to guarantee grid services (inertia emulation and compensation of current harmonics) and grid support during symmetrical and asymmetrical faults with reactive power only. In the literature, however, the virtual machines are always in charge of processing the full power references. Therefore the S-VSC always operates at low load, featuring higher transient stability and damping;

- The damping of the S-VSC is done using only an equivalent q-axis damper winding. Therefore, the damping is fully independent and decoupled from the primary regulation of the frequency. Full dampers model have already been used in some models. In the proposed model, a simplified damper is adopted, in order to ensure the same performance, but at a reduced complexity;

- A focus on the harmonic compensation capabilities of VSMs and their experimental assessment for the proposed S-VSC model;

- The extension of system level state-space modeling techniques for advanced controllers of power converters using the component connection method (CCM) applied to the S-VSC.

This thesis is divided into 5 chapters as follows:

Chapter 1 : Introduction to the issues of power generation from renewable energy sources and challenges of a power electronics-based power system. Review of the ancillary services needed by the grid and the relative grid standards;

Chapter 2 : State of the art of SG emulation strategies: presentation of the models and comparison;

Chapter 3 : Description of the proposed SG emulation strategy: Simplified Virtual Synchronous Compensator. Detailed description of the model equations, electromechanical damping strategies and excitation control;

Chapter 4 : Experimental validation of the proposed S-VSC in normal and abnormal grid conditions;

Chapter 5 : State-space modeling of grid connected converters using the component connection method (CCM). The S-VSC state-space model is derived using CCM and then validated experimentally;

Conclusions : Conclusions of this research and future perspectives.

1.6 Published Works and Achievements

This PhD research activity led to the following scientific publications:

Journal Papers

- **F. Mandrile**, E. Carpaneto and R. Bojoi, "Grid-Feeding Inverter with Simplified Virtual Synchronous Compensator Providing Grid Services and Grid Support," in *IEEE Transactions on Industry Applications*, doi: 10.1109/TIA.2020.3028334.
- **F. Mandrile**, S. Musumeci, E. Carpaneto, R. Bojoi, T. Dragičević, F. Blaabjerg, "State-Space Modeling Techniques of Emerging Grid-Connected Converters," in *Energies* 2020, 13, 4824.

Conference Papers

- **F. Mandrile**, E. Carpaneto, E. Armando and R. Bojoi, "Simple Tuning Method of Virtual Synchronous Generators Reactive Control," *2020 IEEE Energy Conversion Congress and Exposition (ECCE)*, Detroit, MI, USA, 2020. In press.
- **F. Mandrile**, E. Carpaneto and R. Bojoi, "Grid-Tied Inverter with Simplified Virtual Synchronous Compensator for Grid Services and Grid Support," *2019 IEEE Energy Conversion Congress and Exposition (ECCE)*, Baltimore, MD, USA, 2019, pp. 4317-4323, doi: 10.1109/ECCE.2019.8912266.
- **F. Mandrile**, E. Carpaneto and R. Bojoi, "VSG Simplified Damper Winding: Design Guidelines," *IECON 2019 - 45th Annual Conference of the IEEE Industrial Electronics Society*, Lisbon, Portugal, 2019, pp. 3962-3967, doi: 10.1109/IECON.2019.8926981.
- **F. Mandrile**, E. Carpaneto and R. Bojoi, "Virtual Synchronous Generator with Simplified Single-Axis Damper Winding," *2019 IEEE 28th International Symposium on Industrial Electronics (ISIE)*, Vancouver, BC, Canada, 2019, pp. 2123-2128, doi: 10.1109/ISIE.2019.8781233.

Other Topics Related to Power Electronics and Drives

- L. Zeppegno, **F. Mandrile**, E. Armando and R. Bojoi, "Admittance Model Identification of Inverters using Voltage Injection". *IECON 2020 - 46th Annual Conference of the IEEE Industrial Electronics Society*, Singapore, 2020. In press.
- S. Rubino, R. Bojoi, **F. Mandrile** and E. Armando, "Modular Stator Flux and Torque Control of Multi-Three-Phase Induction Motor Drives," in *IEEE Transactions on Industry Applications*, doi: 10.1109/TIA.2020.3022338.

- S. Musumeci, R. Bojoi, E. Armando, S. Borlo, **F. Mandrile**, "Three-Legs Interleaved Boost Power Factor Corrector for High-Power LED Lighting Application," in *Energies* 2020, 13, 1728.

- D. Cittanti, **F. Mandrile** and R. Bojoi, "Optimal Design of Grid-Side LCL Filters for Electric Vehicle Ultra-Fast Battery Chargers," *2020 55th International Universities Power Engineering Conference (UPEC)*, Torino, Italy, 2020, pp. 1-6, doi: 10.1109/UPEC49904.2020.9209771.

- D. Piumatti, S. Borlo, **F. Mandrile**, M. S. Reorda and R. Bojoi, "Assessing the Effectiveness of the Test of Power Devices at the Board Level," *2019 XXXIV Conference on Design of Circuits and Integrated Systems (DCIS)*, Bilbao, Spain, 2019, pp. 1-6, doi: 10.1109/DCIS201949030.2019.8959845.

- M. Gregorio, **F. Mandrile**, R. Bojoi, A. Gillone and C. Damilano, "Fully MCU-Based DCM Control of On-Board Charger," *2019 20th International Symposium on Power Electronics (Ee)*, Novi Sad, Serbia, 2019, pp. 1-6, doi: 10.1109/PEE.2019.8923297.

- S. Musumeci, A. Fratta, E. Armando, **F. Mandrile** and S. Borlo, "Soft Switching Full-Bridge Isolated Circuit Solution for Auxiliary Power Supply in Power Converter Systems," *IECON 2019 - 45th Annual Conference of the IEEE Industrial Electronics Society*, Lisbon, Portugal, 2019, pp. 1985-1990, doi: 10.1109/IECON.2019.8927310.

- M. Gregorio, **F. Mandrile** and S. Musumeci, "Comparative Evaluation and Simulation of Current Control Methods of LLC Converters in EV Battery Chargers," *2019 IEEE 5th International forum on Research and Technology for Society and Industry (RTSI)*, Florence, Italy, 2019, pp. 188-193, doi: 10.1109/RTSI.2019.8895526.

- E. Armando, R. Bojoi, A. Fratta, **F. Mandrile**, S. Musumeci and A. Tenconi, "H-Bridge Converter as Power Electronics Workbench: An Effective Teaching Case of Learning by Doing," *2019 21st European Conference on Power Electronics and Applications (EPE '19 ECCE Europe)*, Genova, Italy, 2019, pp. P.1-P.10, doi: 10.23919/EPE.2019.8915071.

- S. Borlo, D. Cittanti, M. Gregorio, **F. Mandrile** and S. Musumeci, "Comparative CCM-DCM Design Evaluation of Power Inductors in Interleaved PFC Stage for Electric Vehicle Battery Chargers," *2019 International Conference on Clean Electrical Power (ICCEP)*, Otranto, Italy, 2019, pp. 180-186, doi: 10.1109/ICCEP.2019.8890112.

- S. Rubino, R. Bojoi, **F. Mandrile** and E. Armando, "Modular Stator Flux and Torque Control of Multiphase Induction Motor Drives," *2019 IEEE International*

Electric Machines & Drives Conference (IEMDC), San Diego, CA, USA, 2019, pp. 531-538, doi: 10.1109/IEMDC.2019.8785376.

- S. Musumeci, **F. Mandrile**, A. Novello, A. Raciti and G. Susinni, "Very Low Input Voltage Synchronous Coupled Inductor Boost Converter with High Performance Power MOSFETs," *2018 IEEE International Telecommunications Energy Conference (INTELEC)*, Turin, 2018, pp. 1-6, doi: 10.1109/INTLEC.2018.8612365.

Moreover, during my PhD, I was recipient or co-recipient of the following prizes:

- Politecnico di Torino – XXXIII Cycle PhD in Electrical, Electronics and Communications Engineering Prize (2020);
- First prize – MOTUS-E Consortium Call for Papers Award for a work titled "EV Fast-Charging Stations: a Boost for Power System Stability?" (2020);
- First Prize – Vishay Workshop 2019 for a work titled "Fully MCU-Based DCM Control of an On-Board Charger" (2019).

Chapter 2

Overview of VSM Models

Starting from 2007, several VSM models have been proposed in the technical literature [31–70] and are shown as a tree diagram in Fig. 2.1. In this chapter, these VSM solutions are presented and the specific features of each model are highlighted. Useful review papers are also available in the literature, as [71–73].

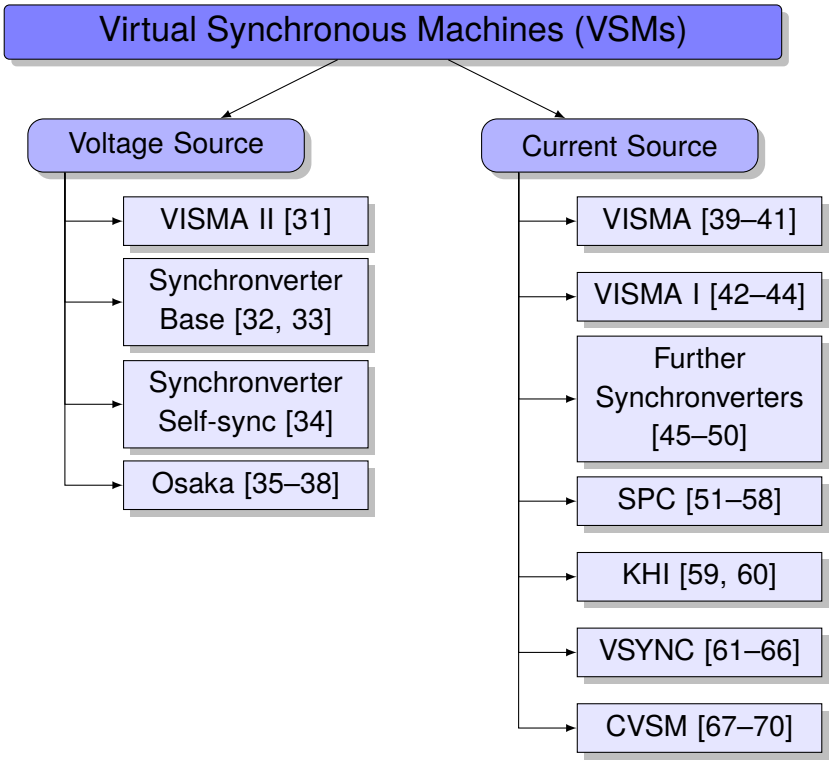

Figure 2.1: Tree diagram of the main VSM solutions available in the technical literature.

Since VSMs are a high level control technique and their behavior does not depend on the topology of the dc/ac converter nor on the grid side low pass filters, in this thesis

(as in most literature), a two-level three-phase inverter, interfaced to the grid through an LCL filter as in Fig. 2.2 will be considered. This converter is considered to be supplied by an ideal dc source, such as a battery storage system.

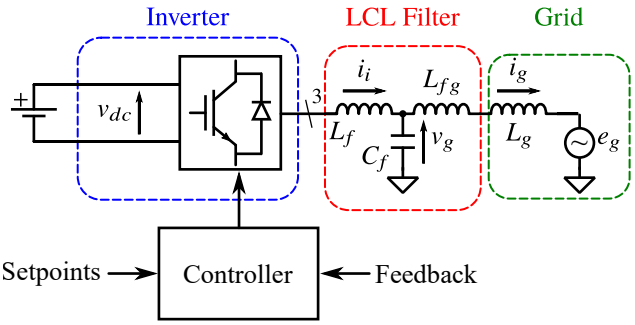

Figure 2.2: Diagram of the considered inverter for VSM implementation.

After having introduced the hardware topology of the converter, it is useful to provide a first major classification of VSM models. They can be divided according to their grid side equivalent behavior in two groups: voltage source or current source VSMs.

The voltage source VSMs behave as a controlled voltage source or as an equivalent Thévenin circuit connected to the grid (see Fig. 2.3). This voltage source is controlled by the controller according to the VSM model, receiving the current feedback from the grid (in this thesis the converter side current i_i will be considered, but also the grid side current i_g can be used).

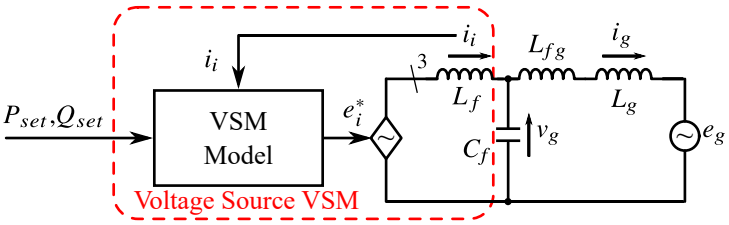

Figure 2.3: Equivalent block diagram of a VSM behaving as a voltage source.

The advantages of this approach can be summarized as follows:

- Easy control strategy: they are controlled in open loop fashion and the voltage reference e_i^* is directly fed to the PWM modulator;
- They are more suited for a connection to a weak grid compared to current controlled converters. In fact they present an inductive behavior for a large frequency range and are, therefore, less prone to harmonic instability as demonstrated in [74, 75].

However, this paradigm presents serious drawbacks that can affect the practical implementation. First, it is difficult to provide an effective current limitation strategy. This is a

crucial aspect for the correct operation of the converter in case of faulty conditions (e.g. voltage dips in the grid) and it must be ensured in order to avoid untimely disconnections of the converter, due to overcurrent faults.

Moreover, some models, as it will be explained in the following sections, use the physical low pass filter inductor (L_f and its equivalent resistance R_f) as the stator impedance of the VSM. This way, the stator is emulated as a Thévenin circuit, where the inverter reference voltage e_i^* is the equivalent back emf of the virtual machine and the inductive filter L_f is the equivalent stator impedance. This leads to two disadvantages:

- The magnitude of the inductive filter L_f values is typical smaller compared to the one of real SGs stators. Therefore, they are not emulated properly. Besides, in case of a large ratio between the resistive and the inductive parts of the filter, there is a coupling between the active and reactive power channels, which must be compensated by an appropriate control strategy;

- The physical filter is determined by hardware design considerations (current ripple reduction) and, therefore, it has constant parameters. It is, however, beneficial to tune the virtual stator parameters and modify them online. Besides, the ratio between the resistive and the inductive part of the filter is fixed and may lead to couplings between the active and reactive power transfer.

This second drawback can be solved by adding a proper control strategy, which emulates a virtual stator, at the price of increased complexity.

The other VSM paradigm is the current source behavior. In this case, the VSM is equivalent to a current source connected to the grid, as shown in Fig. 2.4. In this case, the VSM model measures the grid voltage v_g and generates proper current references i_i^* for the inner current controller.

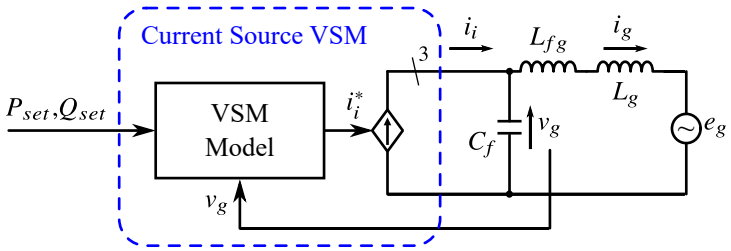

Figure 2.4: Equivalent block diagram of a VSM behaving as a current source.

Compared to the voltage source approach, the current source model completely solves the current limitation issue, being able to control the actual current within the specified limits. Moreover, the stator emulation does not depend on the actual converter filter parameters, as the converter behaves as an ideal current source. This way, the machine stator can be emulated with no limitation dictated by the physical parameters of the converter. Moreover, the ratio between the resistive and inductive part of the virtual stator

can be tuned in order to avoid the coupling between the active and reactive channels. The drawbacks of this solutions are the reduced robustness when connected to weak grids [74, 75] and the greater complexity due to the closed loop current controller.

In the following sections, each solution presented in Fig. 2.1 will be presented and analyzed. Finally, an overall comparison of the state of the art will summarize this chapter.

2.1 VISMA

The family of the VIrtual Synchronous MAchine (VISMA) models represents the first attempt of SG emulation using static converters. The first works were published by the Clausthal University of Technology in 2007 [39, 40]. Then, this model evolved into two other variants (i.e., VISMA I and VISMA II). In total, the VISMA models are:

- VISMA Base[40, 41];
- VISMA I [42–44];
- VISMA II [31].

In the following sections, each of them will be described in detail.

2.1.1 VISMA

In this first release of the VISMA model, the SG was fully modeled according to the classical power system representation of SGs [2]. This is a voltage-input current-output model. The VISMA model generates the current references i^* for the current controller. The adopted model is a 7-th order SG implementing: a virtual rotor, damper windings on both the d- and q-axis (modeled as the D and Q windings), stator windings (d and q windings) and a full excitation winding (e), as shown in Fig. 2.5.

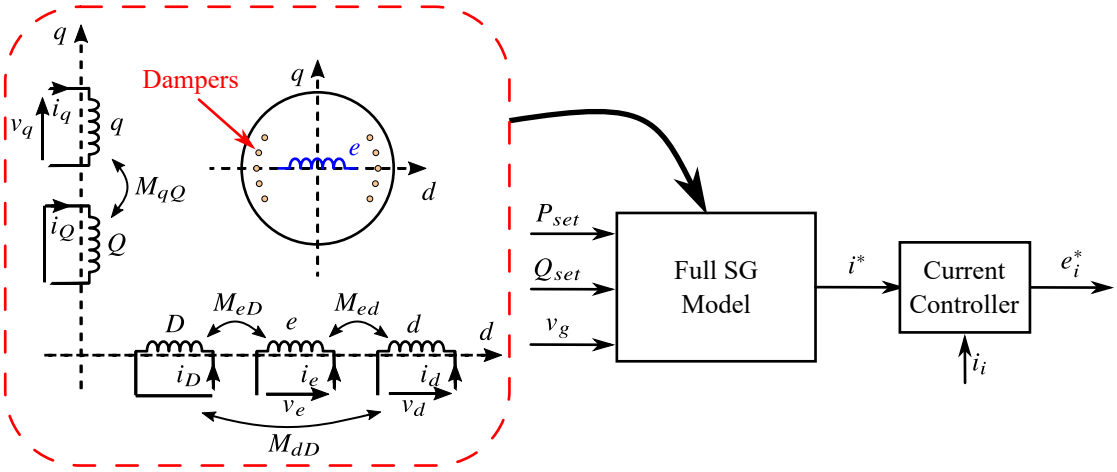

Figure 2.5: Equivalent block diagram of the VISMA model [40, 41].

The VISMA SG equations [41] divided as follows:

- Mechanical part:

$$\begin{aligned} \omega_r &= \int (T_m - T_e)\, dt \\ \theta_r &= \int \omega_r dt \\ T_e &= \frac{3}{2}\left(\lambda_d i_q - \lambda_q i_d\right) \end{aligned} \tag{2.1}$$

  where T_m and T_e are the virtual mechanical and electromagnetic torque; ω_r is the virtual rotor speed and θ_r its virtual position;

- Virtual dampers:

$$d\text{-axis} \begin{cases} \lambda_D = -\int R_D i_D dt \\ i_D = \dfrac{\lambda_D - M_{dD} i_d - M_{eD} i_e}{L_D} \end{cases} \tag{2.2}$$

$$q\text{-axis} \begin{cases} \lambda_Q = -\int R_Q i_Q dt \\ i_Q = \dfrac{\lambda_Q - M_{qQ} i_q}{L_Q} \end{cases} \tag{2.3}$$

  where D and Q stand for the damper on the d-axis and q-axis, respectively. The damper variables are λ and i (flux linkage and current), while the parameters of the dampers are R (resistance), L (self inductance) and the mutual inductances with the other windings of the same axis (M_{dD}, M_{qQ} and M_{eD});

- Stator:

$$d\text{-axis}\begin{cases} \lambda_d &= -\int \left(v_d - R_d i_d + \omega_r \lambda_q\right) dt \\ i_d &= \dfrac{\lambda_d - M_{dD} i_D - M_{ed} i_e}{L_d} \end{cases} \tag{2.4}$$

$$q\text{-axis}\begin{cases} \lambda_q &= -\int \left(v_q - R_q i_q - \omega_r \lambda_d\right) dt \\ i_q &= \dfrac{\lambda_q - M_{qQ} i_Q}{L_q} \end{cases} \tag{2.5}$$

  where the nomenclature is similar to the dampers. The variable λ indicates the flux linkages, i the currents, R the resistances, L the self inductances and M the mutual inductances. v is the grid voltage vector, transformed into the (d,q) frame synchronous with the virtual rotor;

- Excitation winding:

$$\begin{aligned} \lambda_e &= -\int (v_e - R_e i_e)\, dt \\ i_q &= \frac{\lambda_e - M_{eD} i_D - M_{ed} i_d}{L_e} \end{aligned} \tag{2.6}$$

where v_e is the excitation voltage, i_e the excitation current, λ_e the excitation flux linkage. The excitation parameters are the resistance R_e, the self inductance of the excitation winding L_e and the mutual couplings on the d-axis M_{eD} and M_{ed}.

This model features the following benefits:

- Physical-based model: the emulation of a traditional SG is complete and the same power system theory can be applied;
- No need for a Phase Locked Loop (PLL);
- Current limitation during faults thanks to the current controller;
- Same ancillary services performance as SGs.

However, this early model is very complex and requires a large computational effort. Moreover, being a full implementation of a SG, it also inherits the classical drawbacks of SGs, such as electromechanical oscillations and poor damping. Moreover, the complete emulation of the excitation winding sets a strong limitation on the dynamic behavior of the reactive power.

2.1.2 VISMA I

A first improvement of the VISMA is represented by the VISMA I [42–44]. Similarly to the VISMA, it is a voltage-input current-output model and it is divided into two parts, as it can be seen in Fig. 2.6.

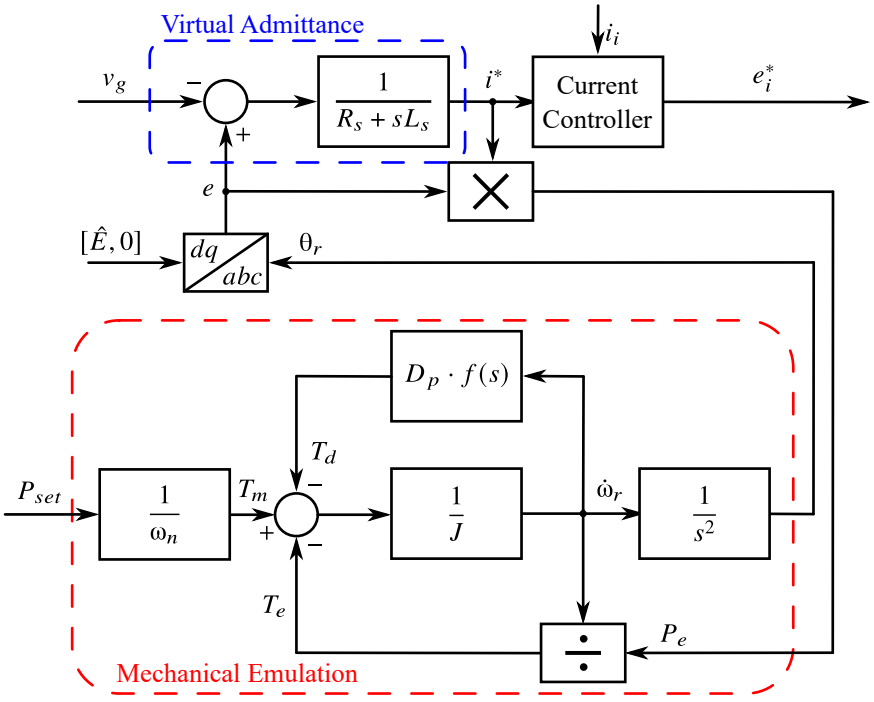

Figure 2.6: Equivalent block diagram of the VISMA I model [42–44].

The first part is the mechanical emulation, implementing a slightly modified version of the swing equation:

$$T_m - T_e = J\dot{\omega}_r + D_p \cdot f(s)\dot{\omega}_r \tag{2.7}$$

Compared to the classical swing equation, the damping term is here provided by the transfer function $D_p \cdot f(s)$ and it is proportional to the derivative of the rotor speed $\dot{\omega}_r$. Only limited information is available on the structure of $f(s)$, but from [42], $f(s)$ is implemented as a low pass filter with a long time constant (i.e., 1 s).

The second part is a virtual admittance (resistance R_s and inductance L_s), which calculates the current references i^* from the grid voltage v_g and the machine virtual back emf e. The amplitude of the back emf is generated externally and it equal to $\hat{E}$.

In summary, the VISMA I is a simplified version of the VISMA and does not emulate non necessary aspects, such as the excitation winding or both damper windings. It still preserves the current limitation capabilities and does not need a PLL. However, many aspects were left unclear and the damping strategy is not well explained, therefore, it is difficult to judge its actual performance.

2.1.3 VISMA II

The second variation of the VISMA is the VISMA II [31]. This represents a novelty for the VISMA family, as it is a current-input voltage-output model. The VISMA II is composed of two parts, as shown in Fig. 2.7.

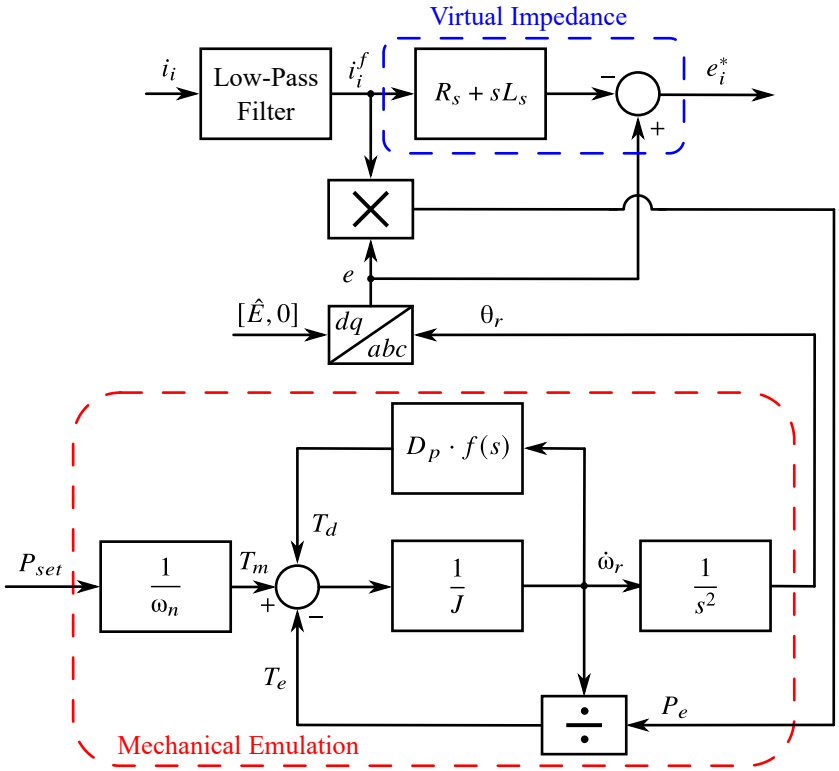

Figure 2.7: Equivalent block diagram of the VISMA II model [31].

The mechanical part is identical to the one of the VISMA I, guaranteeing a similar behavior.

The difference from the VISMA I is the presence of a virtual impedance instead of the virtual admittance. The open loop reference voltage for the PWM modulator is, therefore, calculated as:

$$e_i^* = e - (R_s + sL_s)\, i_i^f \tag{2.8}$$

where e is again the back emf of the VISMA, R_s and L_s the virtual impedance resistive and reactive part, and i_i^f is the filtered converter current. The converter current must in fact be filtered before feeding it to the virtual impedance, as the involved derivative would amplify the high frequency components of the measured current. The proposed filtering is a low pass filter, but no specific information about its tuning is given.

In conclusion, this is a simpler model compared to VISMA and VISMA I, since no closed loop control is involved, and inherits all the benefits of a voltage-source VSM.

However, there is no current limitation algorithm available and the virtual impedance practical implementation is unclear in its numerical aspects (filtering of the measured converter current).

2.1.4 Summary and Conclusions on VISMA Models

The three VISMA models available in the literature represent a landmark for VSMs as their are the first examples of this technology. However, there are several limitations, which do not make these models feasible for actual implementation.

In particular:

- The base VISMA model is too complex and inherits all the disadvantages of real SGs (oscillations...);
- The modified VISMA I is an improvement of the base VISMA, but it is unclear how the electromechanical damping is implemented;
- The VISMA II is a good attempt towards a voltage-source model, however it suffers from implementation drawbacks related to the derivative of the virtual impedance and the current limitation strategy.

2.2 Synchronverter

The Synchronverter model was first proposed in 2009 [33, 76], followed by a more complete journal paper in 2011 [32]. Several modifications and improvements were proposed in the following years and they will be described in the following sections. A useful review, which keeps track of the modifications and of the improvements to this model can be found in [45].

2.2.1 Base Synchronverter Model

Initially, it is useful to describe the original Synchronverter model [32] and its basic features. The block diagram of this solution is depicted in Fig. 2.8.

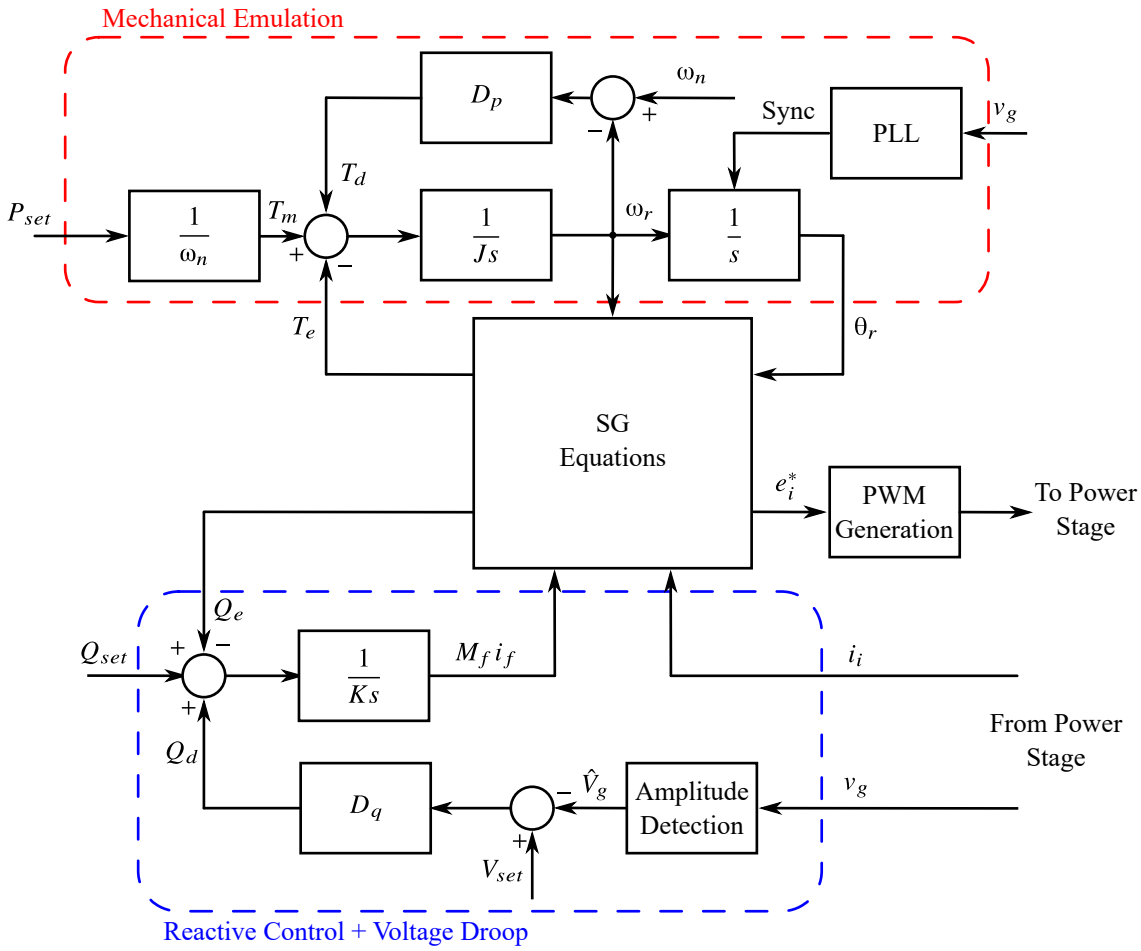

Figure 2.8: Block diagram of the base version of the Synchronverter [32].

This is a current-input voltage-output model, as it receives the converter current i_i as a feedback and directly generates the moving average voltage reference e_i^* for the PWM modulator, without using closed loop controllers.

This model consists of three parts, as shown in Fig. 2.8:

- Mechanical emulation part;
- Reactive control and voltage droop control;
- SG equations emulation.

Mechanical Emulation

The mechanical emulation is performed by implementing the swing equation of SGs as follows:

$$T_m - T_e = J\frac{d\omega_r}{dt} + D_p\left(\omega_r - \omega_n\right) \tag{2.9}$$

where T_m is the equivalent mechanical torque, T_e is the electromagnetic torque of the Synchronverter, J is the inertia of the virtual rotor, ω_r is its virtual speed, D_p the damping-droop coefficient and ω_n the rated grid frequency. In this model the torque is obtained from the power references by assuming an almost constant rotating speed equal to the nominal grid frequency. Therefore $T_m = P_{set}/\omega_n$.

It can be noticed that a droop-based damping is implemented, using the coefficient D_p. This means that the base version of the Synchronverter couples the damping action and the active droop action, as it will be explained in detail in section 3.3.1. For now, it can be said that the necessary values of D_p to provide sufficient damping to the Synchronverter are much larger (around ten times) than the droop coefficients required by the technical standards (2–5%), as seen in 1.1. This leads to a large active power injection into the grid when it is operating at non nominal frequency.

The second key aspect of the Synchronverter is the grid synchronization algorithm. The synchronization process is performed by using a PLL, which is in charge of measuring the grid speed and angle to initialize (Sync signal) the mechanical part of the model, ensuring a seamless synchronization.

The tuning procedure for the virtual parameters is available in [32].

Reactive Part

The second part of this model, marked in blue in Fig. 2.8, is the reactive power control and the voltage droop control.

This consists in an integral controller (with gain $1/K$) which tracks the sum of the external reactive power references Q_{set} (e.g., coming from the grid operator) and the reactive power reference coming from the voltage droop control Q_d. The output of this controller is the equivalent excitation flux linkage $M_f i_f$.

This can be explained by the following equation:

$$M_f i_f = \int \frac{Q_{set} + Q_d - Q}{K} dt \tag{2.10}$$

The voltage droop is of proportional type, with gain D_q.

$$Q_d = D_q \left(V_{set} - \hat{V}_g \right) \tag{2.11}$$

where V_{set} is the reference voltage and $\hat{V}_g$ is the measured grid voltage amplitude from the instantaneous grid voltage v_g.

SG Equations

Finally, the implementation of the SG electrical equations links the mechanical and the reactive part to the model output. The following equations are, therefore, implemented:

$$\begin{aligned} T_e &= M_f i_f \cdot \left\langle \bar{i}_i, \widetilde{\sin}(\theta_r) \right\rangle \\ \bar{e}_i^* &= \omega_r M_f i_f \widetilde{\sin}(\theta_r) \\ Q_e &= -\omega_r M_f i_f \left\langle \bar{i}_i, \widetilde{\cos}(\theta_r) \right\rangle \end{aligned} \tag{2.12}$$

where $\bar{e}_i^*$ is the reference voltage to be fed to the PWM modulator; $\widetilde{\sin}(\theta_r)$ and $\widetilde{\cos}(\theta_r)$ are two angle vectors as follows:

$$\widetilde{\sin}(\theta_r) = \begin{bmatrix} \sin(\theta_r) \\ \sin\left(\theta_r - \frac{2\pi}{3}\right) \\ \sin\left(\theta_r + \frac{2\pi}{3}\right) \end{bmatrix}; \quad \widetilde{\cos}(\theta_r) = \begin{bmatrix} \cos(\theta_r) \\ \cos\left(\theta_r - \frac{2\pi}{3}\right) \\ \cos\left(\theta_r + \frac{2\pi}{3}\right) \end{bmatrix} \tag{2.13}$$

and the notation $\langle \cdot, \cdot \rangle$ indicates the inner product of the quantities within the brackets.

It must be noted that the electrical quantities (voltages and currents) are expressed in the three-phase stationary frame. From these equations, the Synchronverter operates as a Thévenin equivalent, with a voltage source e_i^* behind the LCL physical filter reactance L_f. This represents an issue, as the typical values for L_f are smaller than the typical values of impedance of a SG [46]. Moreover, this value is fixed and cannot be tuned during the operation.

The voltage-source behavior also leads to the coupling of the active and reactive power flows when connected to grids where the resistive part is not negligible. This means that a decoupling controller is necessary.

Summary

The features of this model can be summarized as:

- Easy implementation, directly from the SG equations;
- A PLL is needed for the initial grid synchronization;
- The electromechanical damping is performed leveraging a droop action. The necessary damping coefficient is much larger than usual active droop coefficient, leading to an excessive active power injection when the grid frequency is non nominal;

- No current limitation under faulty conditions. There is no closed loop current control;
- The VSM virtual stator impedance is the physical impedance L_f of the LCL filter interfacing the converter to the grid. This is a smaller value than the usual for SGs and cannot be tuned online.

2.2.2 Self-Synchronizing

The need for a PLL of the base Synchronverter was solved in [34], where a self-synchronized version was proposed. The relative block diagram is depicted in Fig. 2.9.

The proposed self-synchronization process is as follows:

1. The Synchronverter is off. The switch S_P is closed and the voltage droop control is off (S_Q is open). The selector S_C is in position 1: the feedback current $i = i_v$. The power references are null;
2. The model is activated. The PWM modulation is disabled and the VSM model is executed, using as feedback the fictitious current i_S calculated using the virtual impedance as follows:
$$i_v = \frac{e_i^* - v_g}{R + sL}; \tag{2.14}$$
3. The equivalent back emf e_i^* of the Synchronverter matches the grid voltage v_g and the virtual current i_v reaches zero. At this point, the Synchronverter is ready to be connected to the grid and the modulation can be enabled;
4. As soon as the modulation is enabled, the current feedback uses the measured converter current i_i instead of the virtual current i_v. The model can now be fed with the required power setpoints.

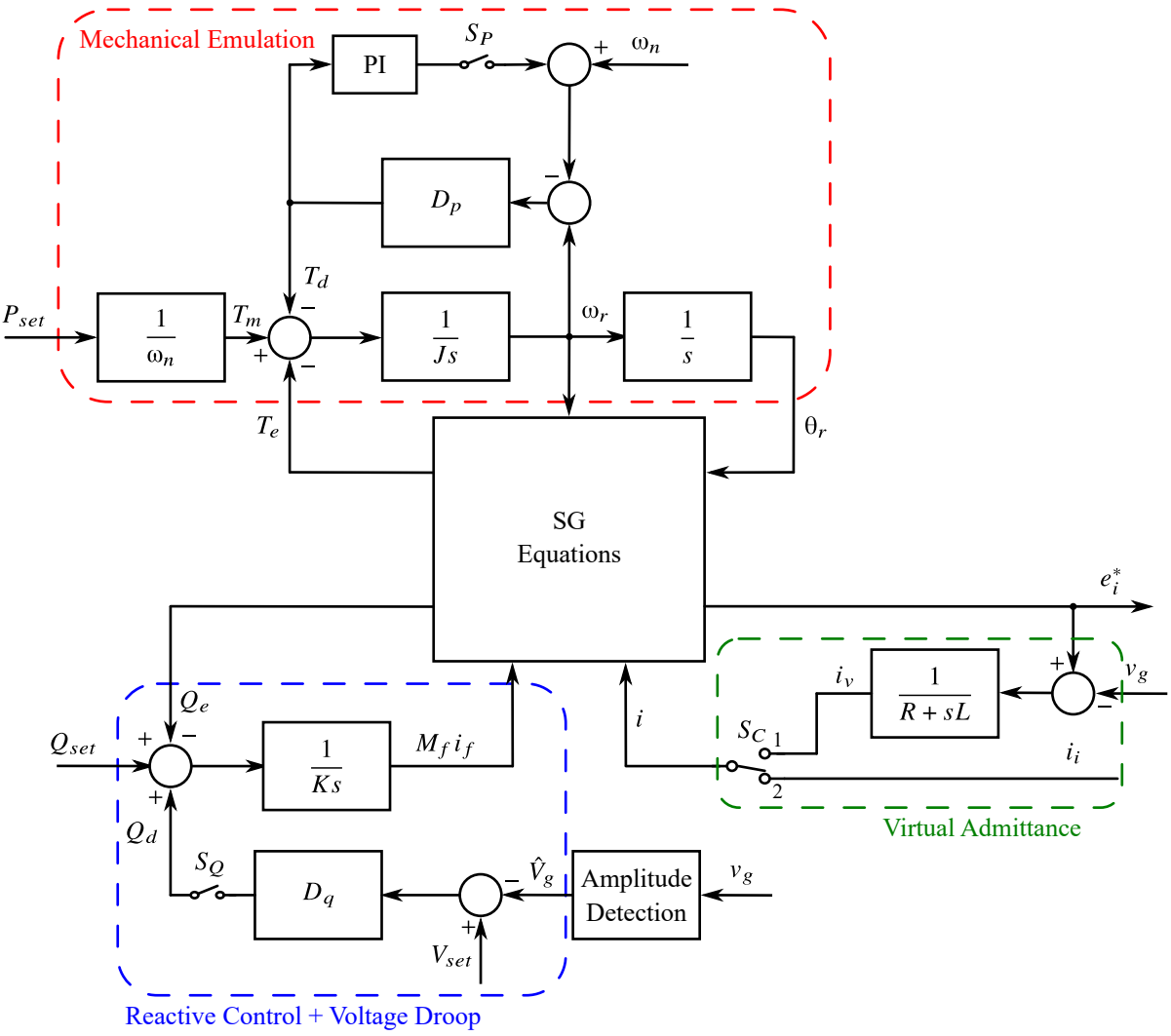

Figure 2.9: Block diagram of the self-synchronized version of the Synchronverter [34].

The switches S_P and S_Q are opened and closed to activate/deactivate the active and reactive droop controllers.

The self-synchronized Synchronverter has the following features:

- The PLL is not necessary anymore, solving a drawback of the base implementation;
- The virtual admittance can be tuned in order to obtain the desired virtual synchronization transient. However, it is not used in ordinary operation;
- The operating stator impedance is still the physical filter one, as in the base version;
- The current is still not limited in case of faults, as in the base model;
- If S_P is open, then there is still an excessive active droop effect, as before.

2.2.3 Further Modifications and Improvements

More improvements were added to the Synchronverter during the years, in order to solve the remaining drawbacks.

Current Limitation

The lack of current limitation during faults has been solved with two different approaches:

- An hysteresis controller is enabled when an overcurrent is detected and switches the model from voltage source to current source operation [48];
- The Synchronverter is fully switched to a current-source model [49, 50].

In both cases, a virtual impedance is employed to generate the current references for the internal controller. In [49], additional protection features were added to prevent the model to reach the current limitation and instabilities during fault (i.e., load angle limitation and virtual excitation flux limitation).

Virtual Stator Impedance Active-Reactive Power Coupling

Several solutions have been proposed [77–79] to decouple the Synchronverter from the physical filter impedance and the resistive/reactive ratio of the grid at the point of connection. In particular:

- Virtual increase of the filter parameters [77], by altering the reference signal to the modulator as in Fig. 2.10. The reference voltage is corrected so that the voltage g is:
$$g = \frac{(n-1)v_g + e_i^*}{n} \tag{2.15}$$
this results to an equivalent impedance n times larger than the filter impedance. However, this method maintains the ratio between the resistive and the reactive part of the impedance;

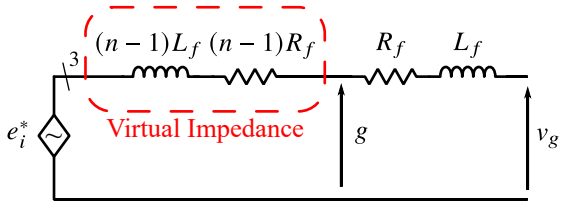

Figure 2.10: Synchronverter with virtual impedance as in [77].

- Addition of virtual capacitors in series to the virtual stator to prevent dc voltage component in the grid voltage to interact with the VSM [77];

- Decoupling strategies [78, 79] to limit the influence of non purely inductive networks.

Damping-Droop Coupling

The limitation of the damping-droop coupling has been solved in the following ways:

- Partial saturation of the active droop power and selection of the damping power using filters [46, 47], as depicted in Fig. 2.11. This strategy separates the damping torque (high frequency) from the low frequency droop action and torque references, which are saturated in the range $[T_{min}, T_{max}]$ to comply with the inverter rating;

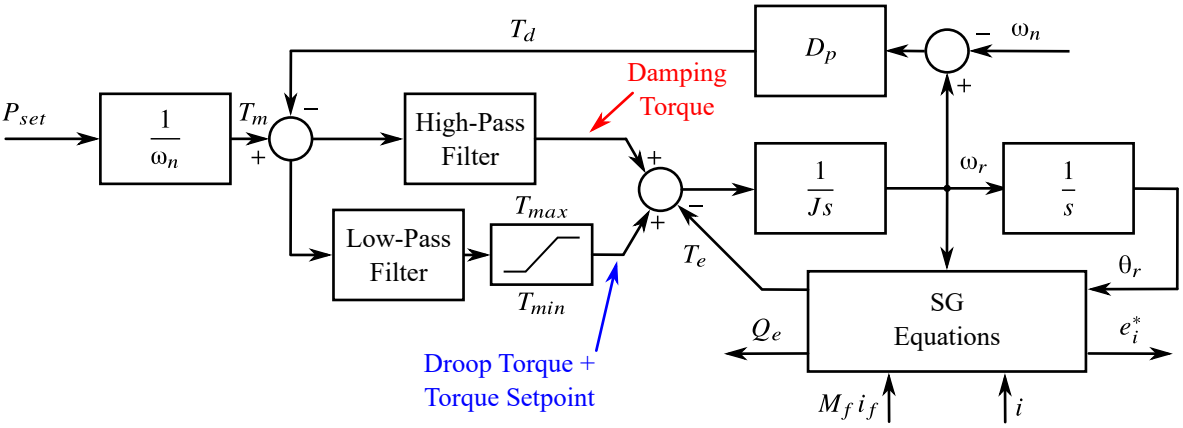

Figure 2.11: Synchronverter with damping and droop decoupling as in [46, 47]. The rest of the model is as in the base version of Fig. 2.8.

- A damping correction loop, based on the derivative of the ratio between the active power flow and the virtual flux of the Synchronverter. This solution requires low pass filters due to the derivative involved [80].

Summary on Synchronverter

The Synchronverter model gained great popularity due to the easy implementation of its initial formulation. However, as it has been demonstrated in the literature [78, 79], the base version has some drawbacks, such as the dependence from the physical filter inductance of the converter. These issues have been solved during the years. However, this increased the complexity very much. Moreover, the current limitation in case of faults is a serious drawback, which can only be solved by shifting to a current controlled model, again introducing additional complexity and the shift to a current source VSM.

2.3 Synchronous Power Controller (SPC)

The Synchronous Power Controller (SPC) was first patented in 2011 [51–53]. This is a voltage-input current-output model and its general structure is depicted in Fig. 2.12.

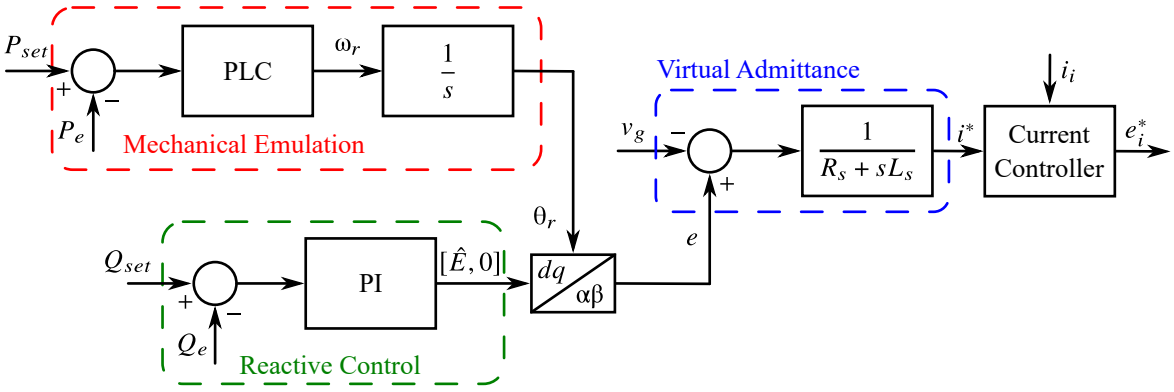

Figure 2.12: General block diagram of the SPC.

This model is organized in the following key blocks:

- Power Loop Control (PLC): this is the cornerstone of the electromechanical emulation and damping. Several variants have been proposed and they will be analyzed in the following sections;
- Reactive control. The SPC employs a PI controller for the reactive power management. This generates the peak voltage of the SPC back emf $\hat{E}$;
- Virtual admittance: The virtual admittance generates the current references for the current controller.

The power feedbacks P_e and Q_e are calculated from the converter current i_i and the grid voltage v_g as follows:

$$P_e + jQ_e = 3/2 \left(v_{g\alpha} + jv_{g\beta}\right) \left(i_{i\alpha} - ji_{i\beta}\right) \tag{2.16}$$

It is useful to define the maximum transferable active power $P_{max} = EV/X_{tot}$, as this parameter is used for the tuning of the various PLC variants. This is the maximum transferrable power across an inductive line of reactance X_{tot}, supplied by the voltages E and V. In the specific case, V is the nominal grid voltage and it is equal to the SPC voltage E. The total reactance is the sum of the virtual one and the grid one $X_{tot} = X_s + X_g$.

2.3.1 PLC Base Version

The first version of the PLC implements the swing equation of SGs [54, 57, 58]. This can be expressed as follows:

$$PLC(s) = \frac{1}{\omega_n \left(Js + D_p\right)} \tag{2.17}$$

The parameters of the PLC can be calculated as follows:

$$\begin{aligned} J &= \frac{2HS_b}{\omega_n^2} \\ D_p &= \frac{2\zeta}{\omega_n}\sqrt{\frac{2HS_bP_{max}}{\omega_n}} \end{aligned} \tag{2.18}$$

This implementation of the PLC is simple and similar to the theory of SGs, however, it has a serious drawback. In fact, it shows a strong coupling between the damping of the SPC (coefficient D_p) and the active droop effect. Typically, the necessary values for D_p to guarantee satisfactory damping are around ten times larger than the normal droop coefficients prescribed by the grid standards. Therefore, this solution would inject a too large active power when the grid frequency is off nominal values.

2.3.2 PLC PI Version

The second version of the SPC uses a PI controller as PLC [56, 58].

$$PLC(s) = \frac{k_X s + k_H}{s} \tag{2.19}$$

The gains k_X and k_H of this regulator are calculated as follows:

$$\begin{aligned} k_X &= \zeta\sqrt{\frac{2\omega_n}{HS_bP_{max}}} \\ k_H &= \frac{\omega_n}{2HS_b} \end{aligned} \tag{2.20}$$

Differently from the previous solution, this PLC does not mix the damping and the droop action. This enables a separate integration of an active droop controller, tuned according to the grid requirements. However, also this solution is not free from drawbacks. In fact, due to the proportional term of the PI regulator, the virtual speed ω_r suffers from large disturbances, related to the active power feedback (i.e., harmonics, measurement noise...) and, therefore, provides lower quality information about the actual grid frequency.

2.3.3 PLC Lead-Lag (LL) Version

The last version of the PLC is based on a lead-lag regulator [55, 56, 58] expressed as:

$$PLC(s) = \frac{k_p s + k_i}{s + k_g} \tag{2.21}$$

The gains k_p, k_i and k_g of this regulator are calculated as follows:

$$\begin{aligned} k_p &= \zeta\sqrt{\frac{2\omega_n}{HS_bP_{max}}} - \frac{1}{2HP_{max}R_D} \\ k_i &= \frac{\omega_n}{2HS_b} \\ k_g &= \frac{1}{2HR_D} \end{aligned} \tag{2.22}$$

This solution embeds a tunable active droop controller. In fact, the parameters depend on the droop coefficient R_D and are adjusted accordingly. Like the PI solution, also this one features a direct feed-through of any disturbances in the active power measurement, which propagate to the virtual speed ω_r without filtering.

2.3.4 Conclusions and Summary on SPC

The SPC is the most promising VSM model in the literature due to the following advantages:

- Current controlled with easy current limitation;
- No PLL is needed;
- The synchronization is based on power, making it more robust under weak grids;
- Tunable virtual admittance;
- Decoupling between damping and droop action for some implementations (PI and LL).

However, the base version of the PLC must be excluded for the embedded and not tunable active droop action and further improvements are necessary to provide more high frequency rejection to the virtual rotor speed.

2.4 Osaka Model

The Osaka model is a voltage-source VSM, proposed by authors from the University of Osaka [35, 81] for the first time in 2011.

The block diagram of this model is shown in Fig. 2.13. This model has a few key aspects. The first one regards the mechanical emulation and it implements the swing equation of SGs, but the grid frequency for damping is measured by a PLL. This damping method will be described more in detail in 3.3.2. This guarantees a damping action, that is fully decoupled from the active droop control.

A second aspect is that the active droop control is embedded as a virtual governor (see Fig. 2.14), which generates the reference power P^* as the sum of the external setpoint P_{set} and the active droop power. The droop control parameters are the gains k_{droop}, R_D and a low pass filter time constant τ_d.

To overcome the major limitation of voltage source VSMs (current limitation), two overcurrent mechanism are implemented to avoid overcurrent protection during voltage dips. The first one is a virtual resistance R_{lim}, limiting the reference voltage as follows:

$$e_i^* = e - R_{lim} i_i \tag{2.23}$$

The second method is the scaling of the active power reference, according to the rms value of the measured grid voltage $V_{g,rms}^2$. This allows a power limitation while keeping constant the relative angle between the grid and the VSM.

Finally, a PI reactive power regulator was added in [36] to generate the peak value of the virtual back emf voltage $\hat{E}$ of the model and this is able to track the reactive power references and perform a proportional voltage control.

The features of this model can be summarized as:

- Voltage source model with current limitation features;
- Active and reactive droop controllers are embedded;
- No virtual stator is implemented and it relies on the physical filter parameters;
- Damping performed using a PLL, therefore increasing the complexity of this model.

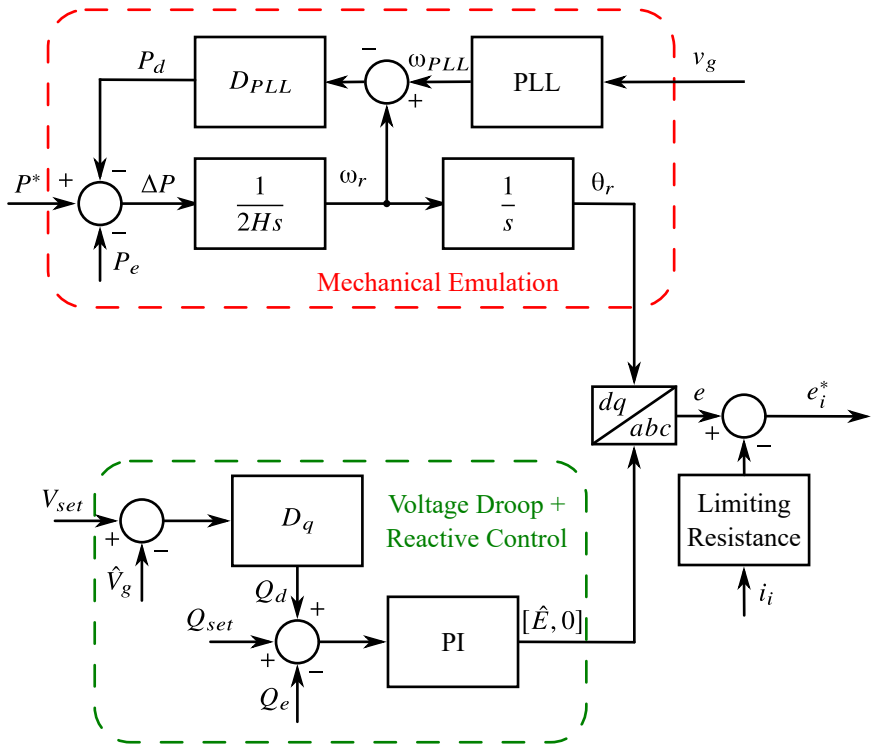

Figure 2.13: Block diagram of the Osaka model.

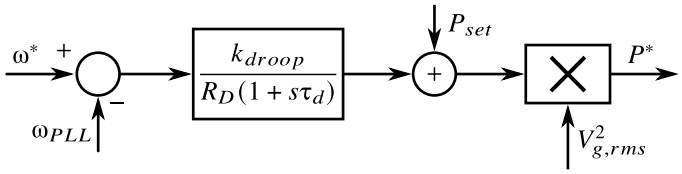

Figure 2.14: Active droop control of the Osaka model.

2.5 Kawasaki Heavy Industries (KHI) Model

The Kawasaki Heavy Industries (KHI) Model was first presented in [59]. The KHI is a voltage input current output model, as shown in Fig. 2.15.

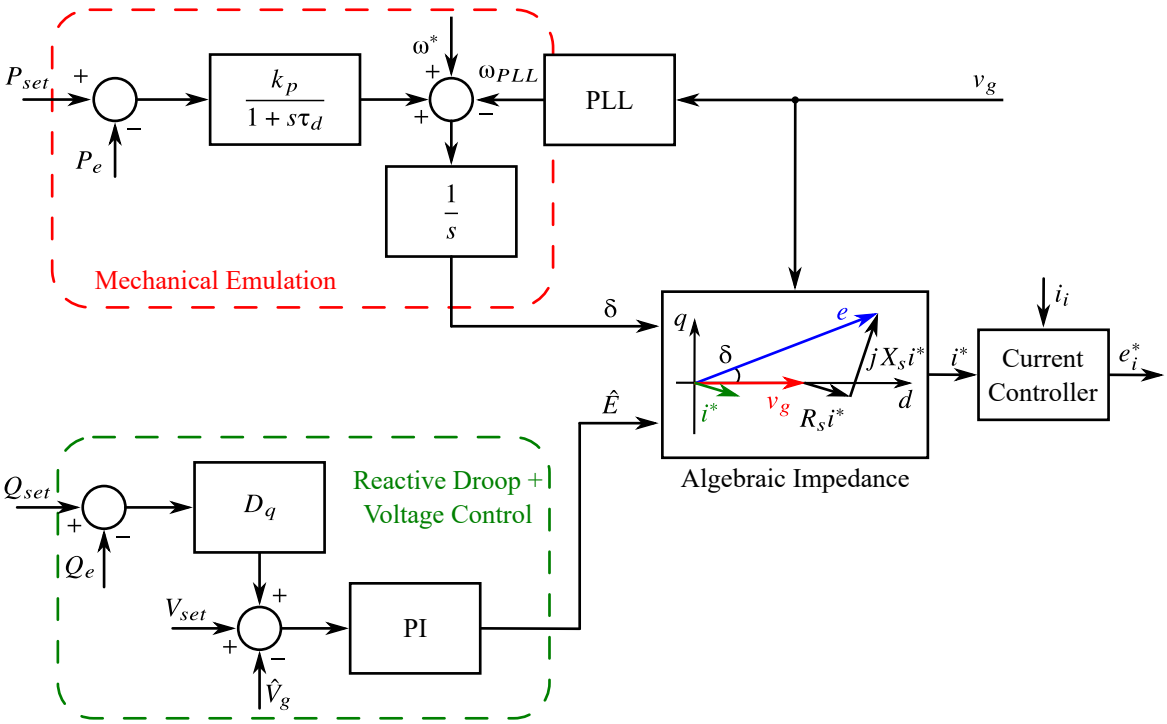

Figure 2.15: Block diagram of the Kawasaki Heavy Industries (KHI) model [59, 60].

The mechanical emulation implements a virtual governor with inertial action, performed using a low pass filter tuned with a proportional gain k_p and the filter time constant τ_d. The damping is provided by a PLL. The output of the mechanical part is the load angle δ of the virtual machine.

Then, a voltage amplitude control at the point of common coupling is implemented with a PI regulator. This regulator does not only track the reference voltage V_{set}, but also takes into account the reactive power exchange requirements coming from a reactive droop control. This second part of the model generates the virtual machine back emf amplitude $\hat{E}$. Moreover, the reactive part of this model implements an integral regulation of the voltage and a proportional regulation of the reactive power. This might be an issue when it is necessary to comply to the specific reactive capability curves and reactive power injection laws prescribed by the grid standards (see section 1.1.2).

The feedback of these two parts are the active and reactive power exchanged with the grid, calculated from the converter current i_i and the grid voltage v_g as follows:

$$P_e + jQ_e = 3/2\left(v_{gd} + jv_{gq}\right)\left(i_{id} - ji_{iq}\right) \tag{2.24}$$

Finally, the current reference i^* is calculated from a virtual algebraic stator impedance, implementing the fundamental frequency phasorial behavior of the SG stator. The inputs of this algebraic impedance are the amplitude $\hat{E}$ and load angle δ of the virtual back emf e of the model. Then, the following calculation is performed in the virtual rotor (d,q

frame:

$$\begin{bmatrix} i_d^* \\ i_q^* \end{bmatrix} = Y \begin{bmatrix} e_d - v_{gd} \\ e_q - v_{gq} \end{bmatrix} \tag{2.25}$$

where Y is the algebraic stator:

$$Y = \frac{1}{R_s^2 + X_s^2} \begin{bmatrix} R_s & X_s \\ -X_s & R_s \end{bmatrix} \tag{2.26}$$

This specific implementation is simple and requires low computational effort, however, it shows an incorrect behavior when the KHI is supplied with a distorted or unbalanced voltage. In this case, the impedance shown by the KHI is constant at each and every frequency and sequence, differently from the real SGs, which have an inductive behavior. This aspect will be tested and discussed more specifically in section 4.5.

The summary of the KHI model are:

- Current source model, with easy current limitation during faults;
- Algebraic stator, not suitable when supplied with voltage harmonics;
- Needs a PLL for damping.

2.6 VSYNC

The VSYNC model was first proposed in 2009 in the framework of the VSYNC European Project [61, 62]. Several papers, also including field validation were published in the following years [63–66].

The idea behind this model is to modify the conventional PLL structure in order to emulate the SG mechanical behavior.

From the general block diagram of Fig. 2.16, the following features can be reported:

- This is a voltage-input current-output model;
- The grid synchronization is performed using a PLL;
- There is no reactive power loop implemented.

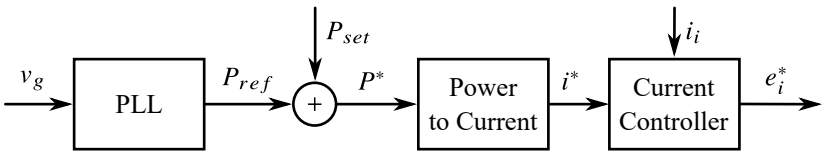

Figure 2.16: Equivalent block diagram of the VSYNC model [62].

The current references i^* are generated in the rotating (d,q) frame synchronous with the modified PLL angle and they are calculated from the active power reference P^* as follows:

$$\begin{aligned} i_d^* &= \frac{2}{3}\frac{v_{gd}}{v_{gd}^2 + v_{gq}^2}P^* \\ i_q^* &= \frac{2}{3}\frac{v_{gq}}{v_{gd}^2 + v_{gq}^2}P^* \end{aligned} \tag{2.27}$$

where the power reference P^* is the sum of the external power references P_{set} and the PLL power references P_{ref} (i.e., $P^* = P_{set} + P_{ref}$).

The structure of the modified PLL is depicted in Fig. 2.17. The power reference P_{ref} is calculated to emulate a SG. To accomplish that, the PLL gains K_d and K_i are computed as follows [62]:

$$\begin{aligned} K_d &= \frac{E}{X_{tot}} \\ K_i &= \frac{\omega_n}{2HS_b} \end{aligned} \tag{2.28}$$

where E is the nominal voltage of the converter (i.e., 1 pu), X_{tot} is the total reactance between the converter and the grid, ω_n is the nominal grid speed, H the inertia constant of the VSYNC and S_b the base power of the converter.

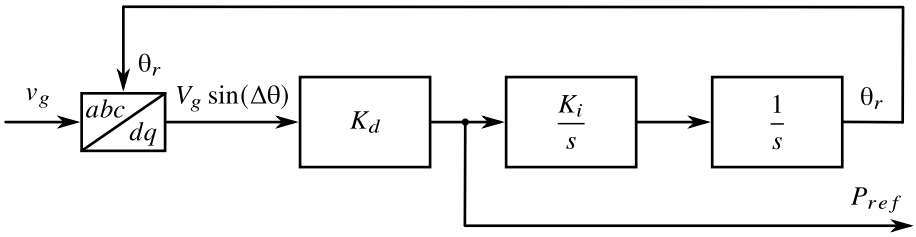

Figure 2.17: Block diagram of the modified PLL employed by the VSYNC model [62].

The positive features of this model can be summarized as:

- Current controlled: the current can be limited easily in case of faults;
- Easy implementation, as it is based on a modified PLL.

However, this model has many drawbacks and limitations:

- The electromechanical behavior is influenced by the non linearities of the PLL;
- There is no stator emulation;
- There is no indication about the reactive power management and in general the grid support features.

For these reasons, this model does not look promising for a complete SG emulation.

2.7 CVSM

The Cascaded Virtual Synchronous Machine (CVSM) was first proposed in 2013 [67] and later refined in [68–70]. This model can be considered as a hybrid between a voltage source and a current source. In fact, as it can be seen in Fig. 2.18, it features a cascaded voltage and current control. This way, this model can efficiently limit the current in case of faults, without incurring into any overcurrent protection.

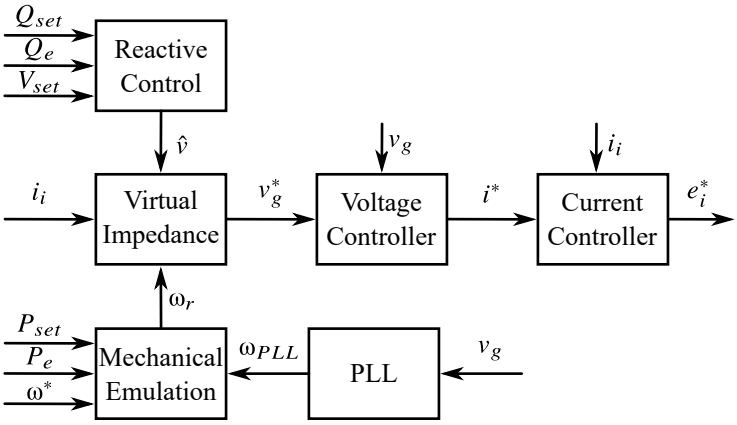

Figure 2.18: Block diagram of the CVSM.

The mechanical emulation part, shown in Fig. 2.19, implements the classical swing equation and uses the speed measured by a PLL to provide damping. Therefore, the damping action and the active droop control are fully decoupled. However, the PLL is an additional component, increasing the complexity of the model. This model also includes an active droop control with coefficient k_{droop}.

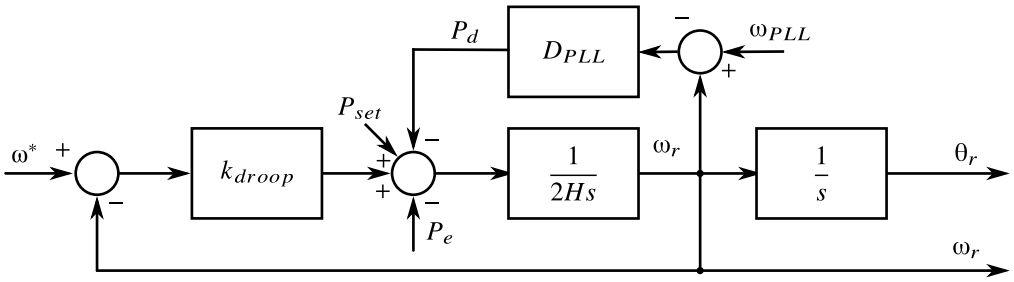

Figure 2.19: Mechanical part of the CVSM.

The reactive part (see Fig. 2.20) of the CVSM provides a reference voltage $\hat{v}$ for the virtual impedance. The value of this voltage depends from the voltage setpoint V_{set} and the effect of a proportional control of the reactive power with coefficient D_q. This means that no zero-error tracking of the reactive power reference is possible in every condition.

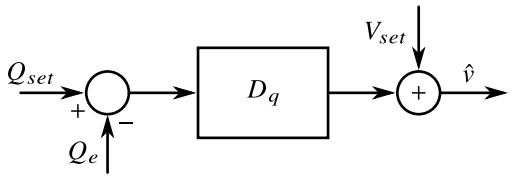

Figure 2.20: Reactive part of the CVSM.

As in many other solutions, the active and reactive power feedback P_e, Q_e are calculated from the converter current i_i and the grid voltage v_g as follows:

$$P_e + jQ_e = 3/2 \left(v_{gd} + jv_{gq}\right) \left(i_{id} - ji_{iq}\right) \tag{2.29}$$

Starting from the voltage reference $\hat{v}$, the measured current i_i and the virtual speed ω_r, the reference voltage v_g^* for the voltage controller is calculated by the virtual impedance shown in Fig. 2.21.

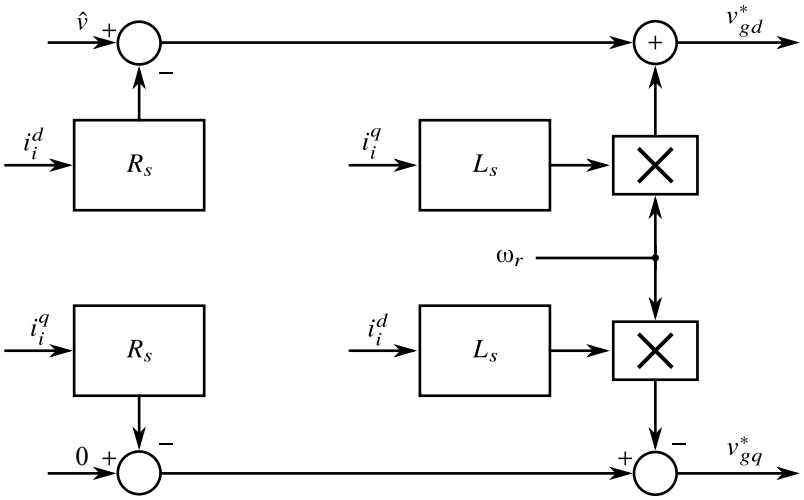

Figure 2.21: Virtual impedance of the CVSM.

This virtual impedance is implemented in the (d,q) frame by neglecting the derivatives of the current and preserving only the motional cross terms. This simplifies the implementation, but introduces a wrong behavior for frequencies different than the fundamental. This can be easily observed by comparing the full implementation and this simplified one at the negative sequence (corresponding to twice the fundamental frequency in the (d,q) frame).

In the Laplace domain, the full implementation of a RL impedance, supplied by a voltage v, expressed in the (d,q) frame is:

$$v_{dq} = Ri_{dq} + j\omega Li_{dq} + sLi_{dq} \tag{2.30}$$

If supplied by a negative sequence voltage at frequency -2ω, the equivalent impedance is:

$$v_{dq} = Ri_{dq} + j\omega Li_{dq} - 2j\omega Li_{dq} \tag{2.31}$$

resulting to an impedance equal to $R - j\omega L$.

On the other hand, the simplified impedance, not having the derivative term, results to a value of $R + j\omega L$. This means that the negative sequence behavior of this VSM is exactly the opposite (in terms of phase) of the one to be expected from SGs.

Finally, the VSM employs a cascaded voltage and current control, therefore limiting the current injection in case of faults. This solution is effective, however reduces the overall bandwidth of the system and involves a more complex tuning procedure, compared to other models with a single control loop.

In summary, the CVSM has the following features:

- Is a hybrid between a voltage source and a current source VSM;
- Is equipped with a damping based on the PLL measurement, therefore decoupling the damping and the active droop actions;
- Does not have an error free tracking of the reactive power reference, implementing a simple proportional control;
- Implements a simplified virtual impedance, neglecting the derivative terms. This simplifies the implementation, but features an incorrect behavior when supplied with voltage harmonics and negative sequence components;
- Presents two cascaded regulation layers (voltage and current), being therefore to protect the converter in case of faults. However, this reduces the bandwidth and introduce more complexity in the tuning procedure.

2.8 Conclusions of the VSM Overview

The literature provides us with numerous SG emulation solutions. It is, therefore, important to compare them under each of the ancillary services aspects, in order to select the most appropriate for the practical implementation.

The following Table 2.1 summarizes the different solutions presented in this chapter and can represent a useful reference.

Table 2.1: Summary of the Literature Review of the Main Existing VSM Strategies

Model	Model Type	Damping-Droop	Stator Emulation	Current Limitation	PLL Needed
VISMA	Current	No	Full	Yes	No
VISMA I	Current	Depending on $f(s)$	Full	Yes	No
VISMA II	Current	Depending on $f(s)$	Full with derivative	No	No
Synchronverter Base	Voltage	Yes	Physical Filter	No	Yes
Synchronverter Self-Sync	Voltage	Yes	Physical Filter	No	No
SPC Base	Current	Yes	Full	Yes	No
SPC PI	Current	No	Full	Yes	No
SPC L-L	Current	Tunable	Full	Yes	No
Osaka	Voltage	No	Physical Filter	Yes	Yes
KHI	Current	No	Partial	Yes	Yes
VSYNC	Current	No	None	Yes	Yes
CVSM	Hybrid	No	Partial	Yes	Yes

Chapter 3

Simplified Virtual Synchronous Compensator (S-VSC)

This thesis proposes the Simplified Virtual Synchronous Compensator (S-VSC) as a valid VSM solution. In this chapter, S-VSC model is presented and described in its features and composing parts. This chapter is organized as follows:

- Initially, it is described how this model is integrated into the control of a grid-tied converter;
- The proposed S-VSC is described in its every part, with a special focus on the electromechanical damping and the design and tuning of the reactive power control. This section will also contain specific experimental results relative to the damping methods;
- This model belongs to the current source category presented in chapter 2. Therefore, a section is devoted to the adopted current controller and its limitation strategy.

The contents of this chapter have been partially published in [82–86].

3.1 Model Integration in Inverter Control

The S-VSC is a VSM control strategy intended for an inverter interfaced to the electric grid by means of an LCL filter, as shown in Fig. 3.1. In this thesis, the inverter dc link is provided by a constant dc voltage source. This dc voltage can be provided e.g. by a renewable energy source integrated with a storage system or the storage system of a fast charging station.

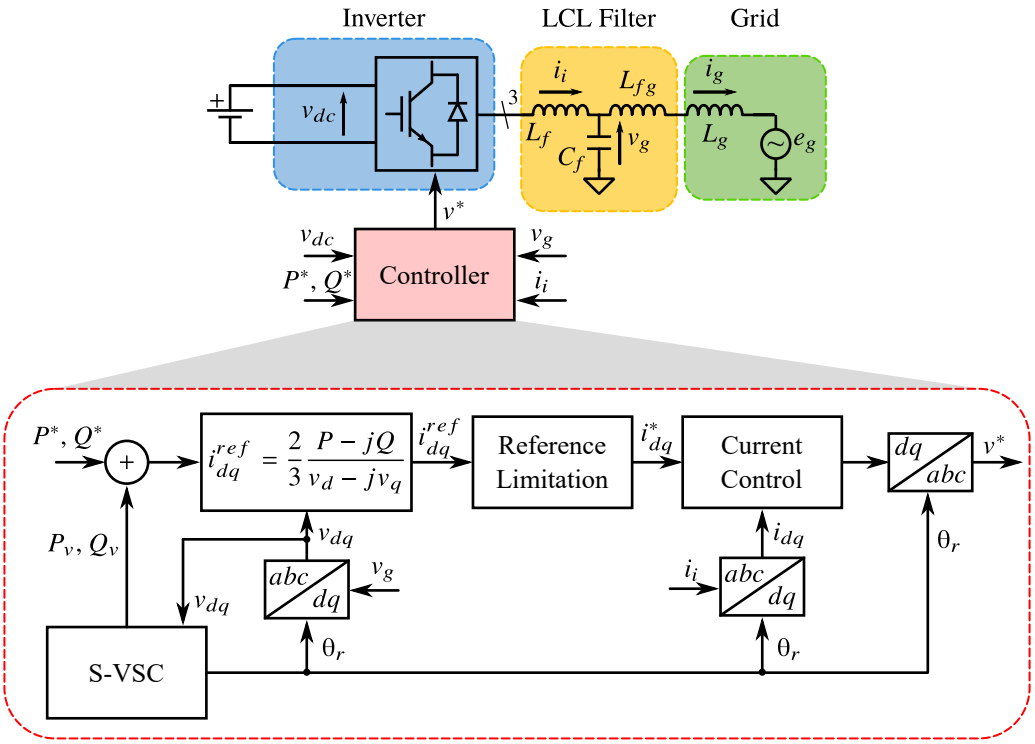

Figure 3.1: Integration of the proposed S-VSC into the control of a current-controlled inverter.

The inverter control system measures the output current i_i of the inverter, the line-line (or phase-neutral) voltage across the filter capacitors v_g and the dc side voltage v_{dc}. Any modulation strategy can be used and does not alter the behavior of the S-VSC, since it only influences the high frequency (switching frequency and above) behavior of the system. Therefore, in this thesis the output of the controller is the moving average voltage reference of the converter v^*, which is considered to be applied ideally. This assumption is reasonable when studying VSMs, as the frequencies of the VSM (e.g. mechanical emulation) are orders of magnitude smaller (Hz) than the switching of the converter (kHz range). The two aspects are therefore fully decoupled. In practice, this moving average voltage reference is then transformed into gate driving signals for the power switches by applying any of the modulation techniques available in the technical literature [87].

The innermost control loop is the converter current controller, which receives the reference currents from the higher level VSM logic. These references are the sum of the external power setpoints (e.g. coming from a grid voltage or frequency control) and the S-VSC currents, in charge of compensating any grid perturbation (e.g. frequency or voltage variation, harmonics...). The S-VSC is the source of grid synchronization for the current control (with the virtual rotor angle θ_r). In fact, thanks to the inertia of the virtual rotor, the S-VSC provides a stable and filtered grid angle measurement. Therefore, a PLL is not needed for the operation.

The block "Reference Limitation" is in charge of limiting the amplitude of the reference current vector to comply with the inverter ratings in all cases (even during faults and grid abnormal conditions).

3.2 Model Description

To describe the S-VSC structure, it is practical to introduce a simplified diagram of the converter and control assembly. This diagram assumes that the inverter behaves as an ideal current source, injecting exactly its reference values into the grid. The system is therefore represented as in Fig. 3.2. The hardware part is modeled by a controlled current source i_i^* connected to the grid through a CL filter. This current source is generated from the external power setpoints and the S-VSC virtual powers.

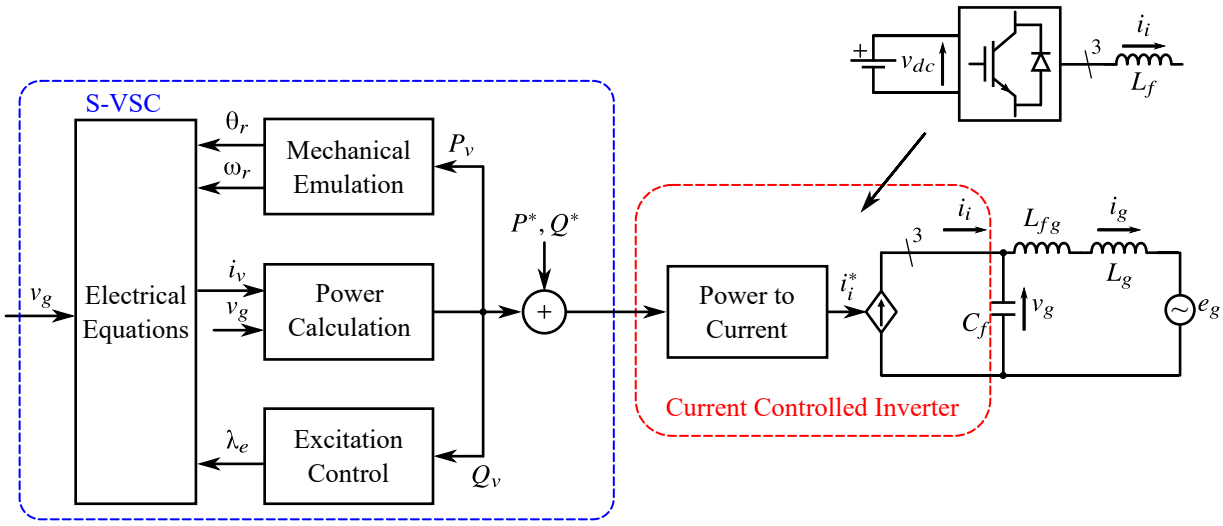

Figure 3.2: Equivalent of the proposed S-VSC embedded into a current-controlled inverter.

The S-VSC is therefore a voltage-input, power-output model. The input voltage v_g is measured across the LCL filter capacitor C_f. The S-VSC is organized in several blocks, each in charge of a specific aspect of the VSM:

1. Power calculation: calculation of the active and reactive power of the S-VSC from its currents and the grid voltages;

2. Mechanical emulation: this is the virtual rotor of the machine. This block provides the virtual speed ω_r and angle θ_r of the VSM and frequency support to the grid;

3. Excitation control: reactive channel management, virtual excitation flux control for reactive support during faults and short circuit current injection;

4. Electrical equations: Virtual stator and optional virtual dampers. Provides tunable harmonic compensation.

In this thesis, the per unit notation was adopted. The following base values are used: base angular speed ω_b (i.e., nominal grid angular frequency), base power S_b (power rating of the converter) and base voltage V_b (peak value of the phase voltage).

3.2.1 Power Calculation

This block calculates the feedback virtual active power P_v and virtual reactive power Q_v for the S-VSC model. These virtual powers are calculated from the virtual machine currents i_v, not using the actual inverter currents i_i. This guarantees higher immunity against the measurement uncertainties and avoids the introduction of non-linear effects due to the current saturation in case of inverter overload. The virtual powers are assumed to be tracked by the converter control with zero error. This assumption is valid since the bandwidth of this controller is much larger than the power variations of the S-VSC (hundreds of Hz vs Hz).

The virtual active and reactive powers of the S-VSC are calculated from the measured grid voltage and the S-VSC virtual currents as:

$$P_v + j \cdot Q_v = \left(v_{gd} + j v_{gd}\right)\left(i_{vd} - j i_{vq}\right) \tag{3.1}$$

3.2.2 Mechanical Emulation

This is the key part of the S-VSC. In fact, it is in charge of the synchronization with the grid (providing a measurement of both the grid frequency ω_r and angle θ_r) for the converter controller. In the S-VSC model, a simplified version of the synchronous generators swing equation is implemented. The well-known swing equation [2]:

$$P_m - P_e = 2H\frac{d(\omega_r - \omega_g)}{dt} + D_p(\omega_r - \omega_g) \tag{3.2}$$

is here simplified by removing the damping term $D_p(\omega_r - \omega_g)$. The electrical feedback power P_e is here the virtual machine power P_v and the prime mover mechanical power P_m becomes the virtual reference active power P_v^*. The result is depicted in the block diagram of Fig. 3.3.

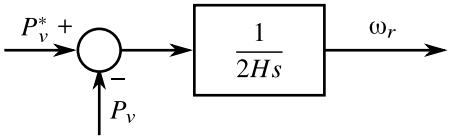

Figure 3.3: Simplified swing equation block diagram used in the S-VSC.

3.2.3 Current References Generation

A novelty of the S-VSC is that it always operates with zero power references (i.e. $P_v^* = Q_v^* = 0$). The active and reactive power setpoints are processed directly by the inverter control loops and the virtual machine is only in charge of generating compensation references to provide grid ancillary services (virtual inertia, reactive support, harmonic compensation). The advantage can be explained with the load angle characteristic (P_v, δ) [2] of a SG, depicted in Fig. 3.4. The stable operating region of a synchronous machine corresponds to the load angle interval $(-\pi/2, \pi/2)$. The VSG models available in the literature operate over this whole stable region, changing radically their load angle according to the needed active power flow. On the other hand, the S-VSC always operates around the point $\delta = 0$, at nearly-zero active power (i.e., $P_v^* = 0$, $P_v \approx 0$). Therefore, when the active power transfer to the grid must change, only the converter control loops vary their operating point. The S-VSC does not change its load angle and it operates in parallel with the converter, similarly to a synchronous condenser, just injecting fractions of its nominal active power during grid transients. Moreover, in the S-VSC also the virtual speed ω_r does not change significantly, as the virtual rotor does not have to modify its position with respect to the grid voltage vector. This leads to a better quality of the grid frequency estimation, when using the S-VSC virtual speed, even during load transients. Moreover, this leads to improved both small signal and large signal stability [2], as more angle margin during grid faults is available.

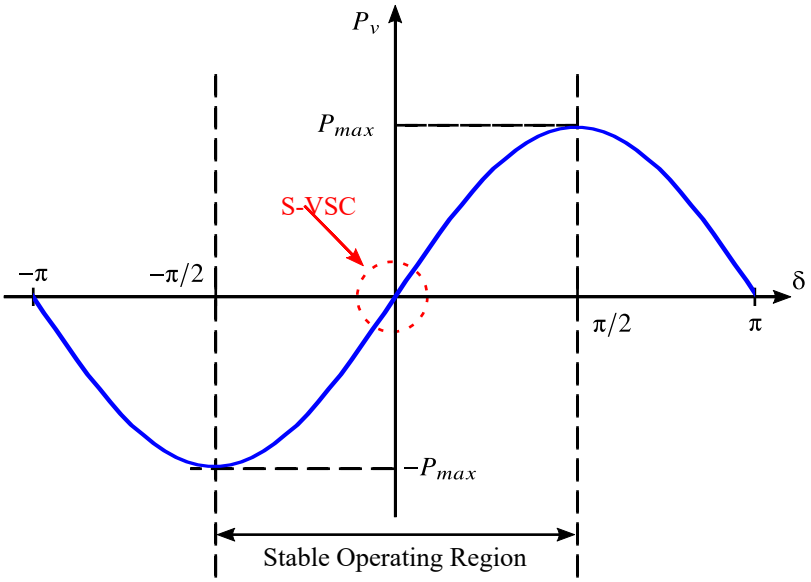

Figure 3.4: Power angle relationship of a SG and the operating area of the S-VSC.

The current reference i_{dq}^{ref} for the inner controller is then derived from the sum of the external power setpoints PQ^* and the S-VSC compensating power references PQ_v,

according to:

$$i_{dq}^{ref} = \frac{P^* + P_v - j(Q^* + Q_v)}{v_d - jv_q} \tag{3.3}$$

and are then limited to comply with the converter rating as it will be explained in section 3.6.1.

The advantages of this structure will be experimentally demonstrated in chapter 4.

3.2.4 Electrical and Magnetic Equations

The electrical equations of the S-VSC emulate a virtual stator in the (*d*,*q*) rotating frame and optionally include a simplified damper winding on the *q*-axis, as it will be described in section 3.3.4.

As for real electrical machines, the excitation flux acts on the *d*-axis (reactive axis), while the *q*-axis deals with the active power (torque). This is a slight difference compared to traditional PLL-oriented grid-tied converters, which relate the *d*-axis with the active power (in phase with the grid voltage) and the *q*-axis with the reactive power (in quadrature).

The equivalent circuits of the S-VSC electrical part are depicted in Fig. 3.5a (*d*-axis) and Fig. 3.5b (*q*-axis). Such equivalent circuits are similar to the ones found in the traditional modeling of synchronous alternators [2].

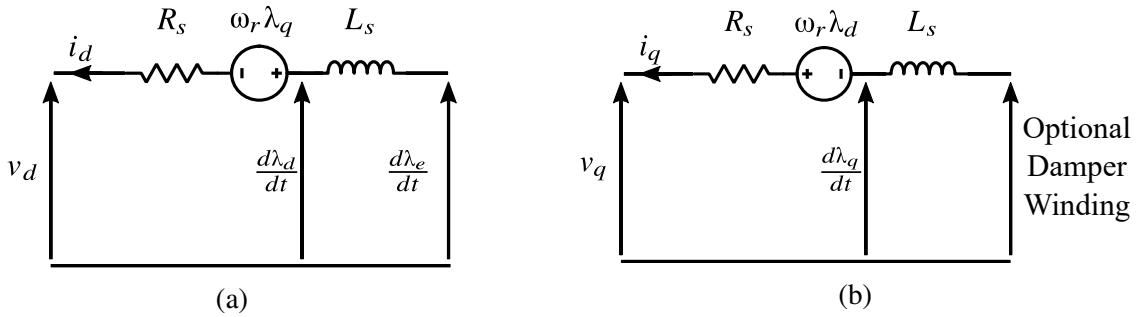

Figure 3.5: Equivalent circuits of the S-VSC in the rotating (*d*,*q*) frame. From left to right:
a) S-VSC *d*-axis equivalent circuit;
b) S-VSC *q*-axis equivalent circuit.

Compared to synchronous alternators, the non ideal (e.g. saturation) and other unnecessary features for the synchronous machine emulation have been excluded (e.g., damper windings on both axes, dynamics of the excitation winding). It can be seen that the *d*-axis circuit comprises the excitation flux linkage λ_e.

The resulting electrical equations of the virtual machine are as follows:

$$\begin{aligned} v_d &= -R_s i_d - \omega_r \lambda_q + \frac{1}{\omega_b}\frac{d\lambda_d}{dt} \\ v_q &= -R_s i_q + \omega_r \lambda_d + \frac{1}{\omega_b}\frac{d\lambda_q}{dt} \end{aligned} \tag{3.4}$$

where R_s is the stator virtual resistance and λ_d and λ_q are the virtual stator flux linkages; ω_b is the base angular speed.

The virtual currents i_d and i_q of the S-VSC can be calculated through the inverse magnetic model of the machine (here without the simplified damper winding on the q-axis) as follows:

$$\begin{aligned} i_d &= \frac{\lambda_e - \lambda_d}{L_s} \\ i_q &= -\frac{\lambda_q}{L_s} \end{aligned} \tag{3.5}$$

The electrical and magnetic part of the S-VSC can be modified according to the selected damping method, as it will be described in detail in Section 3.3.

3.2.5 Harmonic Compensation

The S-VSC virtual stator also embeds a harmonic compensation feature. Just as real synchronous machines do, also the S-VSC is able to generate compensating current references to counteract harmonic distortions of the grid voltage. The virtual stator can be represented in the stationary (α,β) frame as in Fig.3.6. In fact, at steady state it acts as a virtual inductance L_s (the resistance R_s is usually much lower and is therefore neglected). Therefore, this virtual stator circuit, when supplied by a grid voltage including n arbitrary harmonic distortions of order h, generates harmonic current references that are as follows in the stationary (α,β) frame:

$$i_h^{\alpha\beta} = \frac{v_h^{\alpha\beta}}{h\omega_g L_s}, \quad h = 1 \ldots n \tag{3.6}$$

This means that the S-VSC is able to generate a compensating current, that is inversely proportional to the virtual stator inductance L_s. Since the virtual stator inductance is tunable, the magnitude of the injected current can be varied. It must be noted that a suitable current controller is needed to track high order harmonics current references.

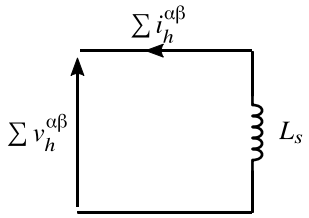

Figure 3.6: Equivalent circuit at steady state for harmonic compensation in the equivalent (α,β) frame.

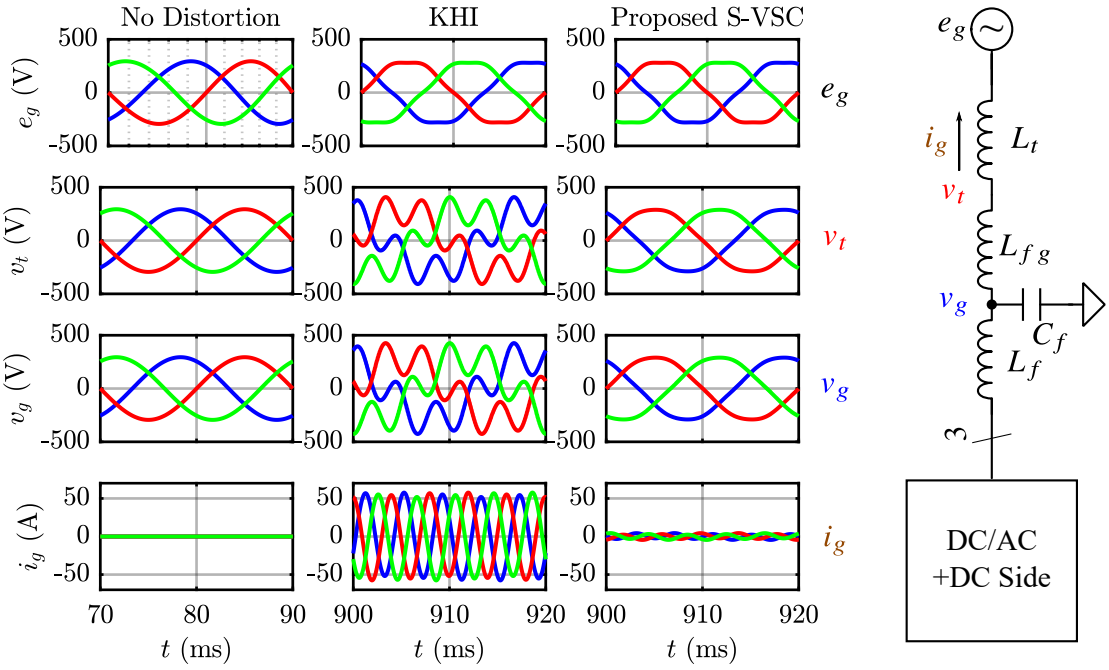

Figure 3.7: Simulation comparison of the proposed S-VSC with the existing KHI model.

The tunable harmonic compensation feature has been tested in simulation (due to the complexity of the experimental setup) with an existing VSG model: the KHI [59]. The following system has been considered:

- A three-phase converter with ideal DC source equipped with an LCL grid-side filter (same parameters as the experimental setup listed in Tab. 4.1);
- A transformer to interface the generating plant with the grid. It has been modeled with its equivalent inductance L_t = 0.1 pu;
- Both models have been tuned with equivalent parameters (inertia, damping, virtual stator...);

- The converter was modeled with average values. An accurate modeling of the PWM modulation is in fact not necessary when dealing with lower frequency phenomena, such as the harmonic distortion;
- Both controllers were implemented in digital form and the equivalent delay of the digital controller and PWM modulation was included as well;
- Both systems were equipped with the same PI+RES current controller, as described in Section 3.6.2;
- Both models were operating at no load in order to clearly identify the differences among them.

To compare the two systems, a 5% 5th harmonic voltage perturbation has been applied to the grid (e_g). The voltage shapes at different points (v_t, v_g) and the current injected into the grid were compared and the results are displayed in Fig. 3.7. Both models behave equally under ideal grid conditions (left column), by injecting no current. The voltage is not distorted in any point. When the voltage perturbation is applied (central and right column) both systems inject current at the disturbance frequency. However, the KHI model, being implemented with an algebraic virtual stator, injects very large currents that further contribute to the voltage distortion. On the other hand, the proposed S-VSC (right column) is injecting smaller currents according to (3.6). Such currents are effective in compensating the voltage distortion. As it can be seen in Fig. 3.7, both the line-line voltages v_t and v_g do not feature the typical peak shaving caused by the 5th harmonic, but have a more sinusoidal shape.

3.2.6 Excitation control

The last core block of the S-VSC is represented by the excitation control. This block deals with the reactive power management of the machine. In summary, this block acts as an integral controller of the reactive power, generating the virtual excitation flux linkage λ_e for the VSM electrical part. This block is crucial during voltage dips and short circuits, as its action provides the necessary excitation flux to inject or absorb reactive power towards the grid to support the voltage and trigger the short circuit relays.

This block will be described in detail in section 3.4.

3.3 Electromechanical Damping

As mentioned in section 1.2, the first key aspect of a VSM is the electromechanical emulation. This means that the VSM must:

- Provide **virtual inertia**: active power injection proportional to the inverse of the grid frequency derivative;

- Feature a **damped behavior**: the virtual rotor speed and the active power exchanged with the grid must not oscillate;
- **Track** the grid **frequency**, providing the best estimate possible;
- Be as **little** as possible **sensitive** to **faulty grid** conditions which do not affect the actual grid frequency (e.g. voltage dips).

Therefore, particular care must be devoted to the electromechanical implementation of the VSM. In this section three conventional damping solutions will be presented and analyzed. Then, two original damping solutions are proposed for the S-VSC:

1. **Droop-based damping**: Damping action proportional to the virtual speed error from nominal value (Conventional);
2. **PLL-based damping**: damping power proportional to the speed error from measured grid frequency (Conventional);
3. **PI-based damping**: a PI regulator is used in place of the machine virtual rotor (Conventional);
4. **RQ-damping**: emulation of a simplified virtual damper winding on the machine q-axis (**Proposed**);
5. **Lead-lag-damping**: A lead-lag filter acts on the active power feedback of the electromechanical loop (**Proposed**).

In the following subsections these damping strategies will be presented, as well as the relative tuning procedure. In each case, the tuning procedure starts with the inertia constant H, the damping factor ζ and the virtual stator inductance L_s given as target parameters. Finally, they will be validated experimentally and their performance compared.

3.3.1 Droop-Based Damping

The simplest solution available to provide electromechanical damping to a VSM is the droop-based damping and it is adopted by several models in the literature, such as [32, 56, 88]. This method implements the well known swing equation of synchronous generators [2]:

$$P_m - P_e = 2H\frac{d(\omega_r - \omega_g)}{dt} + D_p(\omega_r - \omega_g) \tag{3.7}$$

imposing the grid frequency ω_g to its nominal value ω_n. This means that the virtual speed ω_r and virtual rotor angle θ_r are calculated from the reference power P^* and the virtual

feedback power P_v as follows:

$$\begin{aligned} 2H\frac{\omega_r}{dt} &= P^* - P_v - D_p(\omega_r - \omega_n) \\ \frac{d(\theta_r)}{dt} &= \omega_r \end{aligned} \tag{3.8}$$

The resulting block diagram of the mechanical part is shown in Fig. 3.8. The damping power P_d is a feedback which ensures proper damping of the virtual machine.

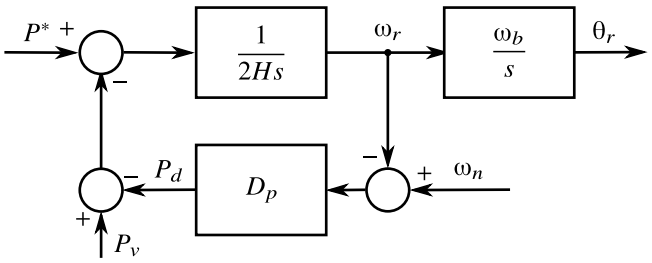

Figure 3.8: Block diagram of the mechanical part of a VSM using Droop-based damping.

This damping solution features the following characteristics:

- The damping action is proportional to the frequency error from its nominal value, therefore an active droop effect is embedded into this solution;
- It does not rely on the measurement of the grid voltage;
- It is highly immune from disturbances, as there is not a direct feedback from the grid;
- It is the simplest damping algorithm.

However, it is affected by the major drawback of coupling the damping with an active droop control effect. This aspect will be further explained in section 3.3.6.

Tuning Procedure

The tuning procedure of D_p is based on the electromechanical linearized model of synchronous machines, available in the technical literature [2]. From the linearized swing equation, the following block diagram of Fig. 3.9 can be obtained.

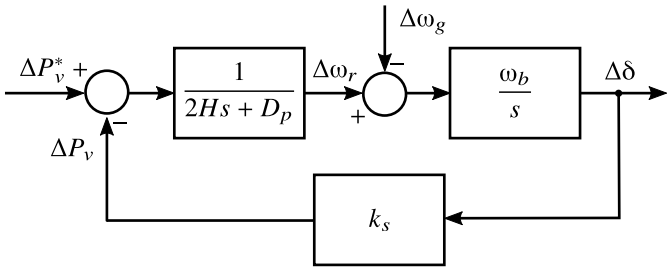

Figure 3.9: Linearized model of the electromechanical behavior of the S-VSC with the Droop-based damping.

The parameter k_s is the synchronizing power, equal to the maximum active power that can be exchanged with the grid in case of a mainly inductive connection ($k_s = EV/X_{tot}$).

The characteristic equation of the linearized model of Fig. 3.9 is:

$$2Hs^2 + D_p s + \omega_b k_s = 0 \tag{3.9}$$

By comparing (3.9) with the characteristic equation of a generic second order system (two complex poles defined by their damping ζ and natural frequency ω_0):

$$s^2 + 2\zeta\omega_0 s + \omega_0^2 = s^2 + \frac{D_p}{2H}s + \frac{\omega_b k_s}{2H} \tag{3.10}$$

the value of D_p is therefore obtained as:

$$D_p = \zeta\sqrt{8H\omega_b k_s} \tag{3.11}$$

3.3.2 PLL-Based Damping

A second widespread solution [69, 88] is to use the grid frequency measured by a PLL instead of its nominal value. The implementation of this method is similar to the droop-based damping presented in Section 3.3.1. In the swing equation (3.7), the measured grid frequency ω_{PLL} is used instead of its nominal value ω_n. The resulting block diagram of the mechanical part is shown in Fig. 3.10.

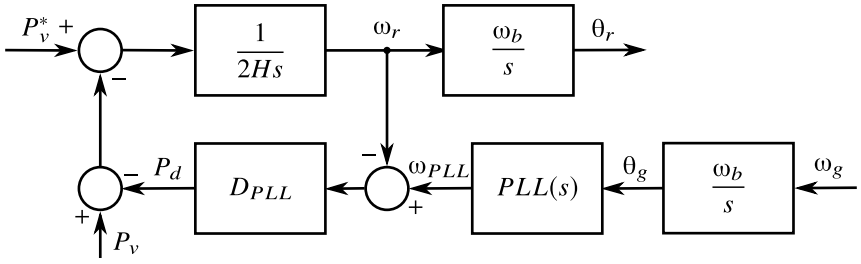

Figure 3.10: Block diagram of the mechanical part of a VSM using PLL-based damping.

The PLL behavior is modeled by the $PLL(s)$ transfer function. In this thesis a standard PLL structure has been considered, as shown in Fig. 3.11.

This PLL structure is equivalent to the diagram of Fig. 3.12, relating directly the grid frequency ω_g to the speed measured by the PLL ω_{PLL}. The overall transfer function of the PLL can be therefore easily calculated as:

$$\frac{\Delta\omega_{PLL}}{\Delta\theta_g} = PLL(s) = \frac{s\left(sk_p^{PLL} + k_i^{PLL}\right)}{s^2 + s\omega_b k_p^{PLL} + \omega_b k_i^{PLL}} \tag{3.12}$$

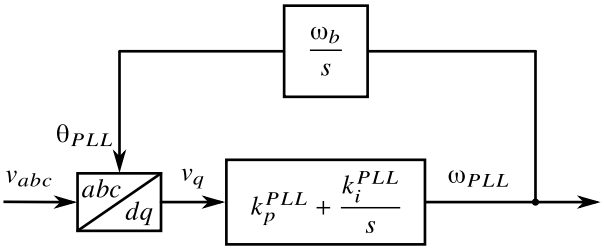

Figure 3.11: Block diagram of the considered PLL for PLL-based damping.

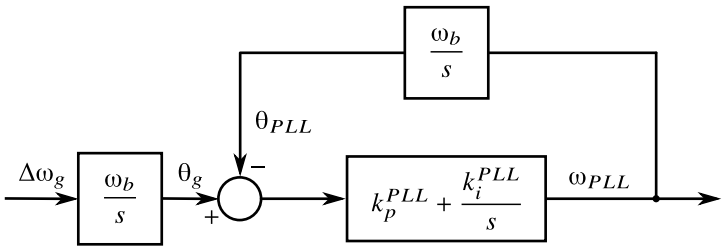

Figure 3.12: Equivalent block diagram of the considered PLL.

This solution features the following characteristics:

- The damping action is **independent from the active droop action**. Therefore, the primary regulation is an optional feature, similarly to the reality of contemporary power systems. Moreover, the frequency droop coefficients can be chosen to satisfy the power system needs, not being mixed with the damping coefficient;
- A **PLL** is **needed** to measure the grid frequency ω_{PLL}. Therefore its dynamics influences the VSM, introducing sensitivity to harmonics, distortions and abrupt grid voltage vector variations.

Tuning Procedure

The tuning procedure is equivalent to the already presented one for the droop-based damping. A correction coefficient is however necessary. This correction factor, depending on the machine and grid inductances, is obtained from empirical considerations and from the existing literature [69]. The value of damping coefficient D_{PLL} is therefore obtained as follows:

$$D_{PLL} = D_p \frac{L_s + L_g}{L_s} = \zeta \sqrt{8H\omega_b k_s} \frac{L_s + L_g}{L_s} \tag{3.13}$$

3.3.3 PI-Based Damping

The PI-based damping employs a Proportional-Integral regulator to eliminate the steady-state active power error of the VSM. As mentioned in the comparison section, this solution is also employed by other VSM strategies (i.e. SPC [56]). It is here applied and described to provide a term of comparison with the other presented damping solutions.

The block diagram of this solution is depicted in Fig. 3.13. The PI regulator $PI(s)$ is defined as:

$$PI(s) = k_d + \frac{k_h}{s} \tag{3.14}$$

where k_d is the proportional term, providing damping, and k_h is the integral one, in charge of the inertial action.

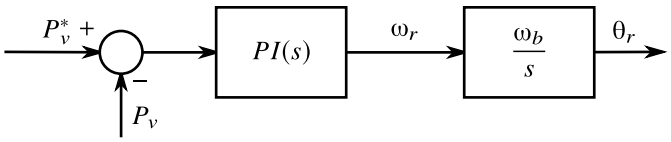

Figure 3.13: PI-based damping block diagram.

The benefits of this damping method are the following:

- **No embedded droop** characteristic (as in the PLL-based damping);
- **No PLL** is needed.

However, this damping method features a high sensitivity to disturbances in the grid voltage. This is due to the proportional term of the regulator, which does not filter the input disturbances.

Tuning Procedure

The two parameters of the PI regulator k_d and k_h must be tuned in order to ensure the proper damping and inertia to the virtual machine. The tuning procedure is similar

to the one of the droop-based and PLL-based. By applying this damping method to the linearized model of the VSM, the following block diagram of Fig. 3.14 is obtained.

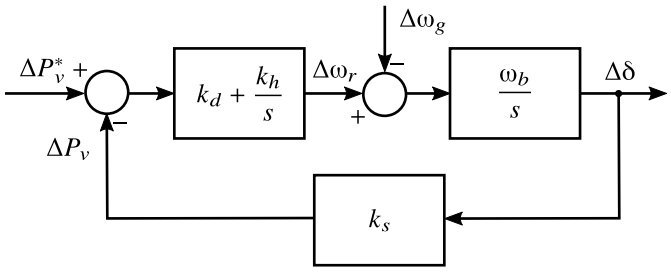

Figure 3.14: Linearized model of the electromechanical behavior of the S-VSC equipped with the PI-based damping.

First, the integral gain k_h of the PI is calculated by comparison with the generic virtual rotor mechanical equation of a synchronous machine. This term provides in fact the inertial active power contribution to the VSM. Therefore:

$$k_h = \frac{1}{2H} \tag{3.15}$$

The proportional gain is tuned from the characteristic equation of the linearized model of Fig. 3.14:

$$1 + PI(s)\frac{\omega_b}{s}k_s = 0 \tag{3.16}$$

Equation (3.16) can be rearranged to obtain the following:

$$s^2 + k_d k_s \omega_b s + k_i k_s \omega_b = 0 \tag{3.17}$$

The obtained characteristic equation can be compared with a generic second order system:

$$s^2 + 2\zeta\omega_0 s + \omega_0^2 = 0 \tag{3.18}$$

This characteristic equation features two complex poles defined by their damping ζ and natural frequency ω_0.

By comparing (3.18) and (3.17), the following relationships are found:

$$\begin{aligned} 2\zeta\omega_0 &= k_d k_s \omega_b \\ \omega_0^2 &= k_i k_s \omega_b \end{aligned} \tag{3.19}$$

It can be easily obtained that:

$$\begin{aligned} k_d &= 2\zeta\sqrt{\frac{k_h}{k_s\omega_b}} \\ k_h &= \frac{1}{2H} \end{aligned} \tag{3.20}$$

which are the final tuning values for the PI-based damping.

3.3.4 RQ Simplified Damper Winding

Synchronous generators employ damper windings to provide the necessary electromechanical damping to the machine. The earlier VSM models [40] proposed a full emulation of such dampers in the virtual rotor (d,q) frame. This solution is effective, but it requires an accurate modeling of the physical structure of the synchronous generator. Therefore, this thesis proposes a **simplified virtual damper winding on the machine q-axis**. This solution guarantees **satisfactory damping performance** and **reduces the complexity** of the model to be implemented, as well as the number of parameters to be tuned.

This solution features the following benefits:

- The **damping** action is **independent from the active droop action**. Therefore, the primary regulation is an optional feature, similarly to the reality of contemporary power systems. Moreover, the frequency droop coefficients can be chosen to satisfy the power system needs, not being related to the damping requirements;
- A **PLL** is **not required** during the operation and the virtual rotor angle can be employed to generate the reference frame for the inverter inner current control;
- The q-axis damper does not interact with the d-axis virtual excitation control;
- The simplified damper winding is a **physical-based concept**, which leads to a better understanding for practicing engineers.

Damper Model Description

The description of the proposed virtual damper winding starts from the winding diagram of the VSM, depicted in Fig. 3.15a. This damping method consists in adding an extra winding on the machine q-axis and, therefore, modifying the electrical equations and the q-axis magnetic model of the VSM. The VSM swing equation does not feature any damping term and can be described by the block diagram of Fig. 3.15b.

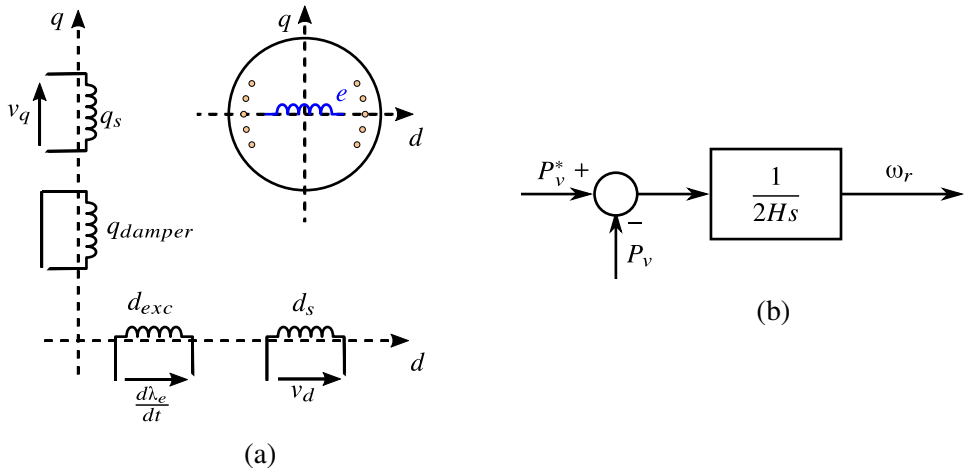

Figure 3.15: S-VSC model with the RQ-damping method. From left to right:
a) Winding diagram and rotor section of the S-VSC in the rotor (d,q) frame. d_s and q_s are the stator windings, q_{damper} and d_{exc} the rotor windings. They represent the q-axis damper and the equivalent excitation winding, respectively;
b) Simplified swing equation diagram when using the proposed simplified q-axis damper winding.

The d_{exc} winding on the d-axis represents the excitation of the virtual machine, while the q_{damper} winding on the q-axis provides the damping. The stator windings are modeled as explained in section 3.2.4. The details of the excitation winding will be described in later sections.

The per unit electric equation of the damper winding is the well known electrical equation of a generic short-circuited winding:

$$v_{rq} = R_{rq} i_{rq} + \frac{1}{\omega_b} \frac{d\lambda_{rq}}{dt} \tag{3.21}$$

where v_{rq} is the voltage at the terminals of the damper winding, R_{rq} is the virtual damper winding resistance, i_{rq} the current through the damper winding and λ_{rq} the damper winding flux linkage. ω_b represents the base angular speed of the system.

Being the damper winding short-circuited, $v_{rq} = 0$. This way, (3.21) can be written as:

$$\frac{d\lambda_{rq}}{dt} = -\omega_b R_{rq} i_{rq} \tag{3.22}$$

At this point, the damper winding time constant τ_{rq0} can be defined:

$$\tau_{rq0} = \frac{L_{rq}}{\omega_b R_{rq}} \tag{3.23}$$

where L_{rq} represents the damper winding inductance. Therefore, (3.22) can be expressed as:

$$\tau_{rq0} \frac{d\lambda_{rq}}{dt} = -L_{rq} i_{rq} \tag{3.24}$$

It is useful to describe this damper winding with an equivalent circuit of the q-axis as in Fig. 3.16. This equivalent circuit shows the additional current term in the q-axis, due to the damper winding.

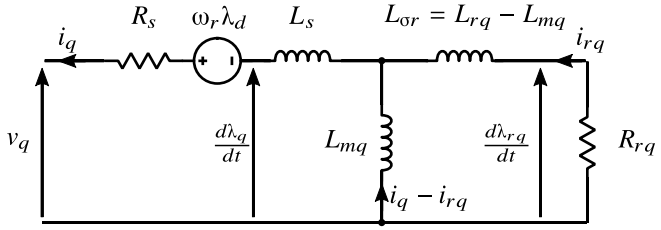

Figure 3.16: Simplified equivalent q-axis equivalent circuit.

Since VSMs are virtual models, with no physical limitations, the virtual damper winding leakage inductance $L_{\sigma r}$ can be arbitrarily imposed to 0, by defining the mutual inductance L_{mq} equal to the damper winding inductance L_{rq}. Therefore, the equivalent circuit of Fig. 3.16 is simplified as shown in Fig. 3.17.

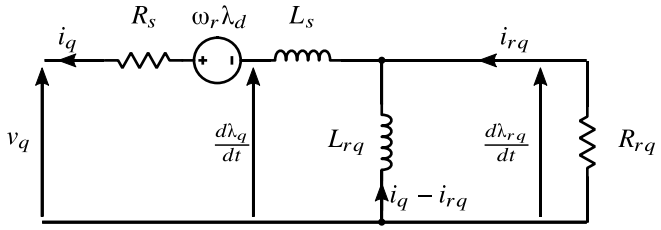

Figure 3.17: Simplified equivalent q-axis equivalent circuit.

After this simplification, the damper current can be written:

$$\lambda_{rq} = -(i_q - i_{rq})L_{rq}$$

$$i_{rq} = \frac{\lambda_{rq}}{L_{rq}} + i_q \tag{3.25}$$

By substituting (3.25) in (3.24):

$$\tau_{rq0}\frac{d\lambda_{rq}}{dt} = -L_{rq}(\frac{\lambda_{rq}}{L_{rq}} + i_q)$$

$$\tau_{rq0}\frac{d\lambda_{rq}}{dt} = -(\lambda_{rq} + L_{rq}i_q) \tag{3.26}$$

The q-axis current therefore contains an additional term with respect to (3.5):

$$i_q = \frac{\lambda_{rq} - \lambda_q}{L_q} \tag{3.27}$$

The set of equations (3.26), (3.27) is therefore complete and fully describes this damping method. It must be noted that the d-axis equations are not influenced, as the proposed q-axis damper winding does not interact with the d-axis. This way, the behavior of the reactive control, acting on the d-axis, is not affected by the presence of the damper and can be therefore tuned to guarantee the desired dynamic reactive response.

Tuning Procedure

After having presented the RQ-based damping model, the two parameters of the virtual damper winding τ_{rq0} and the total q-axis inductance $L_{qt} = L_s + L_{rq}$ must be tuned in order to ensure the proper damping to the virtual machine. The tuning procedure is based on the linearized model of the S-VSC as described in Fig. 3.18.

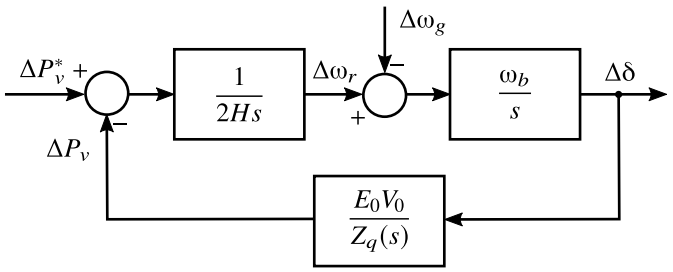

Figure 3.18: Linearized model of the electromechanical behavior of the S-VSC with the RQ-based damping.

First, starting from the simplified q-axis equivalent circuit of Fig. 3.17, the total q-axis equivalent impedance $Z_q(s)$ of the machine can be derived:

$$\begin{aligned} Z_q(s) &= L_s + L_{rq}//R_{rq} \\ Z_q(s) &= L_{qt}\frac{1+s\tau_{rq}}{1+s\tau_{rq0}} \end{aligned} \tag{3.28}$$

where $\tau_{rq} = \tau_{rq0}(L_s/L_{qt})$ is the short circuit time constant of the virtual machine.

The effect of the grid inductance L_g can also be included in Z_q, in order to consider the effects of different connection points. In this case, the external value of the grid can be simply added to L_s.

The advantage of writing this equivalent impedance Z_q is that a straightforward q-axis magnetic equation can be written as:

$$\frac{d\lambda_q}{dt} = -Z_q(s)i_q \tag{3.29}$$

The characteristic equation of this linearized system can be now derived as follows:

$$1 + \frac{\omega_n}{2Hs^2}\frac{V_0^2}{Z_q} = 0 \tag{3.30}$$

Equation (3.30) can be rearranged to obtain the following:

$$s^3 + \frac{1}{\tau_{rq}} s^2 + \frac{\omega_n V_0^2}{2H(L_s + L_g)} s + \frac{\omega_n V_0^2}{2H(L_s + L_g)\tau_{rq0}} = 0 \tag{3.31}$$

and the following terms can be defined:

$$\begin{aligned} a_{RQ} &= \frac{(L_{qt} + L_g)}{\tau_{rq0}(L_s + L_g)} \\ b_{RQ} &= \frac{\omega_n V_0^2}{2H(L_s + L_g)} \end{aligned} \tag{3.32}$$

The obtained characteristic equation (3.31) can be generically rewritten as:

$$(s^2 + 2\zeta\omega_0 s + \omega_0^2)(s + p_r) = 0 \tag{3.33}$$

This characteristic equation features two complex poles defined by their damping ζ and natural frequency ω_0 and one real pole $-p_r$.

By comparing (3.33) and (3.31), the following relationships are found:

$$\begin{aligned} a_{RQ} &= p_r + 2\zeta\omega_0 \\ b_{RQ} &= 2\zeta\omega_0 p_r + \omega_0^2 = \omega_0^2 p_r \tau_{rq0} \\ p_r &= \frac{\omega_0^2}{\omega_0\tau_{rq0} - 2\zeta} \end{aligned} \tag{3.34}$$

Having 4 variables (ω_0, p_r, τ_{rq0}, L_s) and only the three relationships of (3.34), it is necessary to introduce an additional equation to derive the tuning parameters. A possible criterion is to minimize the machine inductance L_{qt}, given the inductance L_s (from power quality considerations). This solution guarantees a better stability of the virtual machine. In particular, a smaller L_{qt} means a larger transient synchronizing power $k_s = V_0^2/Z_q$, meaning that the machine can provide a larger active power, improving the transient response [2]. The following condition is therefore added:

$$\frac{\partial L_{qt}}{\partial \omega_0} = 0 \tag{3.35}$$

The parameter L_{qt} is directly proportional to a_{RQ}. Therefore, a_{RQ} must be minimized, resulting in:

$$\frac{da_{RQ}}{d\omega_0} = 0 = 2\zeta + \frac{\omega_0\tau_{rq0} - 2\zeta - \omega_0\tau_{rq0}}{(\omega_0\tau_{rq0} - 2\zeta)^2} \tag{3.36}$$

leading to:

$$\omega_0\tau_{rq0} = 2\zeta \pm 1 \tag{3.37}$$

Combining (3.32), (3.34) and (3.37), the following is obtained:

$$L_{qt}^{min} = (2\zeta + 1)^2(L_s + L_g) - L_g \tag{3.38}$$

However, the solution $\omega_0\tau_{rq0} = 2\zeta - 1$ cannot be accepted. In fact, $a_{RQ} > 1$ ($L_{qt} > L_s$ by definition).

From (3.37) and (3.32), τ_{rq0} is also derived:

$$\tau_{rq0} = \sqrt{(2\zeta + 1)^3/b} \tag{3.39}$$

The final tuning values are as follows:

$$\begin{aligned} L_{qt} &= (2\zeta + 1)^2(L_s + L_g) - L_g \\ \tau_{rq0} &= \sqrt{(2\zeta + 1)^3/b} \end{aligned} \tag{3.40}$$

Experimental Validation of the Tuning Procedure

The capability of the tuning procedure to guarantee the desired damping, given the design parameters H, ζ and L_s, has been validated experimentally. First, the same design damping coefficient $\zeta = 0.7$ has been used with a set of inertia constant values $H = 1$, 2, 4, 8 and 12 s. A voltage dip of -2 % with a phase jump of $-2°$ has been applied by a grid emulator to perturb the S-VSC. The resulting virtual speed ω_r is shown in Fig. 3.19. As it can be seen in the figure, the trend of the virtual speed always shows a well damped behavior, in accordance to the design values. The different values of inertia constant H lead to larger or smaller variations of the virtual speed, being the angle perturbation constant, the virtual speed variation is proportional to the inertia of the virtual rotor. Also the natural frequency of the speed oscillation depends on the virtual inertia constant. However, the damping factor is always in accordance with the design value.

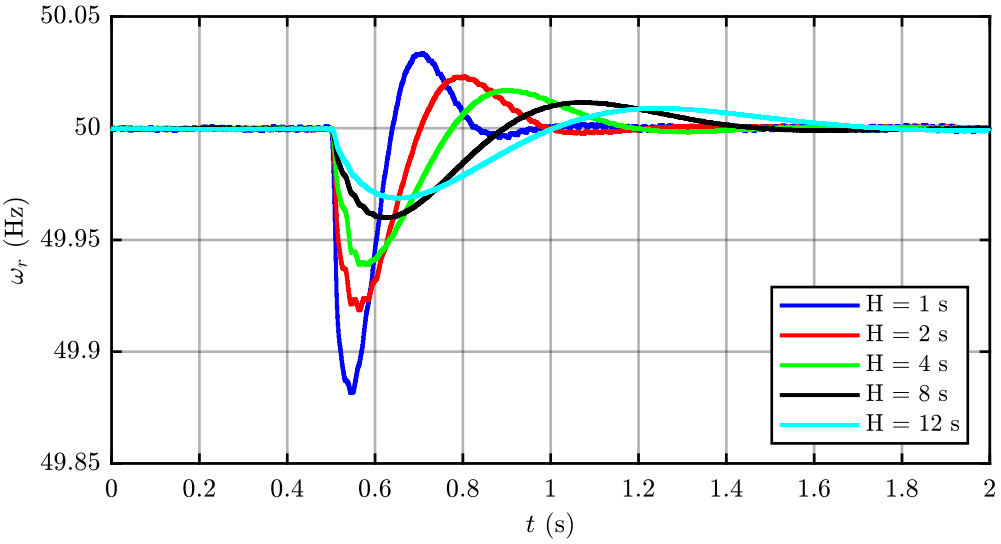

Figure 3.19: S-VSC virtual speed ω_r during a voltage dip $-2\,\%$ with a phase jump of $-2°$. Different values of the inertia constant (H = 1, 2, 4, 8 and 12 s) have been tested to demonstrate the effectiveness of the tuning procedure.

A further experimental test altered the design damping coefficient to $\zeta = 0.4$, keeping the inertia constant at $H = 4$ s. The result, shown in Fig. 3.20 demonstrates that the tuning procedure is capable of guaranteeing the desired damping factor.

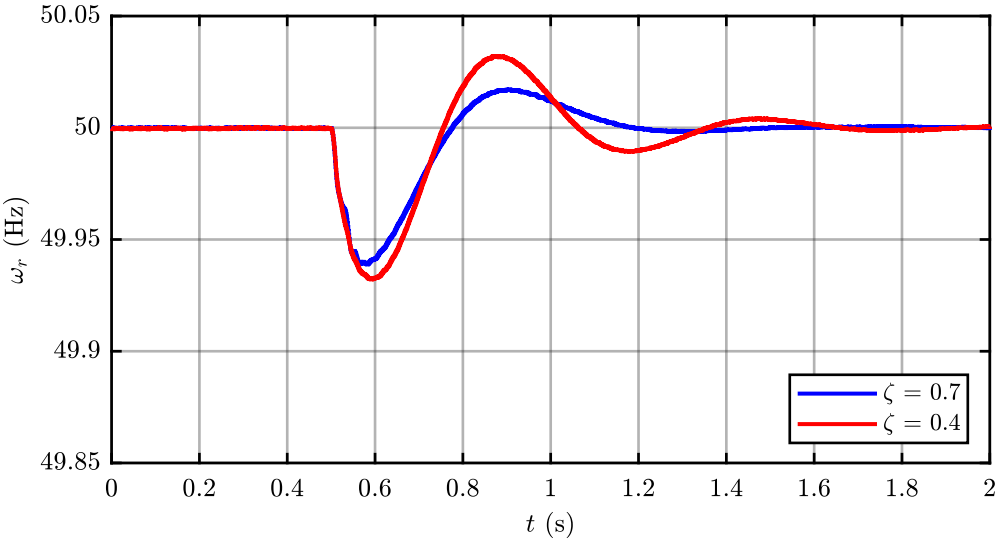

Figure 3.20: S-VSC virtual speed ω_r during a voltage dip $-2\,\%$ with a phase jump of $-2°$. Different damping design values (ζ = 0.4 and 0.7) have been tested to demonstrate the effectiveness of the tuning procedure.

3.3.5 Lead-Lag-Damping

The Lead-lag damping employs a lead-lag filter on the calculated virtual active power feedback P_v of the virtual machine. The block diagram of this solution is depicted in Fig. 3.21. The lead-lag filter $LL(s)$ is defined as:

$$LL(s) = \frac{1 + s\tau_z}{1 + s\tau_p} \tag{3.41}$$

where τ_z and τ_p are the time constant of the zero and the pole of the filter, respectively.

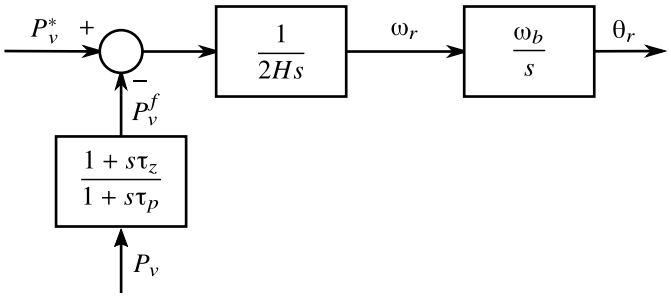

Figure 3.21: Lead-lag damping block diagram.

The benefits of this damping method are the following:

- **No** additional **complexity** of the q-axis (compared to the RQ-based damping);
- **No** embedded **droop** characteristic;
- **Limited sensitivity** to disturbances into the grid (e.g. phase jumps), compared to the PLL-based or PI-based damping;
- **No PLL** is needed.

Tuning Procedure

The two parameters of the proposed lead-lag filter τ_z and τ_p must be tuned in order to ensure the proper damping to the virtual machine. The tuning procedure is similar to the one of the RQ damping of 3.3.4. By applying this damping method to the linearized model of the S-VSC, the following block diagram of Fig. 3.22 is obtained.

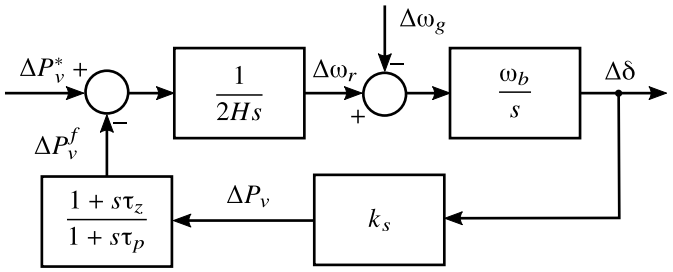

Figure 3.22: Linearized model of the electromechanical behavior of the S-VSC with the lead-lag damping.

The characteristic equation of this linearized system can be derived as follows:

$$1 + \frac{1}{2Hs}\frac{\omega_b}{s}k_s LL(s) = 0 \tag{3.42}$$

Equation (3.42) can be rearranged to obtain the following:

$$s^3 + \frac{1}{\tau_p}s^2 + \frac{\omega_b k_s}{2H}\frac{\tau_z}{\tau_p}s + \frac{\omega_b k_s}{2H}\frac{1}{\tau_p} = 0 \tag{3.43}$$

and the following variable can be defined:

$$a = \frac{\omega_b k_s}{2H} \tag{3.44}$$

The obtained characteristic equation of (3.43) can be generically rewritten as:

$$(s^2 + 2\zeta\omega_0 s + \omega_0^2)(s + p_r) = 0 \tag{3.45}$$

This characteristic equation features two complex poles defined by their damping ζ and natural frequency ω_0 and one real pole $-p_r$.

By comparing (3.43) and (3.45), the following relationships are found:

$$\begin{aligned} 2\zeta\omega_0 + p_r &= \frac{1}{\tau_p} \\ 2\zeta\omega_0 p_r + \omega_0^2 &= ak \\ \frac{a}{\tau_p} &= \omega_0^2 p_r \end{aligned} \tag{3.46}$$

where $k = \tau_z/\tau_p$.

Having 4 variables (ω_0, p_r, k, τ_p) and only the three relationships of (3.46) available, it is necessary to introduce an additional equation to obtain the tuning parameters. A possible solution is to minimize the ratio $k = \tau_z/\tau_p$, which means minimizing the high

frequency gain of the filter. This solution guarantees the least sensitivity from high frequency disturbances affecting the grid. The following condition is therefore added:

$$\frac{\partial k}{\partial \omega_0} = 0 \tag{3.47}$$

where the minimization depends only on ω_0, since the damping coefficient ζ is given as a design input.

From (3.46), it is possible to obtain p_r:

$$\begin{aligned} 2\zeta\omega_0 p_r + \omega_0 &= \omega_0 p_r \tau_p \\ p_r &= \frac{\omega_0}{\omega_0\tau_p - 2\zeta} \end{aligned} \tag{3.48}$$

Then, by substituting (3.48) into (3.46):

$$\begin{aligned} 2\zeta\omega_0 + \frac{\omega_0}{\omega_0\tau_p - 2\zeta} &= \frac{1}{\tau_p} \\ 2\zeta\omega_0\tau_z + \frac{\omega_0\tau_z}{\omega_0\tau_p - 2\zeta} &= \frac{\tau_z}{\tau_p} = k \end{aligned} \tag{3.49}$$

The aforementioned minimization can be now applied to (3.49) as follows:

$$\begin{aligned} \frac{\partial k}{\partial \omega_0} &= 0 \\ 2\zeta\tau_z + \frac{\tau_z\left(\omega_0\tau_p - 2\zeta\right) - \omega_0\tau_z\tau_p}{\left(\omega_0\tau_p - 2\zeta\right)^2} &= 0 \\ 1 - \frac{1}{\left(\omega_0\tau_p - 2\zeta\right)^2} &= 0 \\ \left(\omega_0\tau_p - 2\zeta\right)^2 &= 1 \\ \omega_0\tau_p = 2\zeta \pm 1 & \end{aligned} \tag{3.50}$$

There are, therefore, two solutions for $\omega_0\tau_p$, which can be used to derive p_r from (3.48):

$$\begin{aligned} \omega_0\tau_p &= 2\zeta + 1 \Rightarrow p_r = \omega_0 \\ \omega_0\tau_p &= 2\zeta - 1 \Rightarrow p_r = -\omega_0 \end{aligned} \tag{3.51}$$

It is evident that the second solution ($\omega_0\tau_p = 2\zeta - 1$) is not acceptable, since it would

lead to a real pole in the right half plane. It is therefore obtained that:

$$\begin{aligned} \omega_0^2 &= (2\zeta + 1)\, a \\ p_r &= \omega_0 \\ k &= (2\zeta + 1)^2 \end{aligned} \tag{3.52}$$

The final tuning values are as follows:

$$\begin{aligned} \tau_p &= \sqrt{\frac{2H}{\omega_b k_s \left(2\zeta + 1\right)^3}} \\ \tau_z &= \sqrt{\frac{2H}{\omega_b k_s} \left(2\zeta + 1\right)} \end{aligned} \tag{3.53}$$

Discrete Time Implementation

This damping solution has been implemented digitally after a zero-order-hold discretization of the $LL(s)$ transfer function. The resulting discrete-time expression of the lead-lag filter is as follows:

$$\begin{aligned} x_{LL}^{k+1} &= e^{-T_s/\tau_p} \cdot x_{LL}^k + (1 - e^{-T_s/\tau_p})(1 - \frac{\tau_z}{\tau_p}) \cdot P_v^k \\ P_{v,f}^k &= x_{LL}^k + \frac{\tau_z}{\tau_p} \cdot P_v^k \end{aligned} \tag{3.54}$$

where T_s is the discretization time step, k is the discretization instant and x_{LL} is the internal state variable of the lead-lag filter.

3.3.6 Damping Methods Experimental Validation and Comparison

In this section five damping methods and their tuning have been introduced and analyzed:

1. Droop-based damping;
2. PLL-based damping;
3. PI-based damping;
4. RQ-based damping (proposed);
5. Lead-lag damping (proposed).

In this subsection, these methods will be compared from both a theoretical and an experimental point of view. The comparison will be based on the following criteria:

- **Embedded active droop action**: this quantifies how much active power is injected by the S-VSC when it is operating at non-nominal grid frequency;
- **Sensitivity** of the **virtual rotor speed** ω_r to grid disturbances (such as phase jumps).

The theoretical comparison will be based on the same linearized model, in order to derive the necessary transfer functions. The linearized model is based on the following assumptions, deriving from the classical theory of power system analysis:

1. The virtual resistance of the VSM is neglected (i.e. $R_s = 0$);
2. The virtual flux linkages are assumed to be constant in the first instant of the electromechanical small signal transient. Therefore, $\frac{d\lambda_d}{dt} = \frac{d\lambda_q}{dt} = \frac{d\lambda_e}{dt} = 0$
3. The VSM is operating at no load, i.e. $P_0 = Q_0 = 0$ and so are the virtual currents of the machine;
4. The linearization is performed around the nominal grid frequency $\omega_r = 1$ pu;
5. The behavior of the internal controller is considered to be orders of magnitude faster (kHz) than the electromechanical transients (few Hz) and it is therefore approximated to a unity gain transfer function.

Under these assumptions, the VSM and grid system can be modeled by the following linearized system, shown in Fig. 3.23.

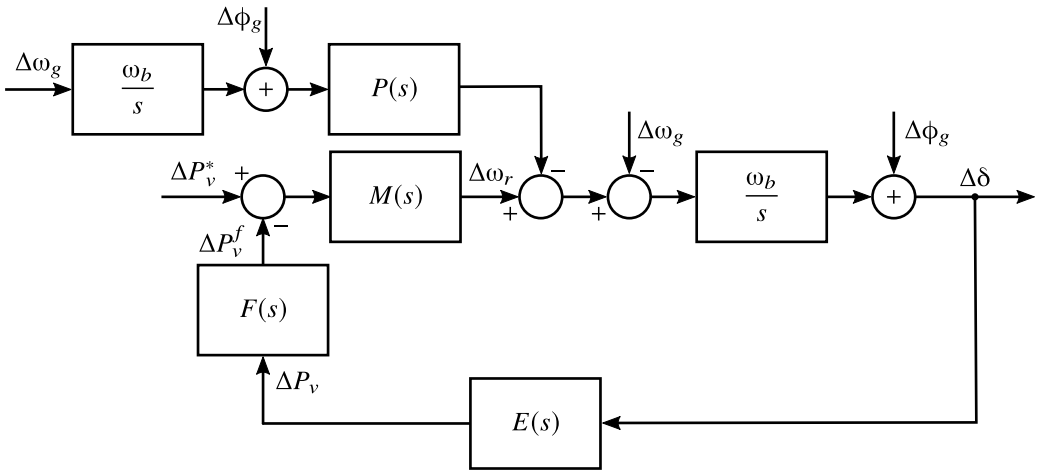

Figure 3.23: Block diagram of the linearized electromechanical model of the S-VSC for damping comparison.

This linearized model is presented in the most general way, in order to be applied to each presented damping method. Therefore, the following blocks are introduced:

- Mechanical block $M(s)$ describing the virtual mechanical emulation of the VSM, relating the active power error and the virtual speed;
- Electrical block $E(s)$ describing the virtual stator of the VSM and its interaction with the grid;
- Grid frequency estimation block effect on the VSM $P(s)$, to include and describe the action of the PLL;
- Filter on the active power measurement $F(s)$.

These blocks assume different value for each damping method. Table 3.1 summarizes the value of each block for each damping method.

Table 3.1: Transfer functions of the linearized model for each damping solution.

Method	**M(s)**	**E(s)**	**F(s)**	**P(s)**
Droop	$\frac{1}{2Hs + D_p}$	k_s	1	0
PLL	$\frac{1}{2Hs + D_{PLL}}$	k_s	1	$-\frac{PLL(s)D_{PLL}}{2Hs + D_{PLL}}$
PI	$k_d + \frac{k_h}{s}$	k_s	1	0
RQ	$\frac{1}{2Hs}$	$\frac{E_0 V_0}{Z_q(s)}$	1	0
LL	$\frac{1}{2Hs}$	k_s	$\frac{1 + s\tau_z}{1 + s\tau_p}$	0

In order to study the effect of the different disturbances that may occur, the following inputs have been introduced:

- Grid frequency variation $\Delta\omega_g$;
- Phase jumps of the grid voltage $\Delta\phi_g$.

Embedded Droop

Starting from the linearized model presented above and applying it to each of the presented damping method, the embedded droop characteristic is studied by calculating the following transfer function:

$$\frac{\Delta P_v}{\Delta\omega_g} = \left(\frac{\omega_b}{s}P(s) + 1\right)\frac{\omega_b E(s)}{s + \omega_b F(s)E(s)M(s)} \tag{3.55}$$

For the various damping methods, substituting the values of Table 3.1:

$$\frac{\Delta P_v}{\Delta \omega_g} = \begin{cases} \dfrac{2Hk_s\omega_b s^2 + D_p k_s \omega_b}{2Hs^2 + D_p s + k_s \omega_b} & \text{Droop-based} \\ \dfrac{\omega_b k_s \left(PLL(s) D_{PLL} - 2Hs - D_{PLL}\right)}{2Hs^2 + D_{PLL} s + k_s \omega_b} & \text{PLL-based} \\ \dfrac{2HE_0V_0\omega_b s}{2HZ_q s^2 + E_0 V_0 \omega_b} & \text{RQ-based} \\ \dfrac{k_s \omega_b s}{s^2 + \left(k_d s + k_h\right)\omega_b k_s} & \text{PI-based} \\ \dfrac{2H\omega_b k_s \left(1 + s\tau_p\right) s}{2H\left(1 + s\tau_p\right) s^2 + \omega_b k_s \left(1 + s\tau_z\right)} & \text{LL-damping} \end{cases} \tag{3.56}$$

which are plotted in Fig. 3.24. For the plot, an example VSM has been used, with the following parameters: $\omega_b = 100\pi$ rad s^{-1}; $H = 4$ s; $\zeta = 0.7$; $k_s = 5$ pu; $L_s = L_g = 0.1$ pu; PLL bandwidth set to 10 Hz.

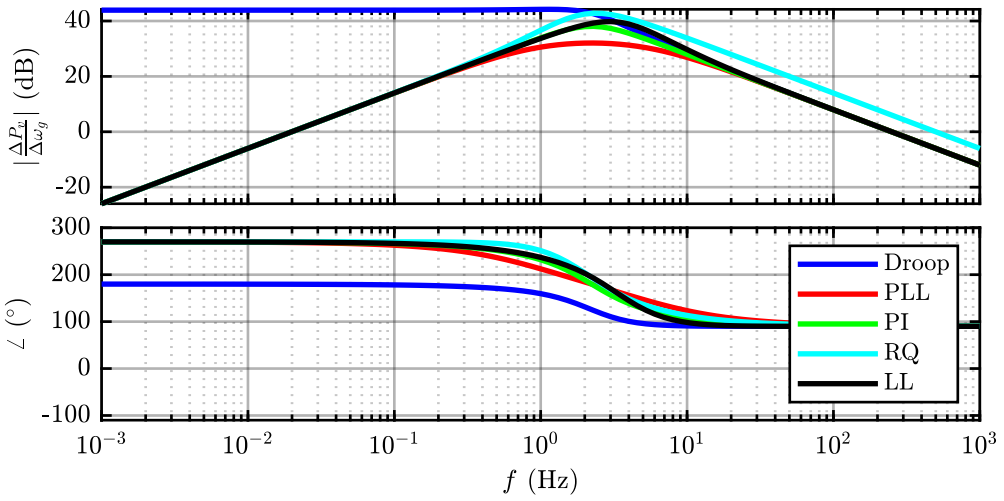

Figure 3.24: Transfer function of the embedded droop characteristic of the S-VSC with the RQ-based damping.

It can be easily calculated, and seen graphically in Fig. 3.24, the active power injected by each damping method when the grid is operating at non-nominal frequency at steady

state ($s \to 0$):

$$\left.\frac{\Delta P_v}{\Delta \omega_g}\right|_{s\to 0} = \begin{cases} D_p & \text{Droop-based} \\ \\ 0 & \text{Other solutions} \end{cases} \tag{3.57}$$

Therefore, the droop-based damping will inject active power into the grid when the grid frequency is different from its nominal value (e.g. frequency after a fault, before the action of primary and secondary frequency control). The amount of injected active power depends on the value of the damping coefficient D_p. This would not represent an issue, if the damping coefficient D_p were equal or similar to traditional active droop coefficients (around 2 % to 5 % [2]). Following the tuning procedure for the example VSM, presented in 3.3.1, D_p = 157 pu. This value is around ten times larger that the usual droop coefficients (5–20 pu). Therefore, an the active power injected is around ten times larger than the one expected by the primary regulation of the frequency.

This is not the case with the other methods, as their low frequency gain is 0. Therefore, if the grid frequency is different from its nominal value, they will not inject any active power into the grid. If a primary frequency regulation logic is needed, an external droop controller can be added. This droop controller can be freely tuned, according to the usual droop coefficients.

This analysis was validated experimentally. The loss of a major generation unit, leading to a significant active power unbalance, was emulated by a grid emulator and the grid frequency was varied according to the profile shown in Fig. 3.25. The values of the frequency nadir (49.2 Hz), the maximum frequency derivative (270 mHz/s) and the frequency after fault (49.75 Hz) were chosen to magnify as much as possible the differences between the five damping methods. For each damping method it has been added an active droop control (droop coefficient set to R = 5%) to shown how much active power would be injected by a canonical droop control strategy. Finally, the inverter maximum current limit was set to 0.6 pu., in order to limit the excessive active power injection in case of droop-based damping. In Fig. 3.26 the active power injected by the inverter for each presented damping method is reported. As predicted, the droop-based damping tries to inject a very large active power, since its equivalent droop coefficient is much larger than usual droop coefficients. The current limitation is soon reached and even after the fault, this damping method still injects a too large power into the grid. On the other hand, the other damping methods show similar results and active power injection. They inject inertial power and active droop power during all the fault. However, in this case, the droop power injection is limited and complies with the design droop coefficient (e.g., after the fault an active power $P_i = \Delta f / R_D / f_n = 0.25/0.05/50 = 0.1$ pu).

In conclusion, the droop-based damping is much inferior compared to the other damping methods, as it injects a too large active power when the grid frequency is far from its rated value. The other damping methods are equivalent under this aspect.

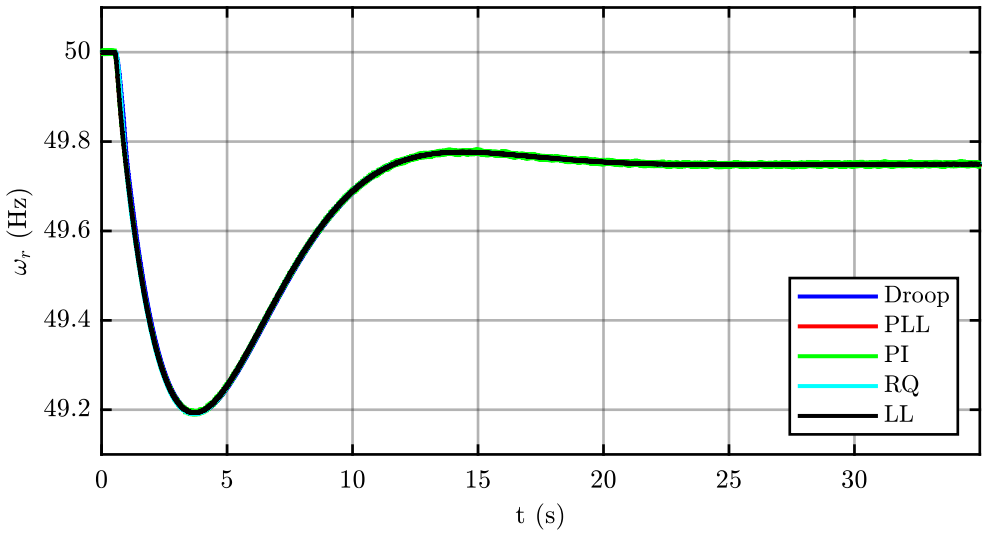

Figure 3.25: Frequency of the S-VSC during the emulated grid fault.

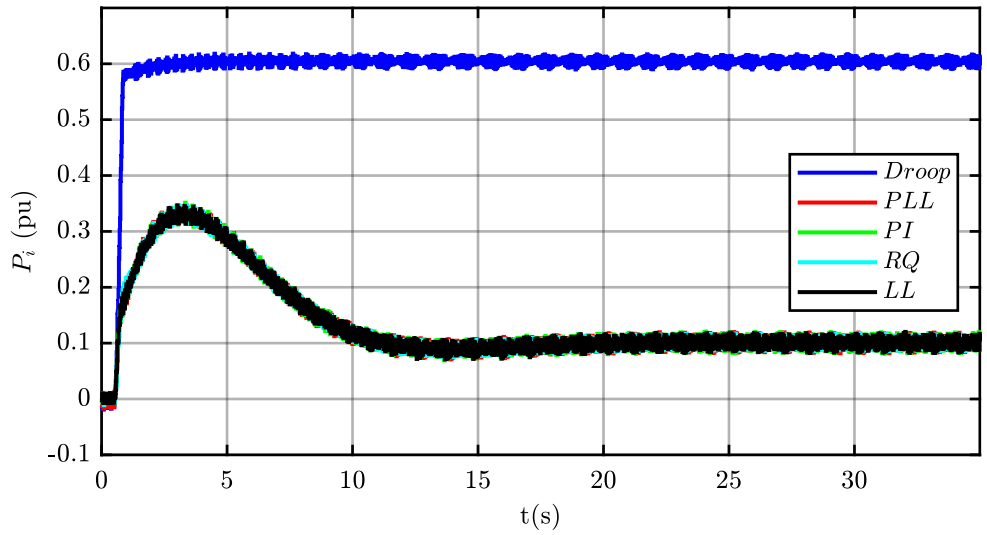

Figure 3.26: Active power injected by the S-VSC with the five presented damping methods during the emulated grid fault.

Sensitivity to Grid Disturbances

Starting again from the linearized model of Fig. 3.23, the sensitivity of the virtual rotor speed ω_r to phase jumps of the grid voltage vectors during faults can be studied

with the following transfer function:

$$\frac{\Delta\omega_r}{\Delta\phi_g} = -\frac{P(s) + F(s)E(s)M(s)}{s + \omega_b F(s)E(s)M(s)}s \tag{3.58}$$

For the various damping methods, substituting the values of Table 3.1:

$$\frac{\Delta\omega_r}{\Delta\phi_g} = \begin{cases} -\dfrac{k_s s}{2Hs^2 + D_p s + k_s\omega_b} & \text{Droop-based} \\ \dfrac{PLL(s)D_{PLL} - k_s}{2Hs^2 + D_{PLL}s + k_s\omega_b}s & \text{PLL-based} \\ -\dfrac{E_0V_0 s}{2HZ_q s^2 + E_0V_0\omega_b} & \text{RQ-based} \\ -\dfrac{k_s\left(k_d s + k_h\right)s}{s^2 + \left(k_d s + k_h\right)\omega_b k_s} & \text{PI-based} \\ -\dfrac{k_s\left(1 + s\tau_z\right)s}{2H\left(1 + s\tau_p\right)s^2 + \omega_b k_s\left(1 + s\tau_z\right)} & \text{LL-damping} \end{cases} \tag{3.59}$$

which are plotted in Fig. 3.27.

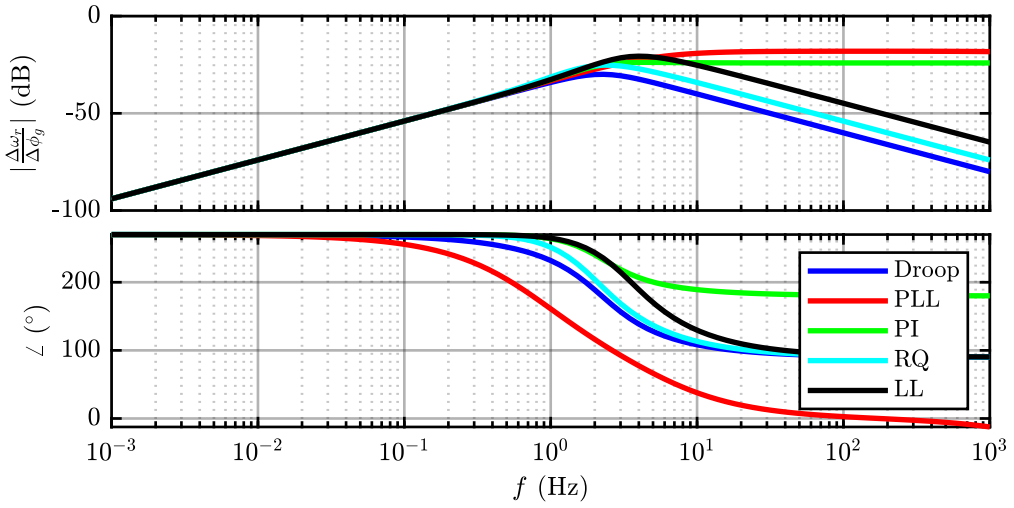

Figure 3.27: Transfer functions of the sensitivity of the presented damping methods to phase jumps $\Delta\phi_g$ of the grid voltage vector.

It is evident from Fig. 3.27 that both the PLL-based and the PI-based damping methods are more sensitive to phase jumps of the grid voltage vector. On the other hand, the other three damping methods (Droop-based, RQ and lead-lag) are more immune to

such disturbances. Therefore, when using these three damping methods the virtual speed ω_r represents a more valid estimation of the actual grid frequency and can be used for monitoring and protection functions.

The different sensitivity to the variation of the grid voltage has been experimentally validated by emulating a permanent grid voltage dip with phase jump (−2 % and −2°). The magnitude of the perturbation was chosen in order to avoid the current limitation of the converter during this test. The outcome of this test for the described damping methods is shown in Fig. 3.28.

The droop-based damping and the RQ-damping show the best performance. In both cases the virtual rotor speed is well damped and features a small variation during the dip. On the other hand, the other three methods (PLL-based, PI-based and LL-based) are more sensitive to the perturbation. In particular, the PI-based shows the largest speed variation (−150 mHz) and the largest steady-state high frequency oscillations, caused by the current and voltage measurements. This large variation in the first instants of the perturbation is due to the direct feed-through (related to the proportional term k_d) from the active power feedback to the virtual speed ω_r. Better results, with lower sensitivity, are obtained with the PLL-based and LL-based damping. These two methods are a compromise between the PI-based and the Droop and RQ-based methods.

In summary, from the point of view of sensitivity to grid disturbances, it can be said that the droop-based and RQ-based damping methods are superior, being very immune to disturbances both in transient and steady-state.

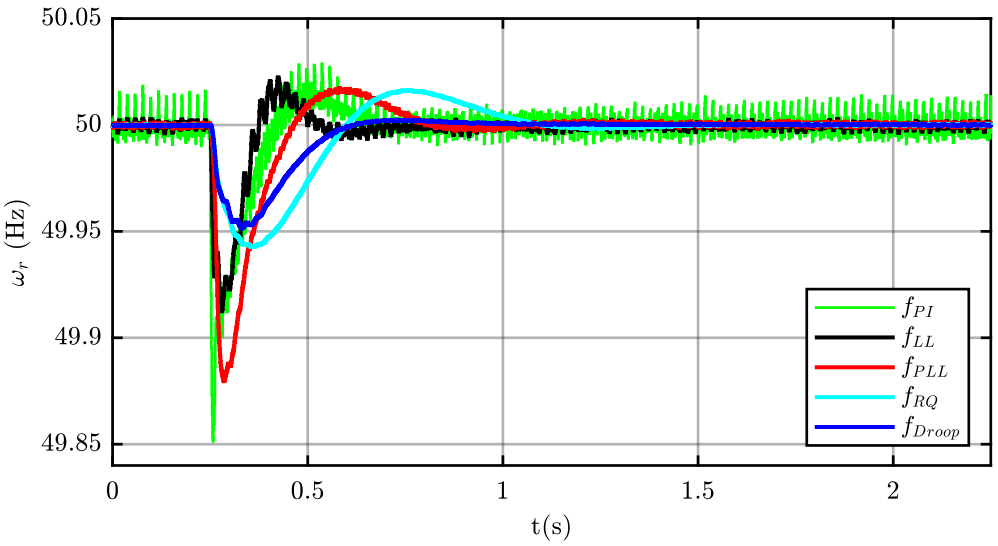

Figure 3.28: Experimental comparison of virtual speed sensitivity to grid voltage disturbances for the five analyzed damping methods. The applied disturbance is a voltage dip with phase jump (−2 % and −2°).

Comparison Summary

This section presents the results from the comparison of five damping methods for the S-VSC. These damping methods feature different structures and levels of complexity, but it is possible to introduce general comparison metrics, thanks to the linearized model of Fig. 3.23. The experimental comparison highlighted that the droop-based damping is strongly unsuitable for field operation, as it injects a too large active power under not rated frequency operation. Among the other models, the best compromise is represented by the RQ-damping method, as it involves a slightly more complex implementation, but guarantees both full decoupling between the damping of the S-VSC and the active droop action of the plant and also high rejection of any non-ideality of the measurements or faulty conditions in the grid. A summary of the presented damping strategies in available in Table 3.2.

Table 3.2: SUMMARY OF THE PROPOSED DAMPING METHODS FOR THE S-VSC.

Feature	**Droop**	**PLL**	**PI**	**RQ**	**L-L**
Parameters	D_p	D_{PLL}	L_{rq}, τ_{rq0}	k_p^{PI},k_i^{PI}	τ_z, τ_p
Implementation	Very easy	Complex	Easy	Complex	Average
Embedded Droop	Yes	No	No	No	No
HF Rejection	Best	Bad	Bad	Best	Average

3.4 Reactive Control Design and Tuning

As it is shown in Fig. 3.29, the implemented excitation control is of integral type, similarly as in [32]. As already mentioned, the reactive power references of the S-VSC are set to zero ($Q_v^* = 0$), being the external active and reactive power setpoints directly fed to the converter. The reactive controller is therefore controlling the virtual reactive power of the S-VSC to 0 at steady state. In addition, in order to avoid any adverse interaction of the inverter current control and the excitation control of the S-VSC, a feed-forward term λ_{ff} is added. This term depends on the external reactive power setpoint of the converter and on the grid inductance L_g, which is estimated in the control by the parameter $\tilde{L}_g$.

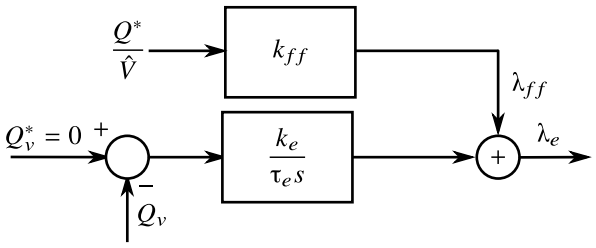

Figure 3.29: Excitation control block of the S-VSC.

In order to study the proposed excitation control, a simplified linearized model is derived, based on the following assumptions:

1. A connection to the medium or high voltage network is considered. Therefore, the connection to the grid is considered mainly inductive. The grid resistance R_g is therefore neglected;
2. The virtual stator resistances are neglected: $R_s \approx 0$;
3. The virtual rotor speed is assumed constant $\omega_r \approx \omega_0$ for the small signal analysis and the linearization is performed around $\omega_0 = 1$ pu;
4. The derivatives of the flux linkages of the virtual machine are negligible $\frac{d\lambda}{dt} \approx 0$;
5. The inner current controller is considered ideal, and therefore the actual inverter current is always equal to its reference;

Based on these assumptions, the virtual stator and grid electrical equation can be derived as follows:

$$j\omega_r \lambda_{dq} = e_g^{dq} + L_g i_v^{dq} \tag{3.60}$$

Being the excitation control implemented on the machine d-axis, only the d-axis component of (3.60) is considered:

$$\omega_r \lambda_d = e_{gq} + L_g i_{vd} \tag{3.61}$$

Therefore, the virtual stator of the S-VSC can be modeled as a Thèvenin equivalent circuit, composed of a voltage source (excitation) and a virtual stator inductance L_s. The virtual stator flux λ_d can be expressed as:

$$\lambda_d = \lambda_e - L_s i_{vd} \tag{3.62}$$

By combining (3.61) and (3.62), at constant speed $\omega_r = \omega_0$, the equivalent circuit of Fig. 3.30 is obtained.

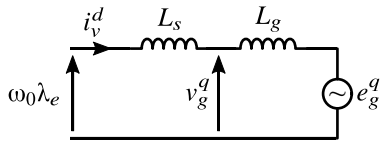

Figure 3.30: Equivalent d-axis circuit of the S-VSC for the study of the excitation control.

The reactive power transfer can also be linearized, assuming the voltage aligned to the q-axis and a zero-power operating point ($Q_0 = 0$). The reactive power variation ΔQ_v is as follows:

$$\Delta Q_v = V_{q0} \Delta i_d \tag{3.63}$$

Therefore, the d-axis current i_d represents the reactive component of the converter current. These results will be used in the next subsection to obtain a tuning procedure for the excitation control.

3.4.1 Reactive Control Tuning

From the equivalent circuit of Fig. 3.30 and the reactive control structure of Fig. 3.29, the block diagram of Fig. 3.31 is obtained.

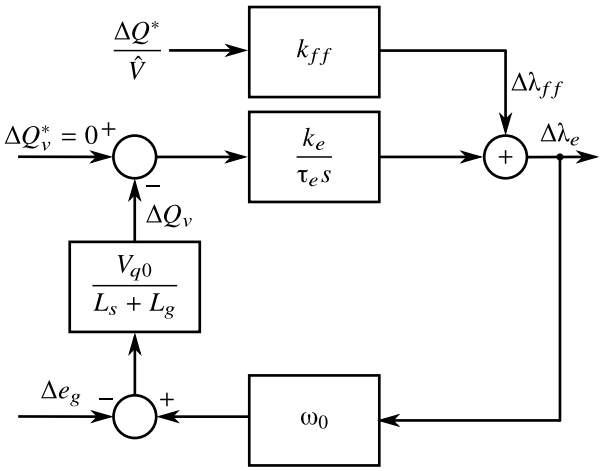

Figure 3.31: Linearized model of the S-VSC excitation control.

The characteristic equation of the linearized system of Fig. 3.31 is:

$$s\tau_e(L_s + L_g) + \omega_0 k_e V_{q0} = 0 \tag{3.64}$$

This system is governed by a single pole with a time constant τ:

$$\tau = \frac{\tau_e(L_s + L_g)}{\omega_0 k_e V_{q0}} \tag{3.65}$$

This time constant is then tuned by the user to the design value $\tau = \tau_e$. Therefore, the resulting gain of the excitation control is:

$$k_e = \frac{L_s + L_g}{\omega_0 V_{q0}} \tag{3.66}$$

The gain k_e guarantees reactive support with the desired tunable time constant τ_e. As the actual grid inductance L_g is not known, its estimated value $\tilde{L}_g$ must be used:

$$k_e = \frac{L_s + \tilde{L}_g}{\omega_0 V_{q0}} \tag{3.67}$$

It is evident that the actual time constant τ_e depends on the correct estimation $\tilde{L}_g$ of the grid reactance L_g. Therefore, online estimation techniques of the Short Circuit Ratio (SCR) of the grid could be employed [89–93] to update the excitation control gain. In

general, in most high-power applications, the grid impedance is however a known value, as it depends on the point of connection to the grid (e.g. Medium voltage connection through a known transformer) and can therefore be set as a constant.

The error on the actual time constant ϵ_τ will therefore depend only on the accuracy of the grid impedance estimation $\epsilon_{\tilde{L}_g}$, since the virtual stator impedance L_s of the machine is set by the user. In fact:

$$\epsilon_\tau = \frac{\tau - \tau_e}{\tau_e} = \frac{\dfrac{\tau_e(L_s + L_g)}{\omega_0 k_e} - \tau_e}{\tau_e} = \frac{L_s + L_g}{L_s + L_g(1 + \epsilon_{\tilde{L}_g})} \tag{3.68}$$

As depicted in Fig. 3.32, the error on the time constant is almost linear around the ideal estimation point $\epsilon_{\tilde{L}_g} = 0$. However, the estimation error has a larger influence as the SCR decreases, therefore particular attention must be taken in case of ultra-weak grids.

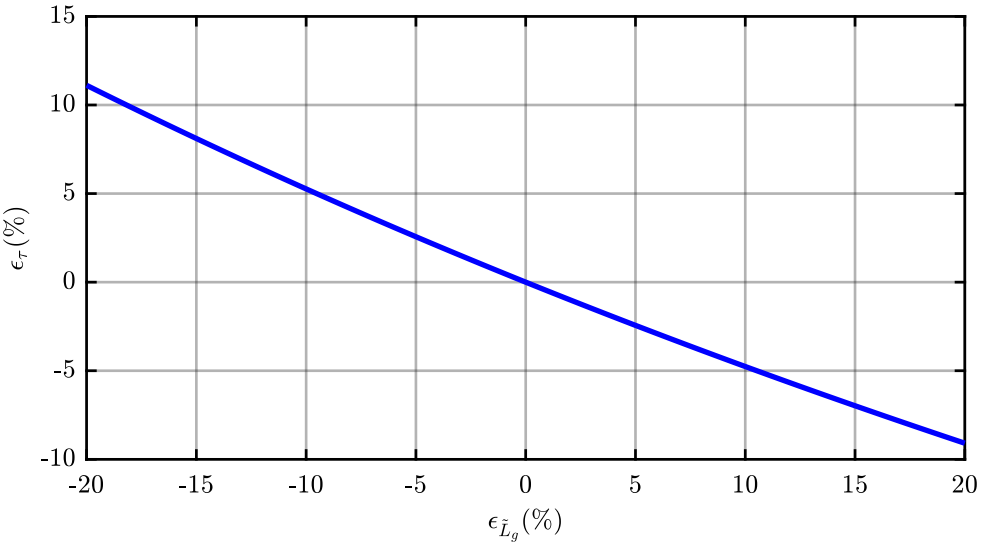

Figure 3.32: Error on the actual time constant ϵ_τ of the VSM, due to the estimation error of the grid impedance $\epsilon_{\tilde{L}_g}$. $L_s = 0.1$ pu, $L_g = 0.1$ pu.

3.4.2 Interaction with the Inverter Reactive Control

The reactive support contribution time constant τ_e of the VSM is tuned according to the desired current injection specifications. On the other hand, a faster dynamic behavior is expected when the inverter reactive power setpoints are changed by the user (e.g. static voltage regulation). To improve this behavior and to decouple the reactive control of the VSM from the reactive control of the converter, we propose to add a feed-forward term λ_{ff}, proportional to the reactive power setpoint, to the excitation flux linkage λ_e, as shown in Fig. 3.29. This feed-forward imposes the excitation flux linkage to the necessary value

to guarantee the desired steady-state reactive power flow, avoiding an opposite reaction of the VSM. To study the effect and the tuning of this feed-forward action, the diagram of Fig. 3.33 following transfer function must be considered:

$$\left.\frac{\Delta Q}{\Delta Q^*}\right|_{\Delta e_g=0} = \left(k_{ff} + \frac{1}{A_{ff}}\right)\frac{A_{ff}}{1 + A_{ff}L_g} \tag{3.69}$$

where

$$A_{ff} = \frac{\left(L_s + L_g\right)\tau_e s}{\left(L_s + L_g\right)\tau_e s + k_e V_0} \tag{3.70}$$

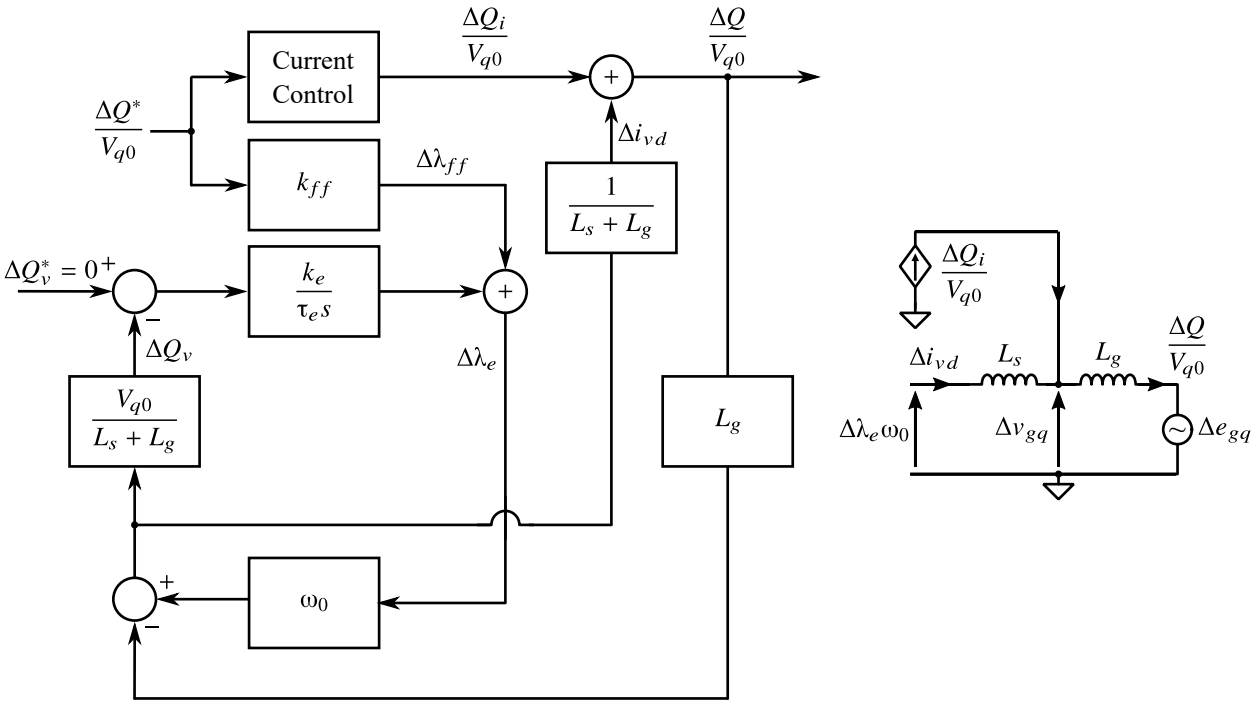

Figure 3.33: Block diagram and equivalent circuit of the proposed feed-forward term in the reactive control of the VSM.

It must be noted that the dynamic behavior of the current controller is approximated as ideal, since its time constant is order of magnitude faster than the excitation control of the VSM.

The optimal feed-forward term k_{ff} is calculated by imposing a unity gain of the reactive controller instantaneous response to a step variation in the reactive power reference:

$$\left.\frac{\Delta Q}{\Delta Q^*}\right|_{s\to\infty} = 1 \tag{3.71}$$

This results in $k_{ff} = L_g$. Therefore, the correct value of the feed-forward term is the estimated grid inductance $\tilde{L}_g$. In Fig. 3.34 the Bode diagram of (3.69) is plotted with

and without feed-forward. It is evident that the action of the proposed feed-forward is effective in increasing the dynamic response of the system. This dynamic is limited only by the performance of the current controller.

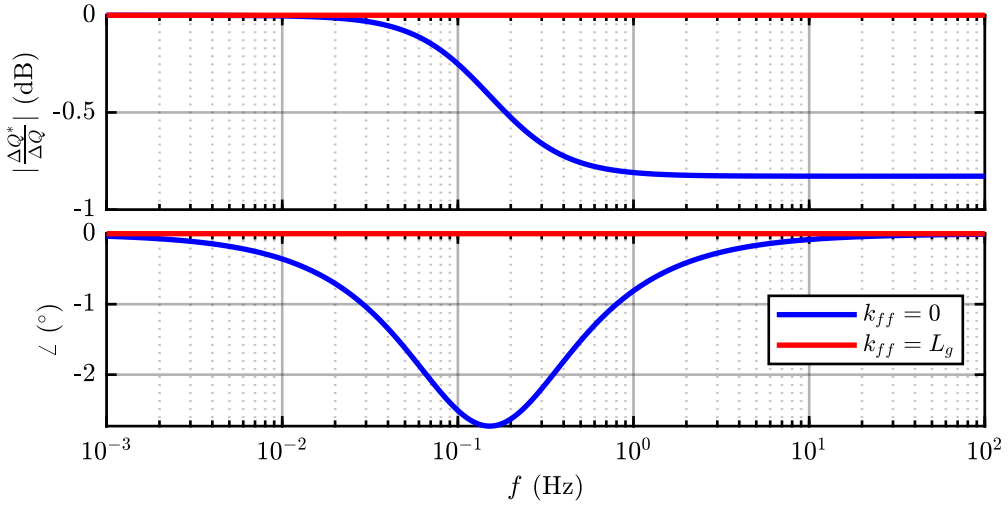

Figure 3.34: Transfer function of the inverter reactive control with and without the proposed feed-forward.

3.4.3 Experimental Validation

The proposed tuning method and feed-forward are experimentally validated in this section. Two perturbations have been applied to the system:

1. Permanent voltage dip (−10 %). This test validates first the tuning procedure of the excitation control. Then, the effect of an incorrect grid inductance estimation on the reactive control is analyzed.

2. Step in the reactive power reference of the inverter. This validates the effectiveness of the proposed feed-forward term and analyses the effects of an incorrect estimation of the grid inductance on the feed-forward term.

In each test, the excitation control time constant has been set to $\tau_e = 1$ s. In the first permanent voltage dip test, the tuning method is validated. As shown in Fig. 3.35a, the virtual excitation flux linkage λ_e reaches the final value of 0.9 with the desired 1 s time constant. The time constant is in fact defined as the time needed to complete 63.2 % of the transient. In the test case, the total transient is 0.1 pu, therefore, the time constant τ is measured as the time between the beginning of the transient and when $\lambda_e = 0.94$ pu. This is highlighted in Fig. 3.35a and actually corresponds to the design value of 1 s. Fig. 3.35b

shows the actual inverter current and grid voltage for the phase a. The positive voltage envelope shows that the during the voltage dip, the S-VSC action contributes to support the grid voltage, which does not change abruptly, but it is supported by the S-VSC reactive current injection. It must be noted that the current is limited arbitrarily to 36 A (0.6 pu), to show the effectiveness of the current limitation strategy and the validity of the proposed tuning method also in case of non-linear effects, such as the current limitation.

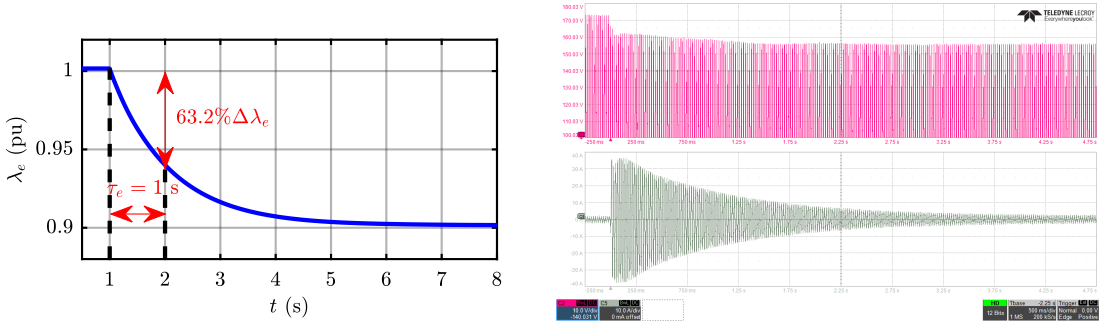

(a) (b)

Figure 3.35: Validation of reactive control tuning: a permanent voltage dip of −10 % has been applied. From left to right:
a) Transient behavior of the virtual excitation flux λ_e. The time constant $\tau_e = 1$ s of the excitation control is highlighted graphically;
b) Scope capture of the positive envelope of the grid phase voltage a across C_f (upper plot, Ch2, 10 V/div) and of the injected grid current, phase a (bottom plot, Ch5, 10 A/div).

The tuning sensitivity to the grid inductance estimation has been tested as well and the results are shown in Fig. 3.36a. Three grid inductance estimation values have been used: $0.8L_g$, L_g and $1.2L_g$ (i.e. ±20%). The perturbation is again a permanent voltage dip of −10 %. As it emerges from the results of this test and the magnification of Fig. 3.36b,there is a small variation on the actual time constant, even when there is a large estimation error. Therefore, the proposed tuning method can be considered valid also when the grid impedance is incorrectly estimated or varies due to faults or reconfigurations.

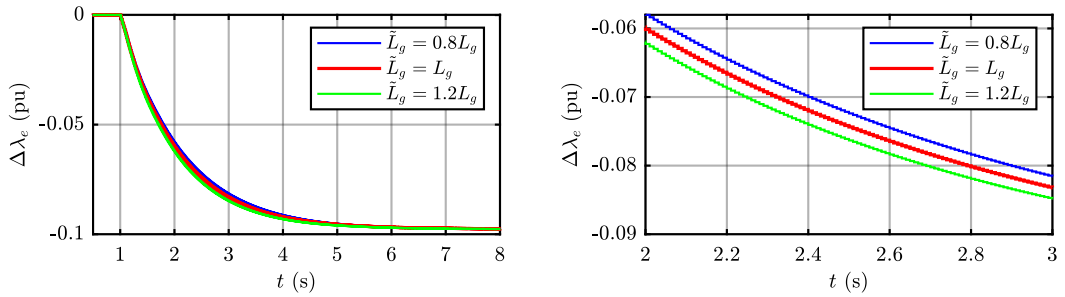

(a) (b)

Figure 3.36: Sensitivity to grid inductance estimation: a permanent voltage dip of −10 % has been applied. The estimated grid impedance $\tilde{L}_g$ varies from $0.8L_g$ to $1.2L_g$. From left to right:
a) Variation of the virtual excitation flux linkage λ_e;
b) Detail of to highlight the differences due to a non ideal estimation $\tilde{L}_g$ of the grid inductance.

Finally, the proposed feed-forward term is validated with a step variation in the reactive power reference Q^*. The results are shown in Fig. 3.37a and Fig. 3.37b. The reactive power trend is compared with and without the proposed feed-forward term $k_{ff} = L_g$. Thanks to the feed-forward term, the excitation flux linkage λ_e instantly reaches its final value and the integral action only corrects the small grid inductance estimation error. This way, the reactive power transient only depends on the current control and it is not influenced by the reactive control time constant τ_e, which can be freely tuned to provide the desired time constant for reactive support during grid voltage variations.

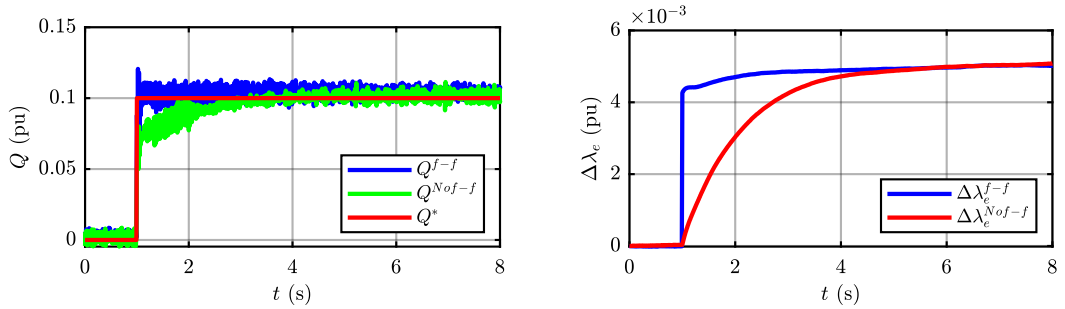

(a) (b)

Figure 3.37: Validation of the feed-forward term: A 0.1 pu step in the reactive power reference Q^* is applied (from 0 to 0.1 pu). From left to right:
a) Reactive power reference Q^* and actual reactive power Q with and without the proposed feed-forward;
b) Virtual excitation flux variation λ_e with and without the optimum feed-forward.

Summary and Conclusions of Reactive Power Control Tuning

In this section it has been explained the structure of the excitation control of the S-VSC. Moreover, the relationship between the tuning of the excitation control of the S-VSC and its virtual stator and grid inductances has been revealed. From this analysis, it emerges that it is important to carefully estimate the grid impedance, in order to obtain the desired design parameters. Moreover, a feed-forward term is proved as an effective solution to increase the dynamic behavior of the reactive current control, decoupling the time constant of the reactive support during voltage dips from the one of the inner current controller when changing the reference of the reactive channel.

As demonstrated both theoretically and experimentally, the proposed tuning procedure and feed-forward term are robust against incorrect grid inductance estimation or its variations due to faults or grid reconfigurations. Moreover, the error in the estimation of the grid impedance are affecting the response only transiently and are compensated by the steady-state integral action of the excitation control.

3.5 Synchronization and Converter Startup

The grid synchronization process of VSMs is a critical aspect, just as the synchronization of real SGs. The advantage of virtual machines is the possibility of having a virtual transient, with no current exchange with the grid. The control must take care of limiting the transient inrush currents and ensure a seamless synchronization process. The startup process of the S-VSC follows the steps:

1. **Start synchronization**: the S-VSC is enabled and the model is executed by the digital controller. The current control is off, as well as the PWM modulation. The power switches (e.g. IGBTs) are open. No current is therefore injected or absorbed from the grid;

2. **Synchronization**: The converter is measuring the grid voltage. The S-VSC is fed the grid voltage and synchronizes to it without the need of a PLL. The duration of the transient depends on the initial load angle between the S-VSC and the grid. As it can be seen in Fig. 3.38a, any initial load angle eventually lead to the synchronization. The synchronization ends when the virtual speed ω_r reaches a steady-state;

3. **Start Control**: the S-VSC is synchronized and perfectly tracks the grid frequency and phase angle. The PWM modulation and the current control can now be enabled. As Fig. 3.38b shows, the PWM is enabled at $t = 0.1$ s after the synchronization is completed. The currents are controlled to be 0 A after startup. The converter is now fully operating. The power references can be modified and the plant is in fully operational state.

The startup process is therefore performed in the time span of few seconds, depending on the initial load angle of the S-VSC. The large virtual speed variations of the S-VSC (more than 5 Hz) during the synchronization process are not an issue, since this phase is performed within the digital control, with no current exchange with the grid. Since the S-VSC operates at no load during the synchronization process, there is no stability boundary on the initial load angle.

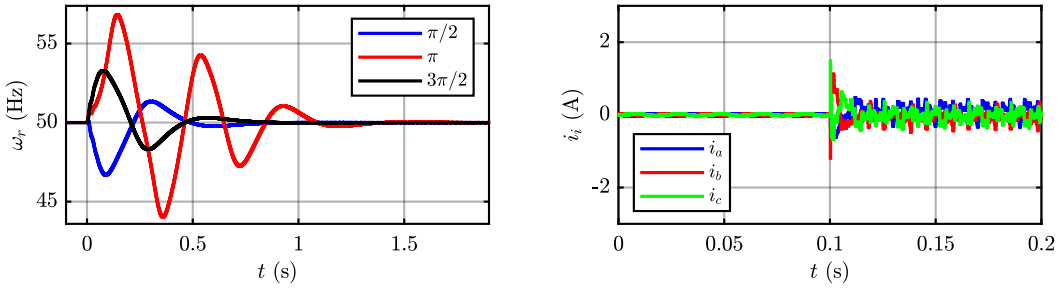

(a) (b)

Figure 3.38: S-VSC synchronization process. From left to right:
a) S-VSC synchronization transient with different initial load angles ($\pi/2, \pi, 3\pi/2$);
b) Startup transient. PWM and current control are enabled at t = 0.1 s after the synchronization is completed.

3.6 Current Controller

The current control (Current Control and Reference Limitation blocks in Fig.3.39) can be performed using any of the available strategies presented in literature [5, 94]. In this thesis a PI controller in the S-VSC rotating frame + Resonant controller on the sixth harmonic has been implemented.

For any employed controller, the same current limitation strategy is used, as discussed in the following section.

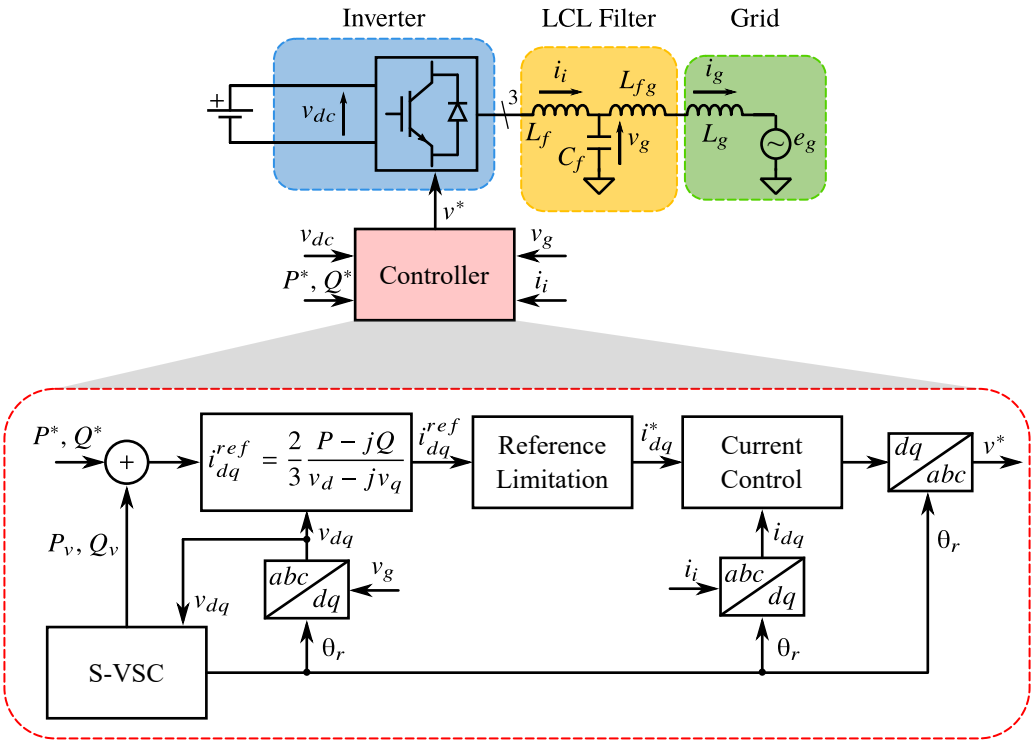

Figure 3.39: S-VSC control of a current-controlled inverter.

3.6.1 Current Limitation Strategy

Differently from SGs, industrial power converters cannot be overloaded, even for short times. Therefore, the current references generated by the S-VSC must be limited to comply with the rating of the converter. In this thesis, the amplitude of the reference current vector i_{dq}^{ref} (sum of the external setpoints and the S-VSC currents) is limited in its amplitude $|i_{ref}|$, without modifying its angle $\angle i_{ref}$ in the (d,q) plane. Therefore, the ratio between the active and reactive component of the current is not modified. The output i_{dq}^* is then fed to the current controller. This saturation algorithm is visually depicted in Fig 3.40.

This saturation algorithm works well if the references are sinusoidal at the S-VSC frequency ω_r. If harmonics or negative sequence components are present in the current references i_{dq}^{ref}, then, this saturation strategy will introduce a distortion in their shape. However, this is not usually an issue, as these contributions are limited in amplitude (few percent of the nominal current).

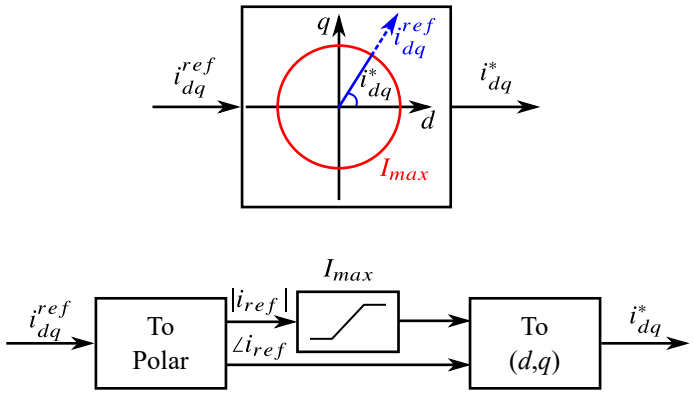

Figure 3.40: Current limitation strategy block diagram.

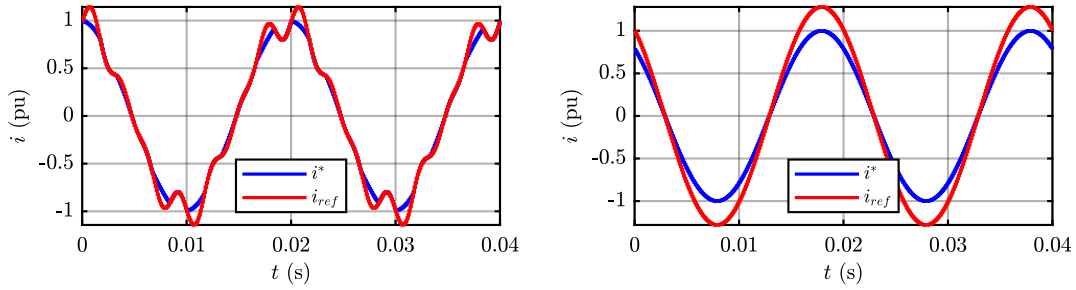

(a) (b)

Figure 3.41: S-VSC current limitation strategy. Maximum amplitude has been set to 1 pu. Phase *a* reference current with and without limitation. From left to right:
a) Limitation of a non-sinusoidal waveform (i_d^{ref} = 1 pu; i_q^{ref} = 0.1 pu; i_6^{ref} = 0.2 pu);
b) Limitation of a sinusoidal waveform (i_d^{ref} = 1 pu; i_q^{ref} = 0.8 pu).

3.6.2 PI+RES in (*d*,*q*)

As mentioned before, a PI+RES (tuned to the sixth harmonic) controller in the S-VSC (*d*,*q*) rotating frame as in [95] has been implemented. The relative block diagram is depicted in Fig 3.42. The tuning of the controller (i.e. the proportional and integral gains k_p and k_i) given the control bandwidth f_{BW}^i and the zero of the regulator ω_{zi} are performed as follows:

$$\begin{aligned} k_p &= 2\pi f_{BW}^i L_f \\ k_i &= \omega_{zi} k_p \end{aligned} \tag{3.72}$$

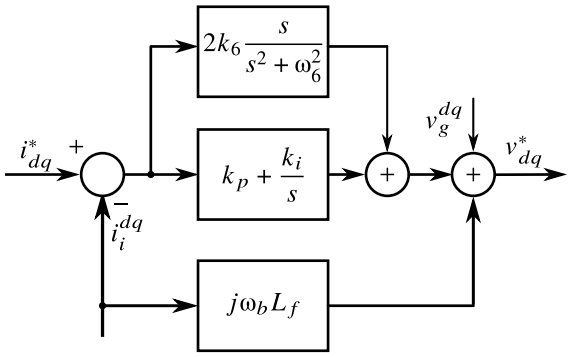

Figure 3.42: Implemented current control in the S-VSC (d,q) frame with a PI and a resonant controller on the sixth harmonic.

The additional resonant term on the sixth harmonic is necessary to track the harmonic compensation references. Supplementary resonant controllers can be added for higher order harmonics (e.g. on the twelfth harmonic to control the fifth and seventh harmonics). In this thesis simply a resonant controller on the sixth harmonic, as in [95], was implemented. The tuning values of the bandwidth f^i_{BW} and the zero of the current controller ω_{zi} are available in 4.1.

3.6.3 Conclusions and Summary of the S-VSC Model

In this chapter, the S-VSC model and its integration into the control of an inverter has been proposed and analyzed. The proposed approach only acts as a parallel compensator add-on and it generates the active and reactive power references for the inverter to provide the ancillary services, mentioned in section 1.1, to the grid. These services include virtual inertia, reactive power support and current harmonic compensation, while a traditional current controlled inverter is in charge of injecting the desired active and reactive power into the grid. This way, the S-VSC always operates at a small load angle. **Therefore, it presents very good performance in terms of transient stability and damping. Thanks to the virtual stator model, also voltage harmonics compensation is achieved.**

Three electromechanical damping strategies available have been presented and compared with the two proposed damping strategies (RQ-based and Lead-Lag-damping). **The proposed damping strategies globally outperform the ones available in the literature and especially the RQ-based damping is a good compromise of implementation complexity and transient performance.**

Chapter 4

S-VSC Ancillary Services Provision Experimental Validation

In this chapter, the ancillary services capabilities of the S-VSC model has been validated experimentally. The following set of tests has been performed to study its behavior for each required ancillary service:

- Active and reactive power setpoint variation: operation under normal conditions;
- Inertial behavior tests: response to grid frequency variations;
- Voltage dips and swells: injection/absorption of reactive current during faults;
- Harmonic compensation.

A dedicated subsection will be devoted to each aspect.

The content of this chapter has been partially published in [82–85].

4.1 Description of the Experimental Setup

The S-VSC model, described in Chapter 3, has been implemented on a three-phase two-level 15 kVA grid-connected inverter for experimental validation. Fig. 4.1 shows a picture of the experimental setup. The rated dc side voltage is 400 V and it is provided by an external bidirectional power supply. The grid side is represented by a 50 kVA grid emulator providing a 220 Vrms line-line grid voltage at 50 Hz. The control algorithm is implemented in C code on a dSPACE 1005 platform. Both the inverter switching frequency and the controller sampling frequency are both 10 kHz. The LCL filter parameters and the S-VSC parameters are listed in Table 4.1.

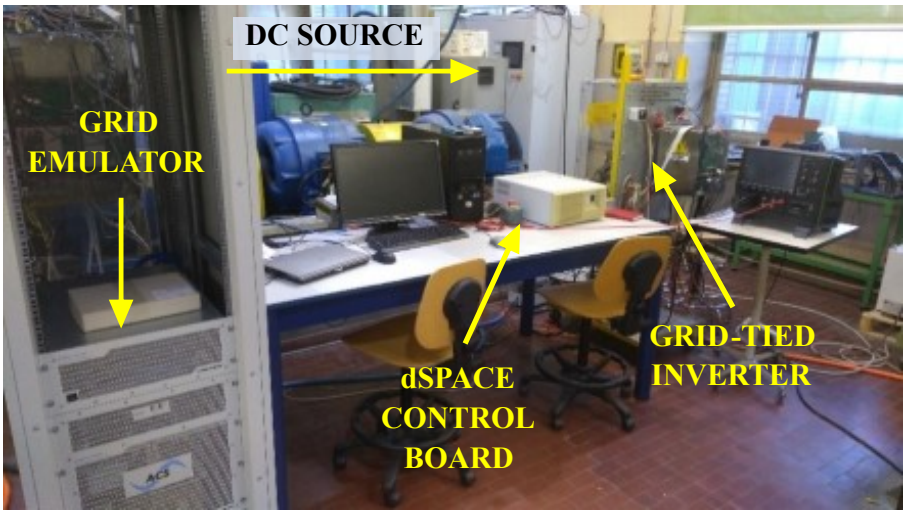

Figure 4.1: Picture of the experimental setup used for the S-VSC validation.

Table 4.1: Inverter and S-VSC parameters for the experimental tests (unless explicitly mentioned otherwise).

Parameter	Value	Parameter	Value
V_b	$120\sqrt{2}$ V	S_b	15 kVA
L_f	545 µH	C_f	22 µF
L_{fg}	120 µH	L_g	270 µH
f_{BW}^i	500 Hz	ω_{zi}	314.15 rad/s
k_p	1.712 V/A	k_i	537.9 V/(As)
L_s	0.1 pu	R_s	0.02 pu
H	4 s	τ_e	0.1 s
L_{rq}	0.71 pu	τ_{rq0}	0.23 s

4.2 Power Reference Variations

The first experimental tests validates the S-VSC capability of injecting power into the grid. The advantage of the parallel operation of the S-VSC introduced in chapter 3 is proved by defining two operating modes: VSC and VSG. The difference between these two operating modes lies in where the external power references P^* and Q^* are fed. Such references can be either provided directly to the inverter control loops (as proposed for the S-VSC) or given as references to the S-VSC.

The proposed operating mode is the VSC. In this operating mode, the power references are processed directly by the inverter control loops and the virtual machine is only in

charge of generating compensation references to provide grid ancillary services (virtual inertia, reactive support, harmonic compensation).

The second operating mode, introduced for comparison, is the VSG, meaning that the VSM fully operates as a real synchronous generator, dealing with both the active and reactive power references. In this operating mode, the inverter current control loops simply track the references generated by the VSM. The definition of this second operating mode is useful, in order to compare the proposed S-VSC solution with other existing models in the technical literature, which can be classified as VSGs.

In these tests, no low-pass filter was applied to the calculated powers, therefore a substantial power ripple is visible. This power ripple is due to the measurement of the currents and the grid voltages. In fact, being the power the product of current and voltage, the measurement noise is amplified. Moreover, the measurement circuit has been used far from its full range, being the power steps at few tens percent of the nominal power rating.

First, the same step in the active power references (0.1 pu to 0.2 pu) has been applied for each operating mode. The results are compared in Fig. 4.2. This test compares both the VSM virtual speed ω_r variation and the step response of the active power, when a step in its reference is given (0.1 to 0.2 pu). It must be noted that in the VSG mode (references fed to the VSM) the virtual machine has to accelerate, in order to change its load angle δ and transfer the required active power to the grid. A larger speed deviation Δf can be noted in Fig. 4.2a. This has two detrimental effects. The first effect is that it slows down the dynamic power response of the inverter, as it can be seen in Fig. 4.2a, as the virtual rotor must change its relative position to the grid angle. The second aspect is that the machine stability is lowered, as the working point of the virtual machine moves to a less stable position (closer to $\delta = 90°$). On the other hand, in VSC mode, the virtual machine does not change its load angle, but only slightly reacts to the perturbation, without interfering with the active power step variation. This leads to a faster dynamic behavior, as shown in Fig. 4.2a, which only depends on the dynamic of the current controller, a smaller overshoot and a more damped response. Moreover, this also leads to benefits when the virtual rotor is employed to estimate the grid frequency, for monitoring purposes and as a feedback for a proportional frequency regulation.

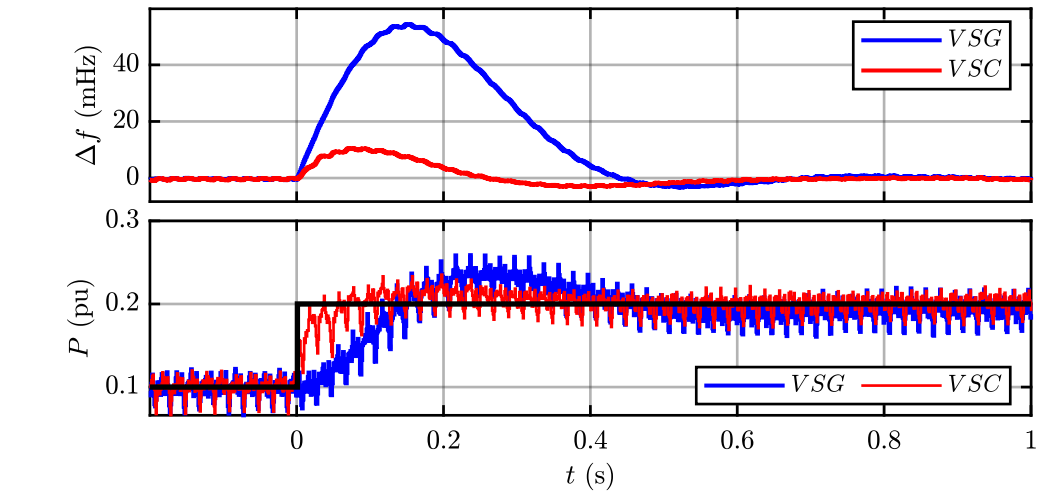

(a)

(b)

(c)

Figure 4.2: Active power reference P^* step (from 0.1 pu to 0.2 pu). Comparison of VSC operating mode versus VSG mode.
a) Frequency variation of the VSM (mHz) and active power injected by the inverter (pu);
b) Current waveforms for VSG mode. Ch2, phase voltage at the PCC (50 V / div). Ch5, phase current i_a (10 A / div);
c) Current waveforms for VSC mode. Ch2, phase voltage at the PCC (50 V / div). Ch5, phase current i_a (10 A / div).

Therefore, the VSC mode is superior, guaranteeing the desired active power flow with the fastest dynamics, higher damping ratio and the smallest virtual speed variation, being therefore able to decouple the active power control of the plant from the internal dynamic of the VSM.

A similar test has been performed for the reactive power reference Q^*. The results are available in Fig. 4.3. As in Test 3, also in this case the VSC mode is superior, guaranteeing a faster dynamic behavior, since the dynamic response does not depend on the machine parameters, but only on the design of the current control loop.

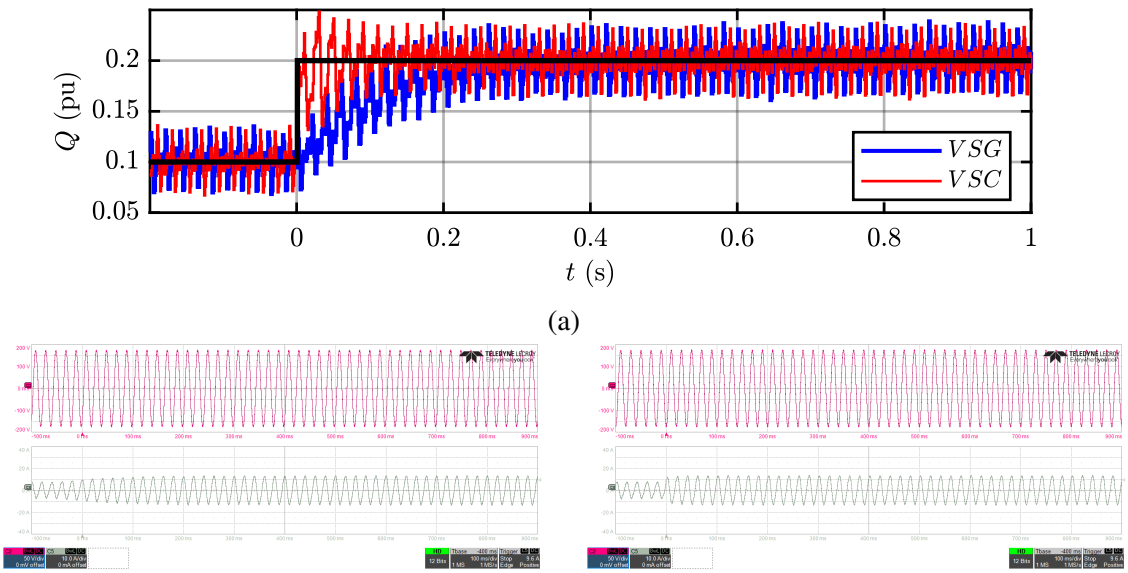

(a)

(b)

(c)

Figure 4.3: Reactive power reference Q^* step (from 0.1 pu to 0.2 pu). Comparison of VSC operating mode versus VSG mode.
a) Reactive power transient;
b) Current waveforms for VSG mode. Ch2, phase voltage at the PCC (50 V / div). Ch5, phase current i_a (10 A / div);
c) Current waveforms for VSC mode. Ch2, phase voltage at the PCC (50 V / div). Ch5, phase current i_a (10 A / div).

The final power reference variation test involved a simultaneous active and reactive power reference step (0.1 to 0.2 pu). This test has been performed in VSC mode. As per Fig. 4.4, little difference can be seen from the previous individual active or reactive power step variations, proving that the two active and reactive power channels are well decoupled.

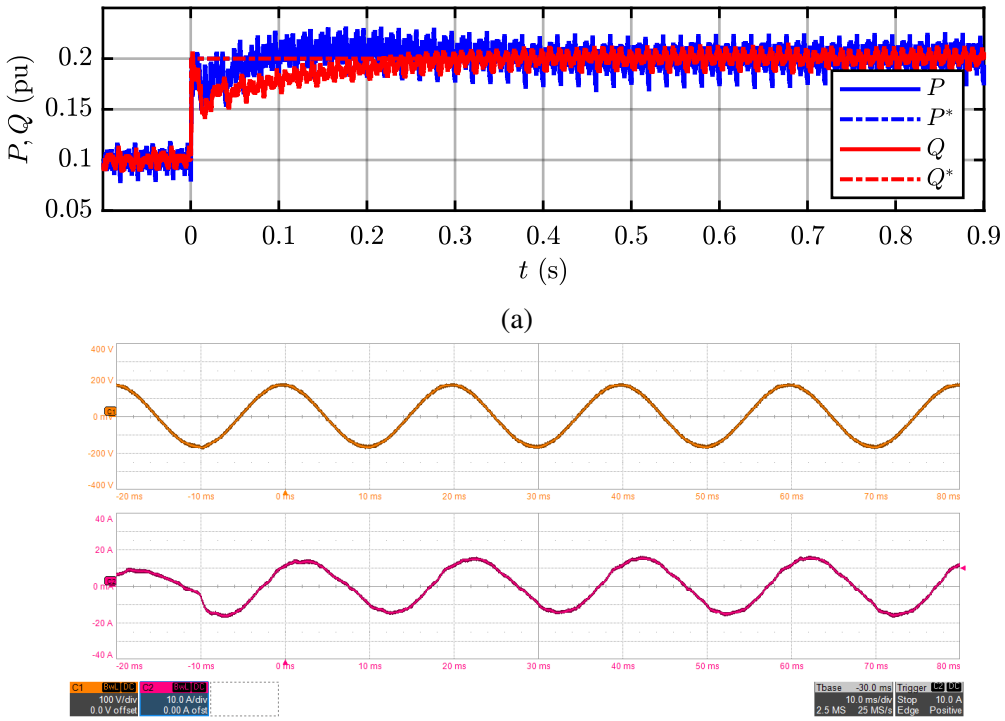

(a)

(b)

Figure 4.4: Active P^* and reactive Q^* power reference step (from 0.1 pu to 0.2 pu). From top to bottom:
a) Active and reactive power transient. The feed-forward term of the excitation control is disabled;
b) Ch1, phase voltage a at the PCC (100 V / div). Ch2, phase current i_a (10 A / div).

4.3 Inertial Behavior

The following tests highlight the effective inertial behavior of the S-VSC, which injects active power into the grid to reduce the Rate of Change of Frequency (RoCoF) and increase the frequency nadir. The results are presented in Fig. 4.5 and Fig. 4.6.

A realistic grid frequency fault profile (e.g. after a major generator disconnection from the grid) has been emulated by the grid emulator in the first test. The profile parameters (i.e., frequency derivative, frequency nadir and frequency after fault) have been chosen in order to increase the active power injected from the S-VSC and make the results more evident. As it can be seen in Fig. 4.5, the active power is injected transiently (initial few seconds span) to support the grid frequency. In the final instants of the fault (after 20–25 s), no active power is injected, as the derivative of the frequency is zero and the grid frequency has reached its post-fault value. An additional active droop controller can be included if the S-VSC is required to contribute to the primary regulation of the frequency.

As already demonstrated in 3.3.6, thanks to the RQ-based damping, the active droop and the damping feature are fully decoupled. This allows the most appropriate tuning of the active droop coefficients (usually in the range 2–5% [2]) without affecting the VSM damping performance. In the second inertial test (Fig. 4.6) a less realistic, but exemplary, triangular wave profile of the frequency has been imposed (± 1 Hz deviation from the rated 50 Hz, 10 s period). This test shows more clearly the inverse proportionality of the active power injection to the grid frequency derivative. In fact, when the grid frequency rises (or decreases) linearly, the active power injection is a negative (or positive) constant value, depending on the set inertia constant H of the S-VSC.

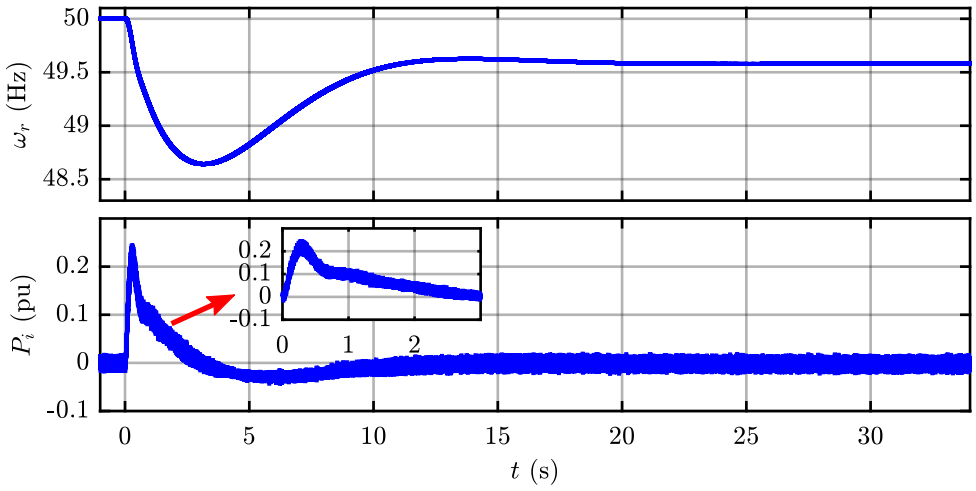

Figure 4.5: Inertial contribution of S-VSC during realistic grid frequency drop.
Top: Grid and S-VSC frequency (Hz);
Bottom: Active power reference from S-VSC (pu).

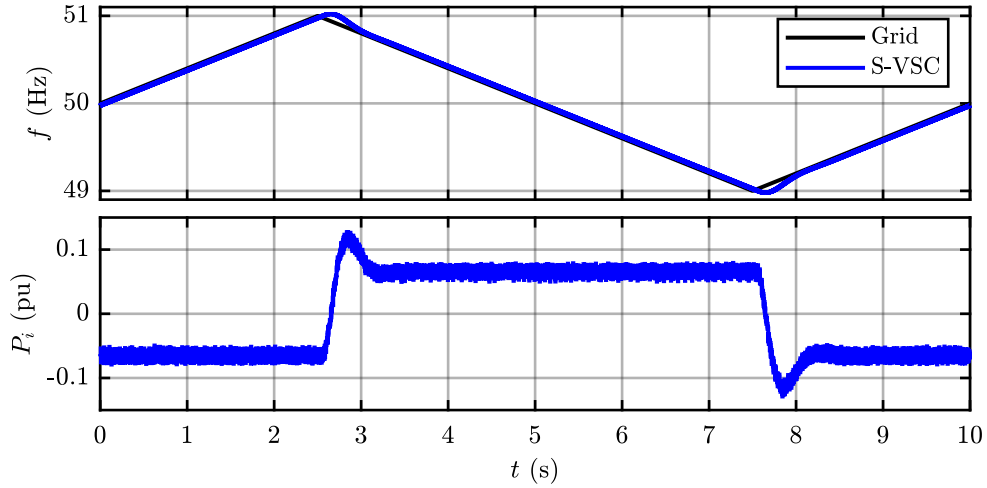

Figure 4.6: Inertial contribution of S-VSC. Grid frequency varies triangularly between 49 and 51 Hz with a period of 10 s.
Top: S-VSC frequency (Hz);
Bottom: Active power injected into the grid (pu).

In summary, the S-VSC is fully capable of guaranteeing virtual inertia in case of grid frequency variations. The inertial power injection is proportional to the virtual inertia constant H, which is a design parameter of the S-VSC and it is fully tunable by the final user. Moreover, the inertial effect is fully independent from the primary regulation of the frequency, enabling the user to add an optional active droop controller with full control on the tuning of its values.

4.4 Reactive Support During Faults

The S-VSC response in case of voltage dips has been tested and the results are described in this section. Voltage dip depths suggested by the international grid standards have been chosen. In particular, a $-10\,\%$ voltage dip was applied by the grid emulator, according to the standards EN 50160 and IEC/TR 61000-2-8:2002. The results are available in Fig. 4.7. Two aspects must be noticed. First, the current limitation strategy described in Section 3.6.1, is working within the specifications. The current reference amplitude is saturated to its maximum set value (36 A in this test). This limitation is also proved by the phase current waveforms in Fig. 4.7b. Second, the inverter injects reactive current during the fault to support the grid voltage and trigger the protection relays.

The large oscillations that can be seen in the first instants of the fault (Fig. 4.7a) are 50 Hz oscillations in the (d,q) rotating frame. These oscillations correspond to a

unidirectional current component in the three-phase stationary frame, as it can be seen from the scope screen of Fig. 4.7b.

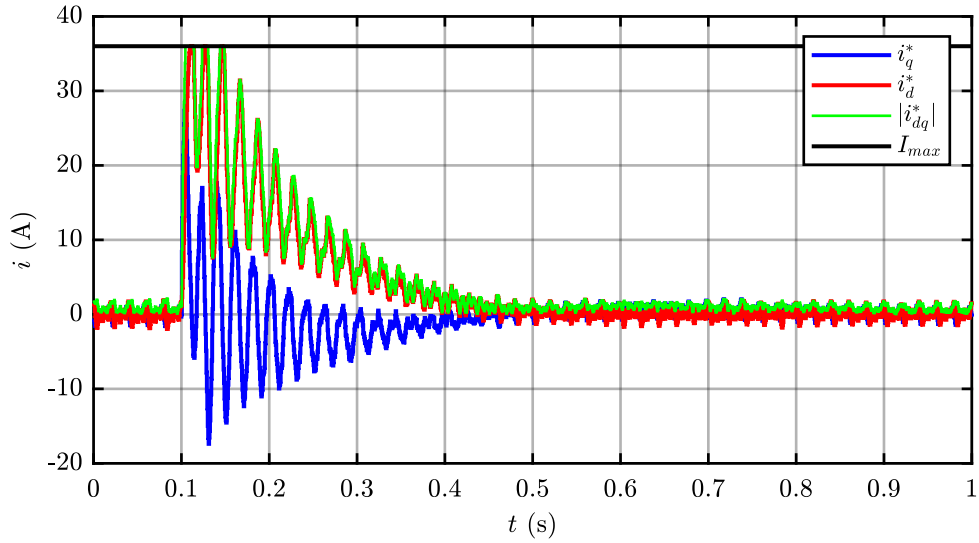

(a)

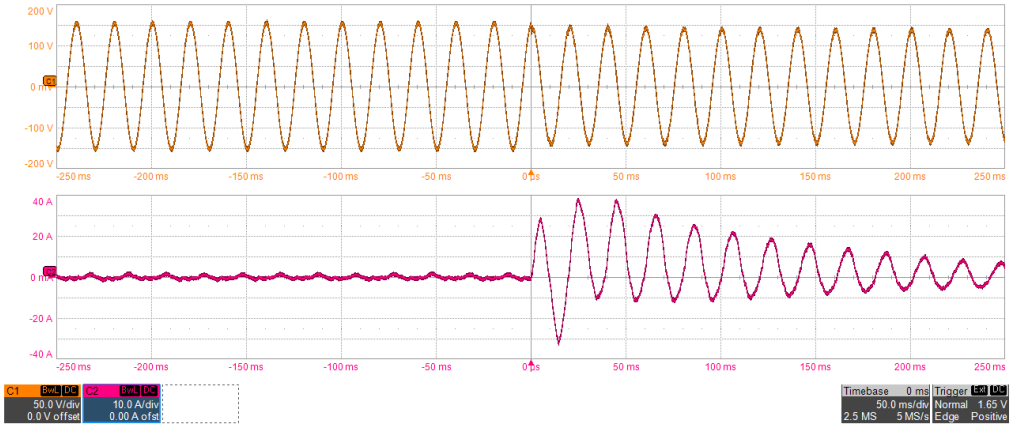

(b)

Figure 4.7: Voltage dip fault according to EN 50160 and IEC/TR 61000-2-8:2002. Voltage dip from 92 % to 82 % of the nominal voltage. From left to right:
a) Inverter reference currents (A) in the (d,q) frame;
b) Ch1, voltage at PCC (50 V / div). Ch2, grid side phase current (10 A / div).

A second test was aimed to demonstrate the reaction in case of voltage swells. The opposite perturbation (10 % voltage) was applied. As it can be seen in Fig. 4.8, the S-VSC absorbs reactive power, contributing to reduce the voltage swell. Again, the current limitation strategy is active and protecting the converter. It is also clear the current unidirectional component in the early part of the fault.

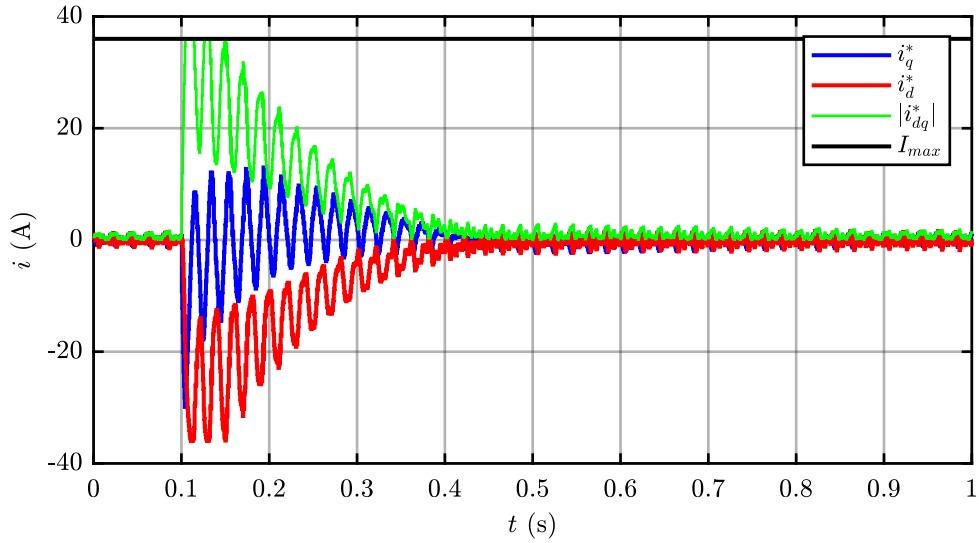

(a)

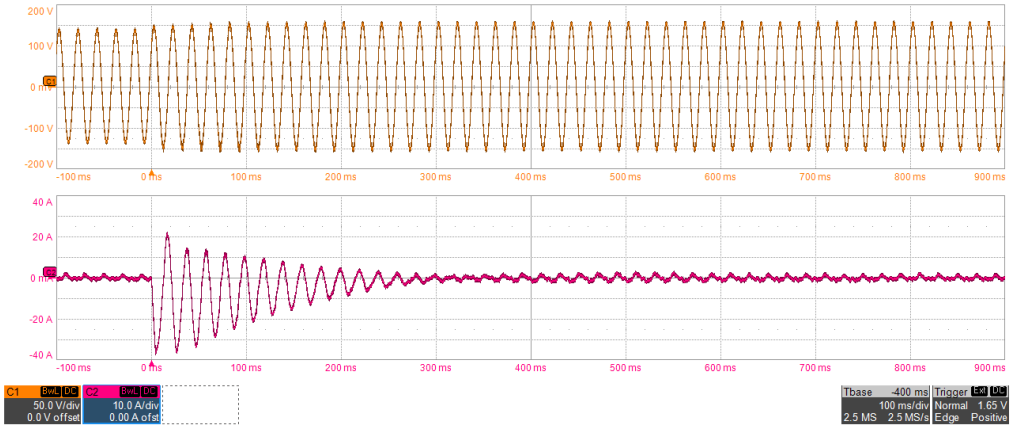

(b)

Figure 4.8: Voltage swell 10 %. From left to right:
a) Inverter reference currents (A) in the (d,q) frame;
b) Ch1, voltage at PCC (50 V / div). Ch2, grid side phase current (10 A / div).

After having tested the S-VSC against voltage dips and swells, the influence of the parameters (i.e., virtual stator resistance and excitation time constant) on the S-VSC behavior has been tested and the results are reported in Figs. 4.7 to 4.11. For these tests, the same perturbation has been applied from the grid emulator: a permanent voltage dip of −10 % with a phase jump of −5°.

Initially a benchmark test with excitation control enabled (τ_e = 100 ms) and small stator virtual resistance (R_s = 0.02 pu) was performed. As before, the virtual machine provides full transient reactive support to the grid with the set time constant. Moreover, the reference current is clamped to the limit value I_{max} (set to 36 A in such tests).

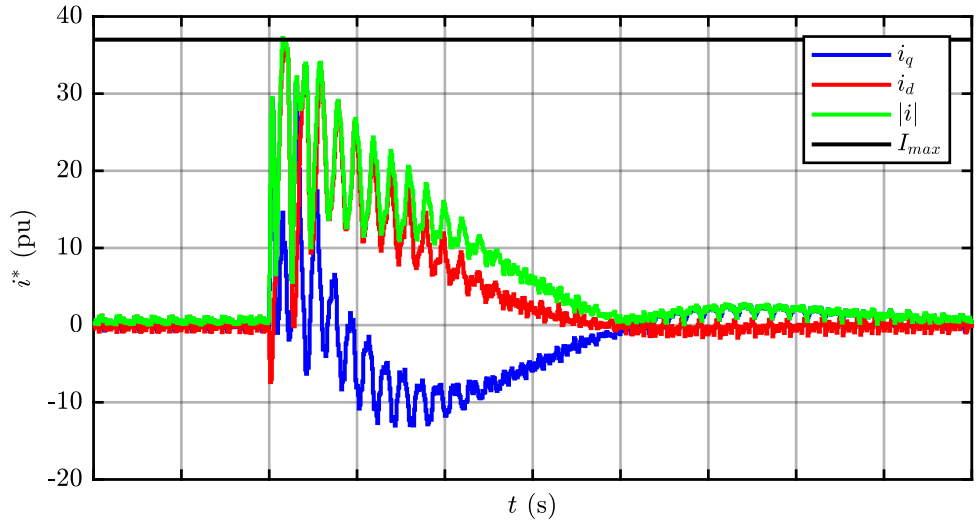

(a)

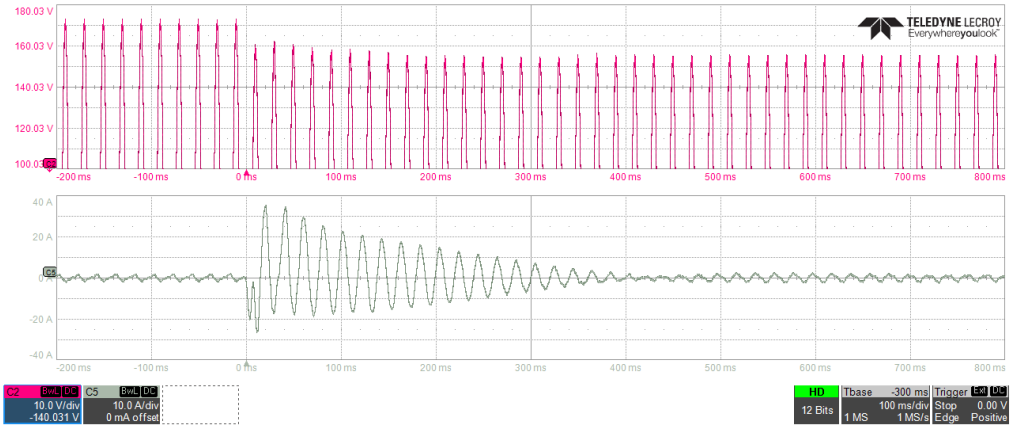

(b)

Figure 4.9: Voltage Dip Fault (-0.1 pu and −5°). S-VSC with excitation control enabled: $\tau_e = 0.1$ s, $R_s = 0.02$ pu. Top to bottom:
a) Inverter currents (A) in the (d,q) frame;
b) Ch2, Positive envelope of the voltage at PCC (10 V / div). Ch5, phase current i_a (10 A / div).

Then, the excitation control was disabled (i.e., $k_e = 0$). The result, shown in Fig. 4.10, demonstrates that permanent grid support can be provided if the excitation control is disabled. Since there is no reactive regulation, the excitation flux linkage λ_e of the virtual machine is constant and equal to its value before the fault.

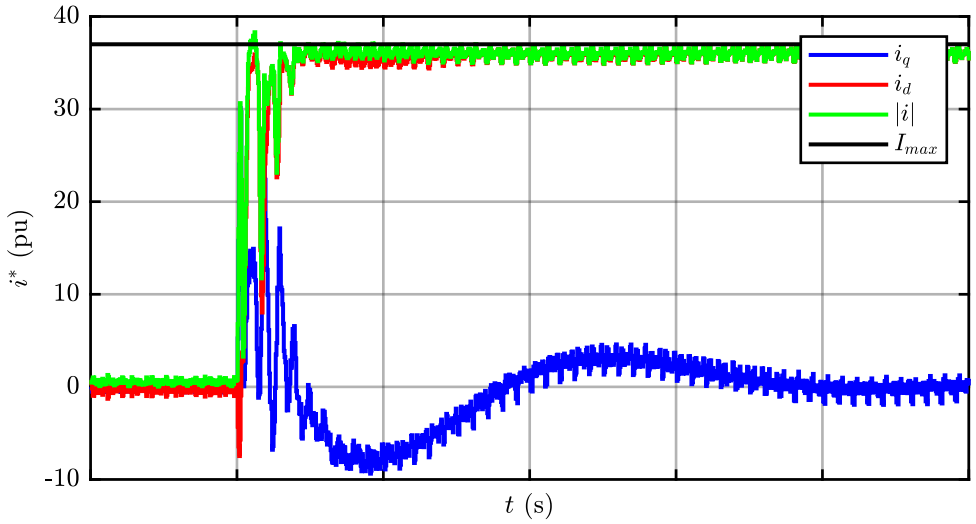

(a)

(b)

Figure 4.10: Voltage Dip Fault (-0.1 pu and $-5°$). $R_s = 0.02$ pu and excitation control disabled: $k_e = 0$. From top to bottom:
a) Inverter currents (A) in the (d,q) frame;
b) Ch2, Positive envelope of the voltage at PCC (10 V / div). Ch5, phase current i_a (10 A / div).

Finally, the virtual stator resistance R_s was increased up to $R_s = 0.2$ pu. While the virtual stator inductance L_s regulates the amplitude of the transient support, R_s sets the damping of its response and the duration of the unidirectional component of the fault current (50 Hz oscillations in the rotating (d,q) frame). As it can be seen in Fig. 4.11, a higher resistance leads to a more damped transient after the fault occurred. This does not effect though the steady state operation, which is determined only by L_s and λ_e.

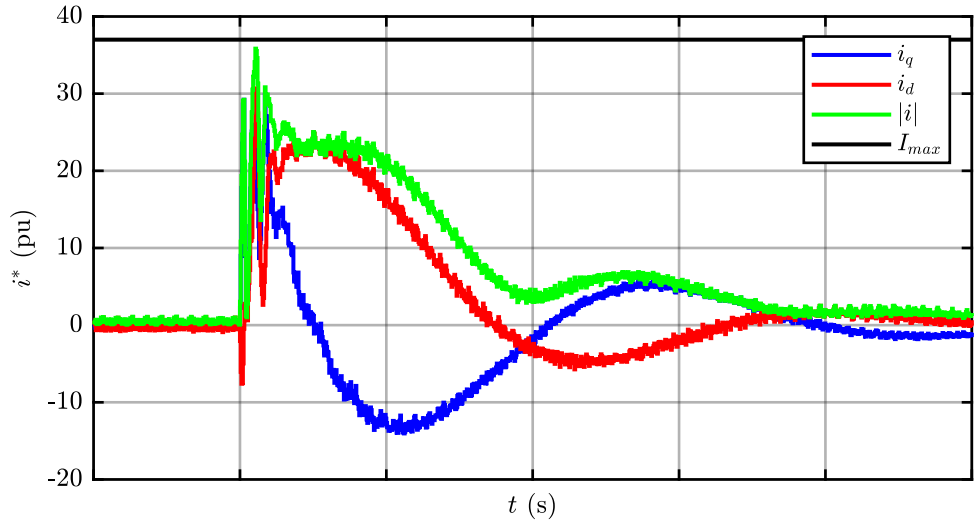

(a)

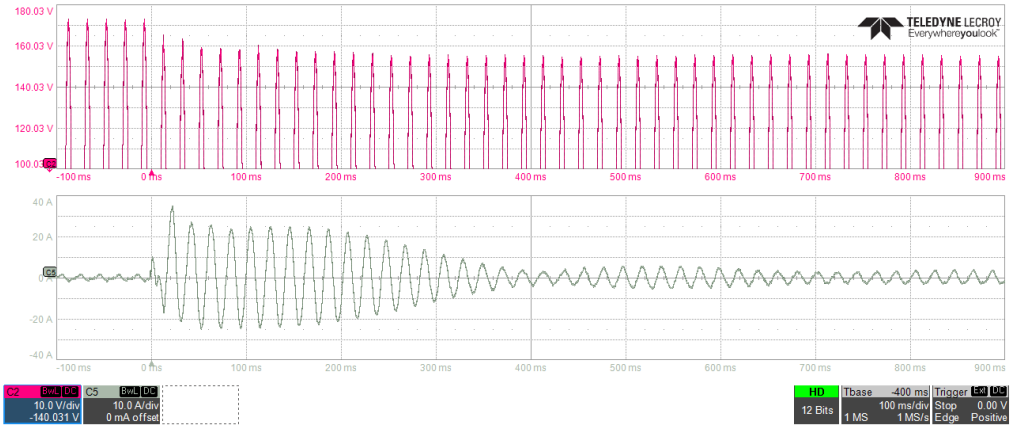

(b)

Figure 4.11: Voltage Dip Fault (-0.1 pu and −5°). S-VSC with large resistance R_s = 0.2 pu and excitation control enabled. From top to bottom:
a) Inverter currents (A) in the (d,q) frame;
b) Ch2, Positive envelope of the voltage at PCC (10 V / div). Ch5, phase current i_a (10 A / div).

The outcomes of these tests can be summarized as follows:

- The S-VSC is capable of injecting/absorbing reactive power during voltage dips and swells;
- The fault response profile can be modified in terms of amplitude (varying L_s), duration (τ_e) and unidirectional current component (R_s) according to the user design data;

- The current reference limitation strategy and the current controller are able to limit the injected/absorbed current within the given constraints.

4.5 Harmonic Compensation

The harmonic compensation capabilities has been tested under a distorted grid, generated by the grid emulator. A 5 % 5th harmonic voltage distortion has been introduced. The system is operating at no load, so that the effect of the harmonic compensation is clearly highlighted.

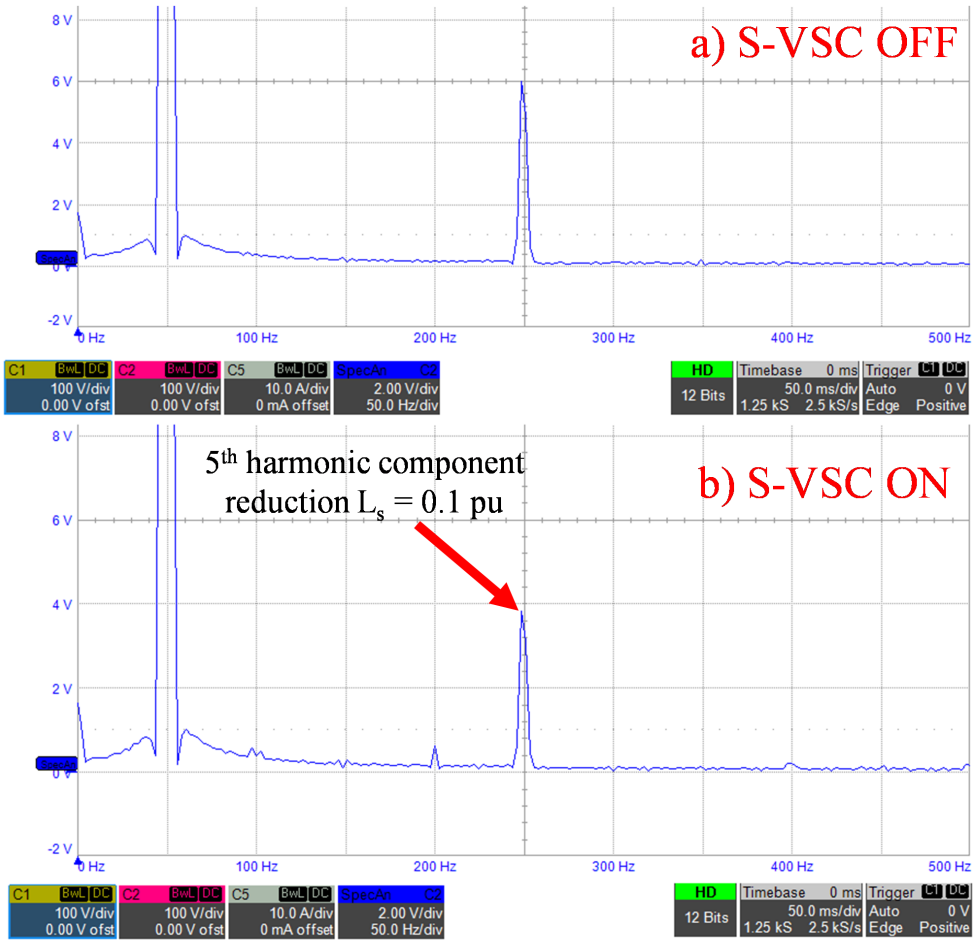

Figure 4.12: Harmonic compensation test. A 5% 5th harmonic component has been introduced into the emulated grid. A comparison with the S-VSC enabled and disabled is carried out. $L_s = 0.1$ pu. From top to bottom:
a) FFT of the voltage at the PCC when the S-VSC is off;
b) FFT of the voltage at the PCC when the S-VSC is on.

The beneficial effect of the S-VSC is clear as resulting from the FFT analysis of Fig. 4.12. The 5th harmonic content in the grid voltage has been attenuated from 6 V to 4 V, proving the effectiveness of the S-VSC harmonic compensation feature. The compensation effect is also evident from the time-domain waveforms. The current and voltage waveforms at the PCC are displayed in Fig. 4.13. The line-line voltage (yellow) shows the typical 5th harmonic distortion, which shaves the peaks of the line-line voltage. If the S-VSC is off, the converter does not inject or absorbs current (Fig. 4.13a).

As soon as the S-VSC is switched on (Fig. 4.13b), compensating current references are generated according to (3.6). The current contains a 5th harmonic component that contributes in reducing the magnitude of the voltage distortion. In this thesis, as mentioned in section 3.6.2, the current control has been implemented in the (d,q) S-VSC frame using PI and resonant controllers on the 6th harmonic. Without such resonant controllers, the quality of the current reference tracking would have been much lower, thus decreasing the effectiveness of the harmonic compensation. It is therefore crucial to employ suitable current controller (e.g. resonant, MPC...) to ensure the correct tracking of the compensation current references.

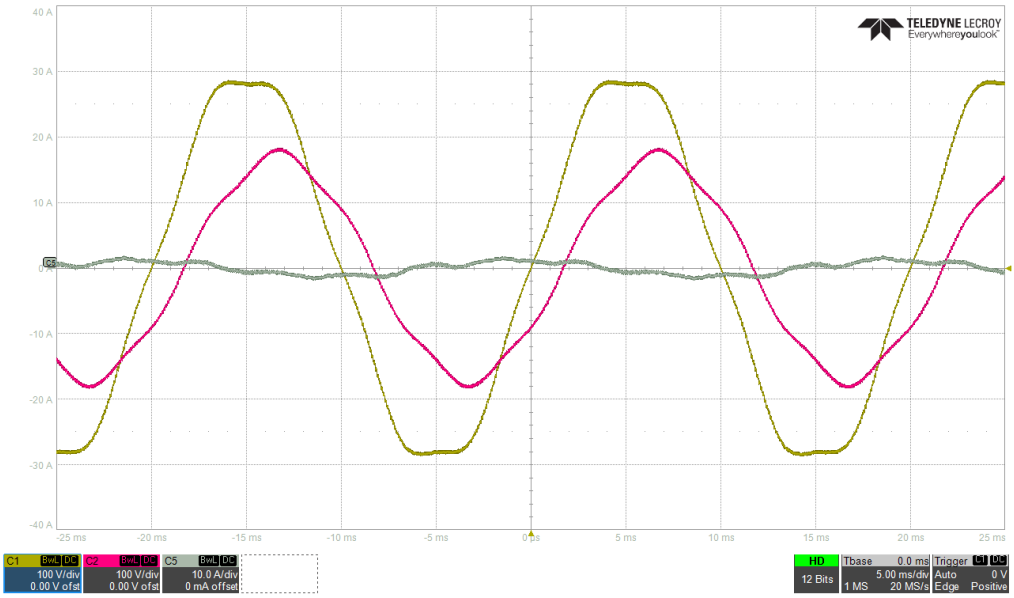

(a)

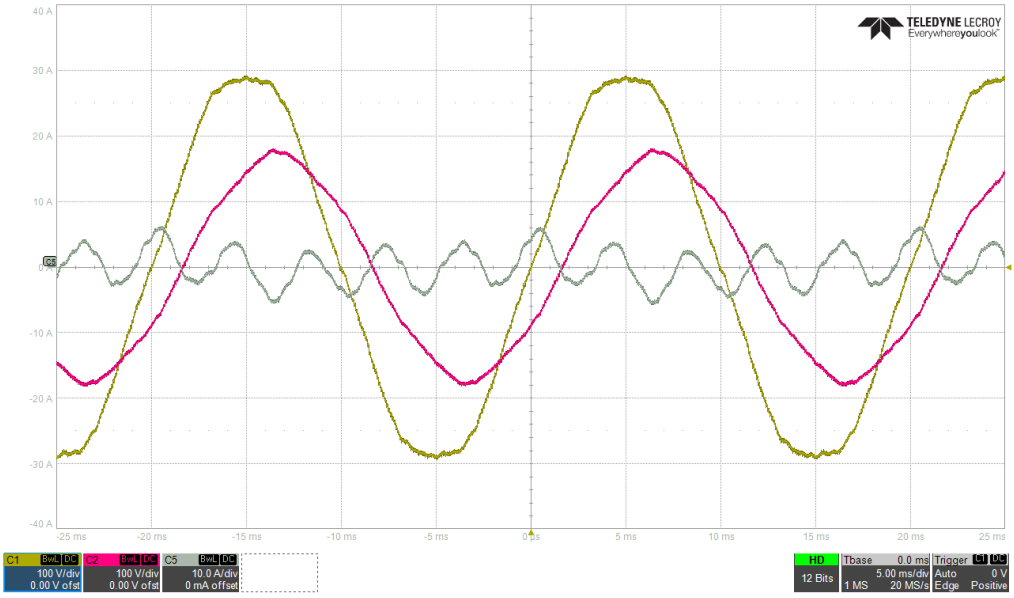

(b)

Figure 4.13: Harmonic compensation test. Current and voltage waveforms at PCC. C5 phase current (A), C2 phase voltage (V) and C1 line-line voltage (V). From top to bottom:
a) S-VSC is off;
b) S-VSC is on.

As mentioned in 3.2.5, the harmonic compensation is tunable and depends on the virtual inductance L_s of the stator. To prove it, a further test has been performed setting $L_s = 0.05$ pu. The FFT of the voltage at the PCC is shown in Fig. 4.14. The residual

component of the 5th harmonic is in this case 2.8 V. Comparing this result with the previous test (Fig. 4.12), it can be noted that the 5th harmonic is further reduced of 50 %. As foreseen, this effect is inversely proportional to the virtual stator inductance L_s. A smaller virtual stator inductance L_s generates a larger compensating current and, therefore, the voltage distortion is further reduced.

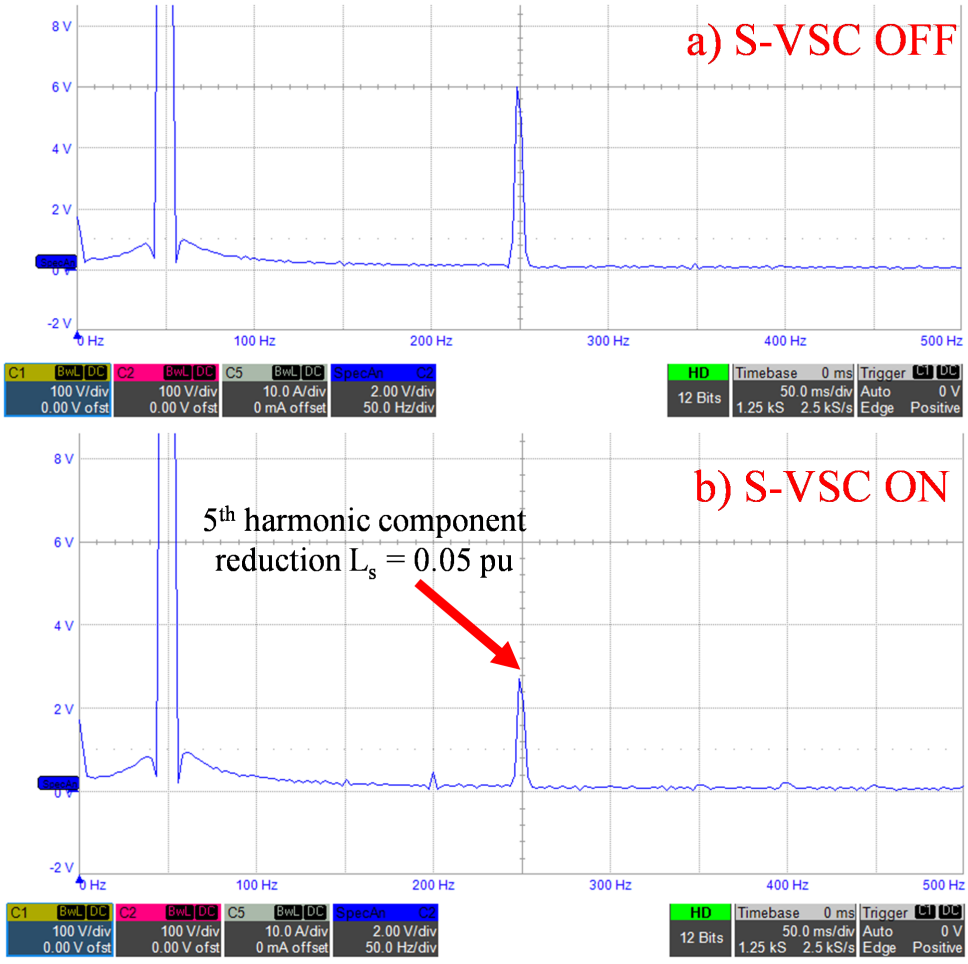

Figure 4.14: Harmonic compensation test. A 5% 5th harmonic component has been introduced into the emulated grid. A comparison with the S-VSC enabled and disabled is carried out. L_s = 0.05 pu. From top to bottom:
a) FFT of the voltage at the PCC when the S-VSC is off;
b) FFT of the voltage at the PCC when the S-VSC is on.

Chapter 5

Modeling of Converters for System Level Stability Studies

After having presented the S-VSC model and its experimental validation as a single converter connected to the electric grid, it is necessary to describe how to model it for system-level studies. In fact, the increasing penetration of electronic-interfaced renewable energy sources may lead to instabilities within the electric power system [20, 96]. Therefore, accurate models of the converters and their control are necessary. Moreover, this necessity has also been translated into grid codes requirements. The Italian TSO Terna is for example requiring models of different detail for the simulation and analysis at the power system level [6, 7].

Traditional power system modeling and analysis, has been working with much larger time constants (electromechanical transients) compared to modern electronic converter (switching frequency). In modern static converters, these time constants are related to the physical hardware of the converter (e.g. LCL filters) and the digital current/voltage controllers. However, to integrate more renewable energy sources into the grid, power converters may be also asked to provide ancillary services (frequency, voltage and harmonic content) to the grid, in order to maintain its stability and power quality. These services, differently from the inner converter controllers, operate with much smaller time constants, similar to the traditional synchronous machines. Therefore, a multi time scale analysis of the system, focusing only of certain time scales of interest, may be necessary. Also, simplified models may be desirable, in order to focus only on specific phenomena, with the goal of reducing the computational burden of the analysis, which would be otherwise excessive and would provide redundant results.

With the recent increase in the share of distributed generation from renewable energy sources interfaced by power electronics converters, accurate and computationally efficient modeling techniques have become necessary. These techniques are required flexibility (i.e. can be applied to different systems easily), scalability (i.e. can model more converters/loads and can merge together multiple grid sub-portions) and a selectable level of detail, to model certain phenomena, while neglecting others.

Therefore, during the years, several levels of complexity and detail have been proposed. Initially, the research focused on subsynchronous oscillations, therefore neglecting the behavior of current/voltage controllers [97], being it much faster. In these studies, the converter was considered a voltage source, ideally controlled in its frequency and amplitude by active and reactive droop controllers. While being valid for low frequency oscillations, these simplifications prevent from predicting instabilities or underdamped resonances at higher frequencies (related to the innermost current or voltage control bandwidth and grid-side filters resonance frequency). Therefore, more accurate models have been proposed [98, 99], which model more accurately the high frequency behavior of the power converters.

Given this introduction, it can be said that the following features are needed to model power converters for system-level studies:

- The modes of the system must be evident in their frequency and damping, so that poorly damped oscillations are easily identified;
- Analysis of the relation between the modes and the states of the system, to identify the states associated with the most critical modes;
- Possibility to derive a reduced order model of the system, by neglecting the dynamic behavior of some of its parts. This allows shorter simulation time with an acceptable quality of the results.

The content of this chapter has been published in [100].

5.1 Possible Converter Modeling Techniques

Given the need of system level converter modeling, several techniques have been proposed. Two are the most popular approaches: frequency domain analysis using impedance models and the eigenvalue analysis using state-space models [101]. Various frequency domain analysis approaches have been presented in the literature [102–107], as well as experimental characterization procedures [108] aimed to obtain the black-box frequency response of a converter without any knowledge of its internal hardware or software parameters. This technique is extended to system-level analysis by applying the Generalized Nyquist Criterion [109], combining the equivalent impedance models of various converters connected to the grid. Unfortunately, these impedance models are more difficult to interpret in terms of comprehension of the poles in the system and how these poles are influenced by the parameters of the system. Moreover, the frequency domain representation (using Bode plots) of the equivalent impedance of these converters leads to pole-zeros cancellation.

On the other hand, the state-space modeling clearly identify the modes of the analyzed system and their correlation to its states (e.g. filter and controller variables) by means of participation factors [2] and also to the parameters of the system (e.g. tuning values)

thanks to the sensitivity analysis. Moreover, a state-space model provides an immediate feedback of the time constants of the system, without the effects of zero-pole cancellation, that can be present in the impedance model representation.

However, the state-space modeling process can be an analytically demanding task, if applied to complex systems with many interconnections. A higher number of state variables, inputs and outputs leads eventually to complicated matrix expressions. Moreover, the low flexibility is a serious disadvantage: if new components are added to the system, others removed or modified, the modeling process must be reiterated. This drawback is especially evident when modeling power converters featuring with advanced cascaded or more emerging controllers, such as the S-VSC.

In the technical literature some examples of state-space modeling of such controllers [69] are available, but following the classical monolithic approach, i.e. deriving the complete model at once. This approach leads to valid results, but it lacks of scalability, modularity and flexibility (i.e. if any part of the model is modified, then it must be derived again). Moreover, the large amount of state variables increases the order of the obtained system. Thus, the complexity of this modeling technique leads involves a larger effort and it is prone to calculation errors. Therefore, troubleshooting cannot be easily done during the derivation of the model.

A sound approach to tackle these problems is the Component Connection Method (CCM). The CCM provides modularity and simplifies the modeling procedure. At the same time, it reduces the analytical modeling effort and the likelihood of mistakes during the derivation process, by individually modeling the single components of the system and then connecting them using sparse interlinking matrices, as shown in Figure 5.1. The global system is finally derived by combining the individual component.

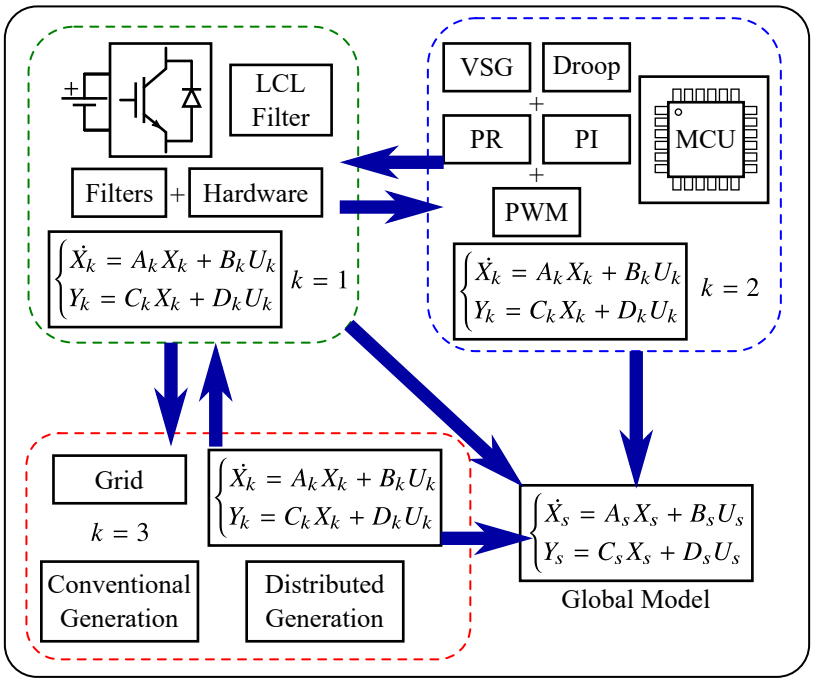

Figure 5.1: Modular state-space modeling of a grid connected converter including controllers.

Traditionally, CCM has been employed in power system studies to analyze multi-node networks featuring several conventional generating units (SGs) and loads starting from [110]. Later, it was used more specifically to model the early grid applications of power electronics: static var compensators and HVDC transmission systems [111, 112]. In the last decade, with the exponential growth of inverter-based electrical energy conversion, CCM has gained renewed interest and it was applied to modern power electronics-based power systems. In 2014 CCM was applied to model wind farms and their connection to the main grid [104, 113, 114]. The same research group extended this work and applied it to CCM modeling of multiple converters power systems, including detailed converter models (i.e. accurate control loops and digital delays modeling) in wider inverter-based power systems.

CCM is currently employed in the stability and interaction analysis between conventional (i.e. grid-following converters) and new breeds of controllers (i.e. Synchronverters) for renewable generation [115–117]. In these publications, the CCM is just the first step towards a more advanced state-space μ-analysis [117] to consider the uncertainties of the modeled plants.

CCM is still adopted in power system studies, to include converter-based grid nodes into larger scale studies (e.g. the study on subsynchronous torsional interactions in [118]). In these cases, its flexibility is exploited and the modeling procedure is simplified to neglect aspects at frequency out of the range of interest (e.g. digital control delay).

5.2 Generalized CCM Modeling Workflow

It is first useful to present a generalized approach to explain CCM modeling, which will be applied to the S-VSC. The CCM models in a modular way the system under study. First, the individual blocks must be identified and linearized around the desired operating point. Then, interlinking matrices relate each block and define the connections among them. Finally, by algebraically combining the single blocks and the interconnection matrices, the complete state-space model of the system under study is obtained.

This process is summarized by the step-by-step procedure described below:

1. Definition of the system under study global inputs U_s and outputs Y_s. The inputs might be external disturbances, such as setpoints variations (e.g. active and reactive power) or grid fault conditions (i.e. frequency, voltage amplitude or phase variations). The outputs, on the other hand, can be chosen arbitrarily, depending on the aspect, which is studied. For example, the power (or current) injected by the converter and the measured grid frequency using PLLs or VSMs;

2. Identification of the single blocks. Two kinds of blocks can be identified: dynamic (containing state variables) and algebraic (not containing state variables). In general, n dynamic components and m algebraic components are identified;

3. Each component is linearized around the desired operating point (e.g. voltage level, frequency...);

4. Each k-th linearized dynamic component (e.g. LCL filters, integral regulators...) must be written in the state-space form:

$$\begin{cases} \dot{X}_k &= A_k X_k + B_k U_k \\ Y_k &= C_k X_k + D_k U_k \end{cases} \qquad k = 1 \dots n \tag{5.1}$$

   where X_k is the vector of the state variables of the component, U_k are the inputs of the block and Y_k are its relative outputs. The matrices A_k, B_k, C_k and D_k are the component state-space matrices.

5. Algebraic components are defined to simplify the modeling procedure. In the conventional state-space modeling, only dynamic components are present. However, the introduction of algebraic blocks is very useful when modeling a controller. Many purely algebraic calculations, such as multiplications and divisions, involve complicated linearized expressions and it is efficient to simplify this process by introducing such algebraic block. They do not contain state variables, but only relate the inputs U_k and the outputs Y_k as:

$$Y_k = D_k U_k \qquad k = n+1 \dots n+m \tag{5.2}$$

A practical example of algebraic components are: sums and divisions for current reference calculation starting from the power references and droop controllers.

6. By aggregating the X_k state variable vectors of the single blocks, the vector X_s of the state variables of the global system is obtained. Similarly, the list of the components inputs U and the list of the components outputs Y are defined as follows:

$$\begin{aligned} X_s &= [X_1 \dots X_n]' \\ U &= [U_1 \dots U_{n+m}]' \\ Y &= [Y_1 \dots Y_{n+m}]' \end{aligned} \tag{5.3}$$

7. By combining the algebraic and dynamic components, an aggregated model is defined as follows:

$$\begin{cases} \dot{X}_s = A_a X_s + B_a U \\ Y = C_a X_s + D_a U \end{cases} \tag{5.4}$$

where:

$$A_a = \begin{bmatrix} A_1 & 0 & \cdots & 0 \\ 0 & A_2 & \cdots & 0 \\ \vdots & \vdots & \ddots & \vdots \\ 0 & 0 & \cdots & A_n \end{bmatrix}$$

$$B_a = \begin{bmatrix} B_1 & 0 & \cdots & 0 & \overbrace{0 & \cdots & 0}^{\text{number of algebraic blocks inputs}} \\ 0 & B_2 & \cdots & 0 & 0 & \cdots & 0 \\ \vdots & \vdots & \ddots & \vdots & \vdots & \ddots & \vdots \\ 0 & 0 & \cdots & B_n & 0 & \cdots & 0 \end{bmatrix} \tag{5.5}$$

$$C_a = \left.\begin{bmatrix} C_1 & 0 & \cdots & 0 \\ 0 & C_2 & \cdots & 0 \\ \vdots & \vdots & \ddots & \vdots \\ 0 & 0 & \cdots & C_n \\ 0 & \cdots & \cdots & 0 \\ \vdots & \vdots & \ddots & \vdots \\ 0 & \cdots & \cdots & 0 \end{bmatrix}\right\} \begin{array}{l}\text{number of algebraic} \\ \text{blocks outputs}\end{array}$$

$$D_a = \begin{bmatrix} D_1 & 0 & \cdots & 0 \\ 0 & D_2 & \cdots & 0 \\ \vdots & \vdots & \ddots & \vdots \\ 0 & 0 & \cdots & D_{n+m} \end{bmatrix}.$$

To cope with the introduction of the algebraic blocks, the B_a and C_a matrices of (7) must be extended and null elements are added. In detail, as many null columns as the total amount of inputs of all the algebraic blocks is to be attached to the B_a matrix. Similarly, as many null rows as the sum of the algebraic block outputs must be added to the C_a matrix.

8. The connection of the single components is performed by defining the connection matrices.

   These connection matrices T are generally sparse and relate the inputs and outputs of the single blocks and the global system as follows:

$$\begin{aligned} U &= T_{uy}Y + T_{us}U_s \\ Y_s &= T_{sy}Y + T_{ss}U_s \end{aligned} \tag{5.6}$$

9. The global linearized system state-space model is finally obtained as:

$$\begin{cases} \dot{X}_s &= A_sX_s + B_sU_s \\ Y_s &= C_sX_s + D_sU_s \end{cases} \tag{5.7}$$

   where:

$$\begin{aligned} A_s &= A_a + B_a T_{uy} W C_a \\ B_s &= B_a T_{uy} W D_a T_{us} B_a T_{us} \\ C_s &= T_{sy} W C_a \\ D_s &= T_{sy} W D_a T_{us} + T_{ss} \\ W &= \left(I - D_a T_{uy}\right)^{-1}. \end{aligned} \tag{5.8}$$

If the system structure needs modifications, then the single blocks and interconnection matrices have to be modified according to the system structure.

5.3 Component Connection Method Applied to the S-VSC

In this section, the proposed S-VSC is modeled using CCM. The system is composed by the converter hardware part, its control (current controller and the S-VSC) and the connection to the grid, represented by its Thévenin equivalent circuit, as shown in Fig. 5.2. In this analysis the RQ-damping has been used. A similar procedure can be applied to model other damping methods.

5.3.1 Definition of System Inputs and Outputs

Following the step-by-step procedure of the previous section, the inputs and the outputs of the system must be defined first. The inputs U_s of the system are defined so to model the possible electrical perturbations that can affect the system. This means step variations of the active and reactive power references (ΔP^*, ΔQ^*), grid frequency $\Delta\omega_g$, grid voltage amplitude ΔE_g and grid voltage phase angle $\Delta\phi_g$ variations. Thanks to these inputs, the S-VSC can be fully tested under normal and abnormal grid operating conditions.

The system outputs Y_s are here selected to analyze the most significant hardware and control variables of the system (power, voltages, current and S-VSC virtual mechanical variables):

$$\begin{aligned} U_s &= \left[\Delta P^*, \Delta Q^*, \Delta\omega_g, \Delta E_g, \Delta\phi_g\right]'_{5\times1} \\ Y_s &= \left[\Delta P_i, \Delta Q_i, \Delta\omega_r, \Delta\delta, \Delta v_g^d, \Delta v_g^q\right]'_{6\times1} \end{aligned} \tag{5.9}$$

where ΔP_i and ΔQ_i are the active and reactive powers injected by the inverter.

5.3.2 Component Identification

The second step is the identification of the blocks composing the system, as highlighted in Fig. 5.2. In total, $n = 4$ dynamic blocks and $m = 2$ algebraic blocks are defined as follows:

- **Dynamic components:** LCL filter, Inverter control loops (PI and delay model), S-VSC electrical part (stator and damper), S-VSC power loops (mechanical part and excitation control);
- **Algebraic components:** Power reference calculation (power to current) and grid perturbation model.

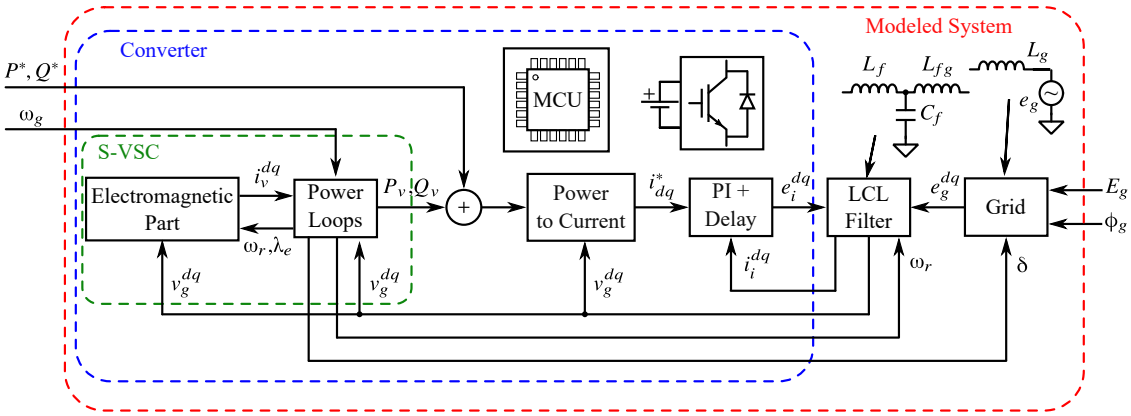

Figure 5.2: Block diagram of the modeled S-VSC control connected to the physical system.

5.3.3 Dynamic Components Definition

LCL Filter

The inverter is interfaced to the grid by means of an LCL filter, as shown in Fig. 5.3. The LCL filter is modeled in the (d,q) frame synchronous to the S-VSC virtual rotor position θ_r, rotating at ω_r.

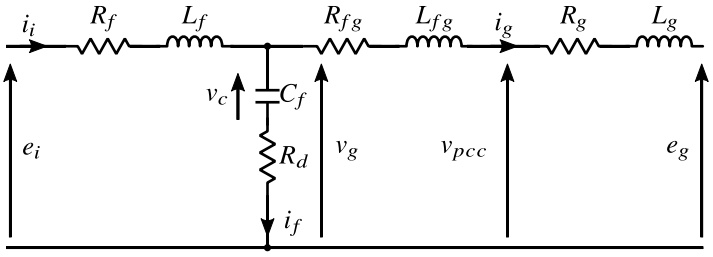

Figure 5.3: LCL filter model in the stationary (α,β) frame.

This block has the following state variables X_{LCL}, inputs U_{LCL} and outputs Y_{LCL}:

$$\begin{aligned} X_{LCL} &= \left[\Delta i_i^d, \Delta i_i^q, \Delta i_g^d, \Delta i_g^q, \Delta v_c^d, \Delta v_c^q\right]'_{6\times1} \\ U_{LCL} &= \left[\Delta e_i^d, \Delta e_i^q, \Delta e_g^d, \Delta e_g^q, \Delta\omega_r\right]'_{5\times1} \\ Y_{LCL} &= \left[\Delta i_i^d, \Delta i_i^q, \Delta v_g^d, \Delta v_g^q, \Delta v_{pcc}^d, \Delta v_{pcc}^q\right]'_{6\times1} \end{aligned} \tag{5.10}$$

The output v_{pcc} is useful if a multi-inverter plant is modeled, where the voltage amplitude control at the plant Point of Common Coupling (PCC) .

The necessary state-space matrices $A_{LCL}, B_{LCL}, C_{LCL}, D_{LCL}$ are obtained, by linearizing the equations describing this component (in per unit):

$$\begin{aligned} e_i^{dq} - v_g^{dq} &= \frac{L_f}{\omega_b}\left(\frac{di_i^{dq}}{dt} + j\omega_r\omega_b i_i^{dq}\right) + R_d i_i^{dq} \\ v_g^{dq} - e_g^{dq} &= \frac{L_{fg}+L_g}{\omega_b}\left(\frac{di_g^{dq}}{dt} + j\omega_r\omega_b i_g^{dq}\right) + (R_{fg}+R_g) i_g^{dq} \\ \frac{C_f}{\omega_b}\frac{dv_c^{dq}}{dt} &= i_i^{dq} - i_g^{dq} - jC_f\omega_r v_c^{dq} \end{aligned} \tag{5.11}$$

The LCL circuit equations of (5.11) are linearized obtaining:

$$\begin{aligned} \Delta e_i^d - \Delta v_g^d &= R_f\Delta i_i^d + \frac{L_f}{\omega_b}\frac{d\Delta i_i^d}{dt} - L_f\omega_0\Delta i_i^q - L_f I_{i0}^q\Delta\omega \\ \Delta e_i^q - \Delta v_g^q &= R_f\Delta i_i^q + \frac{L_f}{\omega_b}\frac{d\Delta i_i^q}{dt} + L_f\omega_0\Delta i_i^d + L_f I_{i0}^d\Delta\omega \end{aligned} \tag{5.12}$$

$$\begin{aligned} \Delta v_g^d - \Delta e_g^d &= (R_{fg}+R_g)\Delta i_g^d + \frac{L_{fg}+L_g}{\omega_b}\frac{d\Delta i_g^d}{dt} - (L_{fg}+L_g)\omega_0\Delta i_g^q - (L_{fg}+L_g) I_{g0}^q\Delta\omega \\ \Delta v_g^q - \Delta e_g^q &= (R_{fg}+R_g)\Delta i_g^q + \frac{L_{fg}+L_g}{\omega_b}\frac{d\Delta i_g^q}{dt} + (L_{fg}+L_g)\omega_0\Delta i_g^d + (L_{fg}+L_g) I_{g0}^d\Delta\omega \end{aligned} \tag{5.13}$$

$$\begin{aligned} \frac{C_f}{\omega_b}\frac{d\Delta v_c^d}{dt} - C_f\omega_0\Delta v_c^q - C_f V_{c0}^q\Delta\omega &= \Delta i_i^d - \Delta i_g^d \\ \frac{C_f}{\omega_b}\frac{d\Delta v_c^q}{dt} + C_f\omega_0\Delta v_c^d + C_f V_{c0}^d\Delta\omega &= \Delta i_i^q - \Delta i_g^q \end{aligned} \tag{5.14}$$

The state variables derivatives can be now highlighted:

$$\begin{aligned}
\frac{d\Delta i_i^d}{dt} &= -\omega_b\frac{R_f}{L_f}\Delta i_i^d + \omega_0\omega_b\Delta i_i^q + \omega_b I_{i0}^q\Delta\omega + \frac{\omega_b}{L_f}(\Delta e_i^d - (R_d\Delta i_i^d - R_d\Delta i_g^d + \Delta v_c^d))\\
\frac{d\Delta i_i^q}{dt} &= -\omega_b\frac{R_f}{L_f}\Delta i_i^q - \omega_0\omega_b\Delta i_i^d - \omega_b I_{i0}^d\Delta\omega + \frac{\omega_b}{L_f}(\Delta e_i^q - (R_d\Delta i_i^q - R_d\Delta i_g^q + \Delta v_c^q))\\
\frac{d\Delta i_g^d}{dt} &= -\omega_b\frac{R_{fg}+R_g}{L_{fg}+L_g}\Delta i_g^d + \omega_0\omega_b\Delta i_g^q + \omega_b I_{g0}^q\Delta\omega + \frac{\omega_b}{L_{fg}+L_g}(R_d\Delta i_i^d - R_d\Delta i_g^d + \Delta v_c^d - \Delta e_g^d)\\
\frac{d\Delta i_g^q}{dt} &= -\omega_b\frac{R_{fg}+R_g}{L_{fg}+L_g}\Delta i_g^q - \omega_0\omega_b\Delta i_g^d - \omega_b I_{g0}^d\Delta\omega + \frac{\omega_b}{L_{fg}+L_g}(R_d\Delta i_i^q - R_d\Delta i_g^q + \Delta v_c^q - \Delta e_g^q)\\
\frac{d\Delta v_c^d}{dt} &= \frac{\omega_b}{C_f}\Delta i_i^d - \frac{\omega_b}{C_f}\Delta i_g^d + \omega_b\omega_0\Delta v_c^q + \omega_b V_{c0}^q\Delta\omega\\
\frac{d\Delta v_c^q}{dt} &= \frac{\omega_b}{C_f}\Delta i_i^q - \frac{\omega_b}{C_f}\Delta i_g^q - \omega_b\omega_0\Delta v_c^d - \omega_b V_{c0}^d\Delta\omega
\end{aligned} \tag{5.15}$$

The outputs of the block are calculated as follows:

$$\begin{aligned}
\Delta v_g^d &= R_d\Delta i_i^d - R_d\Delta i_g^d + \Delta v_c^d\\
\Delta v_g^q &= R_d\Delta i_i^q - R_d\Delta i_g^q + \Delta v_c^q
\end{aligned} \tag{5.16}$$

and:

$$\begin{aligned}
\Delta v_{pcc}^d &= \frac{L_g R_d}{L_{fg}+L_g}\Delta i_i^d + \frac{R_g L_{fg} + R_{fg}L_g - L_g R_d}{L_{fg}+L_g}\Delta i_g^d + \frac{L_g}{L_{fg}+L_g}\Delta v_c^d + \frac{L_{fg}}{L_{fg}+L_g}\Delta e_g^d\\
\Delta v_{pcc}^q &= \frac{L_g R_d}{L_{fg}+L_g}\Delta i_i^q + \frac{R_g L_{fg} + R_{fg}L_g - L_g R_d}{L_{fg}+L_g}\Delta i_g^q + \frac{L_g}{L_{fg}+L_g}\Delta v_c^q + \frac{L_{fg}}{L_{fg}+L_g}\Delta e_g^q
\end{aligned} \tag{5.17}$$

The complete state space matrices of the LCL filter are available in Appendix B.

Current Controller

This model considers a digital (with sampling time T_s) PI current controller implemented in the (d,q) synchronous reference. The proportional and integral gains of the PI regulator are k_p and k_i. The digital controller and the modulation introduce a total delay $T_d = 1.5 \cdot T_s$ and this is modeled using a first order Padé approximation. By modifying this block, a higher order approximation can easily be used. The complete control diagram of the controller is depicted in Fig. 5.4.

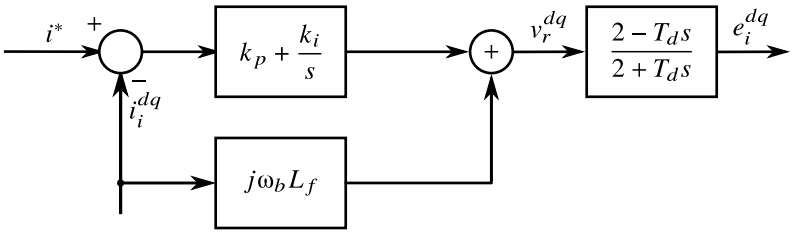

Figure 5.4: Block diagram of the PI regulator and equivalent delay (PI + delay) of the digital control and modulation.

The following state variables X_{Inv} are identified (the integrator Δx_i^{dq} and the delay model Δx_d^{dq}), as well as the inputs U_{Inv} and outputs Y_{Inv} of this block:

$$\begin{aligned} X_{Inv} &= \left[\Delta x_i^d, \Delta x_i^q, \Delta x_d^d, \Delta x_d^q\right]'_{4\times1} \\ U_{Inv} &= \left[\Delta i_d^*, \Delta i_q^*, \Delta i_i^d, \Delta i_i^q\right]'_{4\times1} \\ Y_{Inv} &= \left[\Delta e_i^d, \Delta e_i^q\right]'_{2\times1} \end{aligned} \tag{5.18}$$

The state-space matrices of this block are $A_{Inv}, B_{Inv}, C_{Inv}, D_{Inv}$, describing the following set of equations:

$$\begin{aligned} v_r^d &= k_p\left(i_d^* - i_i^d\right) + x_i^d + \omega_0 L_f i_i^q \\ v_r^q &= k_p\left(i_q^* - i_i^q\right) + x_i^q - \omega_0 L_f i_i^d \\ \frac{dx_i^d}{dt} &= k_i\left(i_d^* - i_i^d\right) \\ \frac{dx_i^q}{dt} &= k_i\left(i_q^* - i_i^q\right) \\ \frac{dx_d^d}{dt} &= -\frac{2}{T_d}x_d^d + \frac{4}{T_d}v_r^d \\ \frac{dx_d^q}{dt} &= -\frac{2}{T_d}x_d^q + \frac{4}{T_d}v_r^q \end{aligned} \tag{5.19}$$

with the following outputs:

$$\begin{aligned} e_i^d &= -x_i^d + x_d^d - k_p i_d^* + k_p i_i^d - \omega_0 L_f i_i^q \\ e_i^q &= -x_i^q + x_d^q - k_p i_q^* + \omega_0 L_f i_i^d + k_p i_i^q \end{aligned} \tag{5.20}$$

The complete expressions of the matrices of the controller are available in Appendix B.

S-VSC Electromagnetic Equations

The electrical and magnetic equations of both virtual stator and rotor of the S-SVC were presented in Chapter 3. The block state variables X_{Elt}, inputs U_{Elt} and outputs Y_{Elt} are defined as:

$$\begin{aligned} X_{Elt} &= \left[\Delta\lambda_d, \Delta\lambda_q, \Delta\lambda_{rq}\right]'_{3\times1} \\ U_{Elt} &= \left[\Delta v_g^d, \Delta v_g^q, \Delta\omega_r, \Delta\lambda_e\right]'_{4\times1} \\ Y_{Elt} &= \left[\Delta i_v^d, \Delta i_v^q\right]'_{2\times1} \end{aligned} \tag{5.21}$$

The state-space matrices $A_{Elt}, B_{Elt}, C_{Elt}, D_{Elt}$ of this block are obtained from the linearization of the electromagnetic equations of the S-VSC, summarized here:

$$\begin{aligned} v_d &= -R_s i_{vd} - \omega_r\lambda_q + \frac{1}{\omega_b}\frac{d\lambda_d}{dt} \\ v_q &= -R_s i_{vq} + \omega_r\lambda_d + \frac{1}{\omega_b}\frac{d\lambda_q}{dt} \\ \tau_{rq0}\frac{d\lambda_{rq}}{dt} &= -\lambda_{rq} - L_{rq} i_{vq} \\ i_{vd} &= \frac{\lambda_e - \lambda_d}{L_s} \\ i_{vq} &= \frac{\lambda_{rq} - \lambda_q}{L_s} \end{aligned} \tag{5.22}$$

which are linearized as:

$$\begin{aligned} \Delta v_{gd} &= -R_s\Delta i_{vd} + \frac{1}{\omega_b}\frac{d\Delta\lambda_d}{dt} - \omega_0\Delta\lambda_q - \Lambda_{q0}\Delta\omega \\ \Delta v_{gq} &= -R_s\Delta i_{vq} + \frac{1}{\omega_b}\frac{d\Delta\lambda_q}{dt} + \omega_0\Delta\lambda_d + \Lambda_{d0}\Delta\omega \\ \tau_{rq0}\frac{d\Delta\lambda_{rq}}{dt} &= -\Delta\lambda_{rq} - L_{rq}\Delta i_{vq} \\ \Delta i_{vd} &= \frac{\Delta\lambda_e - \Delta\lambda_d}{L_s} \\ \Delta i_{vq} &= \frac{\Delta\lambda_{rq} - \Delta\lambda_q}{L_s} \end{aligned} \tag{5.23}$$

The state variables derivatives can be highlighted:

$$\begin{aligned}
\frac{d\Delta\lambda_d}{dt} &= -\omega_b\frac{R_s}{L_s}\Delta\lambda_d + \omega_0\cdot\omega_b\Delta\lambda_q + \omega_b\Delta v_{gd} + \omega_b\Lambda_{q0}\Delta\omega + \omega_b\frac{R_s}{L_s}\Delta\lambda_e \\
\frac{d\Delta\lambda_q}{dt} &= -\omega_0\cdot\omega_b\Delta\lambda_d - \omega_b\frac{R_s}{L_s}\Delta\lambda_q + \omega_b\frac{R_s}{L_s}\Delta\lambda_{rq} + \omega_b\Delta v_{gq} - \omega_b\Lambda_{d0}\Delta\omega \\
\frac{d\Delta\lambda_{rq}}{dt} &= \frac{L_{rq}}{\tau_{rq0}L_s}\Delta\lambda_q - \frac{1+L_{rq}/L_s}{\tau_{rq0}}\Delta\lambda_{rq}
\end{aligned} \tag{5.24}$$

The outputs are simply:

$$\begin{aligned}
\Delta i_{vd} &= \frac{\Delta\lambda_e - \Delta\lambda_d}{L_s} \\
\Delta i_{vq} &= \frac{\Delta\lambda_{rq} - \Delta\lambda_q}{L_s}
\end{aligned} \tag{5.25}$$

The complete expressions of the matrices of the S-VSC electromagnetic part are available in Appendix B.

S-VSC Power Loops Equations

The swing equation (active power loop) and the excitation control (reactive power control) equations of the S-SVC are described by this block. Its state variables X_{Power}, inputs U_{Power} and outputs Y_{Power} are as follows:

$$\begin{aligned}
X_{Power} &= [\Delta\omega, \Delta\delta, \Delta\lambda_e]'_{3\times1} \\
U_{Power} &= \left[\Delta v_g^d, \Delta v_g^q, \Delta i_v^d, \Delta i_v^q, \Delta\omega_g\right]'_{5\times1} \\
Y_{Power} &= [\Delta P_v, \Delta Q_v, \Delta\omega_r, \Delta\delta, \Delta\lambda_e]'_{5\times1}
\end{aligned} \tag{5.26}$$

The state-space matrices $A_{Power}, B_{Power}, C_{Power}, D_{Power}$ of the power loops block are again obtained by the linearizing the relative equations:

$$\begin{aligned}
-P_v &= 2H\frac{d\omega_r}{dt} \\
\frac{d\delta}{dt} &= \left(\omega_r - \omega_g\right)\omega_b \\
-k_e\frac{Q_v}{V_g} &= \frac{d\lambda_e}{dt}
\end{aligned} \tag{5.27}$$

The state variables derivatives can be highlighted:

$$\begin{aligned}
\frac{d\Delta\omega}{dt} &= \frac{b_p}{2H}\Delta P^* - \frac{I_{vd0}}{2H}\Delta v_{gd} - \frac{I_{vq0}}{2H}\Delta v_{gq} - \frac{V_{gd0}}{2H}\Delta i_{vd} - \frac{V_{gq0}}{2H}\Delta i_{vq} \\
\frac{d\Delta\delta}{dt} &= \omega_b\Delta\omega_r - \omega_b\Delta\omega_g \\
\frac{d\Delta\lambda_e}{dt} &= k_e\frac{b_q}{V_{g0}}\Delta Q^* + k_e\frac{I_{vq0}}{V_{g0}}\Delta v_{gd} - k_e\frac{I_{vd0}}{V_{g0}}\Delta v_{gq} - k_e\frac{V_{gq0}}{V_{g0}}\Delta i_{vd} + k_e\frac{V_{gd0}}{V_{g0}}\Delta i_{vq}
\end{aligned} \tag{5.28}$$

The complete expressions of these matrices are available in Appendix B.

5.3.4 Algebraic Components Definition

Power Reference Calculation

The power reference computation algebraic block performs the following calculation to obtain the current references i^*_{set} starting from the external power references PQ^*, the S-VSC currents i_v and the grid voltage v_g^{dq}:

$$i^*_{set,d} + ji^*_{set,q} = \frac{P^*_t - jQ^*_t}{v^d_g - jv^q_g} \tag{5.29}$$

where:

$$\begin{aligned}
P^*_t &= P^* + P_v \\
Q^*_t &= Q^* + Q_v
\end{aligned} \tag{5.30}$$

Due to the division involved in (5.29), a dedicated block is justified to simplify the modeling process.

There are no state variables, while the inputs U_{Ref} and outputs Y_{Ref} of the block are:

$$\begin{aligned}
U_{Ref} &= \left[\Delta P^*, \Delta Q^*, \Delta P_v, \Delta Q_v, \Delta v^d_g, \Delta v^q_g\right]'_{6\times1} \\
Y_{Ref} &= \left[\Delta i^*_d, \Delta i^*_q\right]'_{2\times1}
\end{aligned} \tag{5.31}$$

Equation (5.29) is linearized, obtaining:

$$\Delta i_d^* = \frac{v_{gd0}}{V_{g0}^2} + \frac{v_{gq0}}{V_{g0}^2} + \frac{v_{gd0}}{V_{g0}^2} + \frac{v_{gq0}}{V_{g0}^2} + \frac{v_{gd0}}{V_{g0}^2} + \frac{v_{gq0}}{V_{g0}^2} + \frac{P_{t0}^*(v_{gq0}^2 - v_{gd0}^2) - 2Q_{t0}^* v_{gd0} v_{gq0}}{V_{g0}^4} + \frac{Q_{t0}^*(v_{gd0}^2 - v_{gq0}^2) - 2P_{t0}^* v_{gd0} v_{gq0}}{V_{g0}^4}$$

$$\Delta i_q^* = \frac{v_{gq0}}{V_{g0}^2} - \frac{v_{gd0}}{V_{g0}^2} + \frac{v_{gq0}}{V_{g0}^2} - \frac{v_{gd0}}{V_{g0}^2} + \frac{v_{gq0}}{V_{g0}^2} - \frac{v_{gd0}}{V_{g0}^2} - \frac{2P_{t0}^* v_{gd0} v_{gq0} + Q_{t0}^*(v_{gq0}^2 - v_{gd0}^2)}{V_{g0}^4} + \frac{P_{t0}^*(v_{gd0}^2 - v_{gq0}^2) + 2Q_{t0}^* v_{gd0} v_{gq0}}{V_{g0}^4}$$

Being an algebraic block, only the D_{Ref} matrix is obtained and it is available in Appendix B.

Grid Perturbations

This second algebraic block models the connection to the electric grid. It generates the grid voltage variations e_g^{dq} according to the global system inputs $\Delta\omega_g, \Delta E_g, \Delta\phi_g$, which represent the grid perturbations.

The grid voltage vector is defined as:

$$e_g^{dq} = E_g e^{-j\left(\frac{\pi}{2} - \delta\right)} \tag{5.32}$$

Any phase jump $\Delta\phi_g$ in the grid voltage vector leads to the variation of the S-VSC load angle δ. As already presented in the previous power loops section, a grid frequency $\Delta\omega_g$ variation leads to a load angle variation and it must be therefore included in (5.27). In Fig. 5.5, the vector diagram of the grid and S-VSC is depicted, as well as the graphical representation of the angle variation due to a phase jump in the grid.

Before the perturbation in the grid (time $t = t_0^-$), the angles of the grid and the S-VSC are as follows:

$$\begin{aligned} \theta_r\left(t_0^-\right) &= \theta_0 \\ \theta_g\left(t_0^-\right) &= \theta_{g0}^- \\ \delta\left(t_0^-\right) &= \frac{\pi}{2} + \theta_0 - \theta_{g0}^- = \delta_0 \end{aligned} \tag{5.33}$$

The S-VSC is assumed locked to the grid, so the virtual speeds are:

$$\begin{aligned} \omega\left(t_0^-\right) &= \omega_0 \cdot \omega_b \\ \omega_g\left(t_0^-\right) &= \omega_0 \cdot \omega_b \\ \omega\left(t_0^-\right) - \omega_g\left(t_0^-\right) &= 0 \end{aligned} \tag{5.34}$$

After the perturbation $(\Delta E_g, \Delta\phi_g)$ the angles vary according to:

$$\begin{aligned} \theta_r\left(t_0^+\right) &= \theta_0 \\ \theta_{g0}\left(t_0^+\right) &= \theta_{g0}^- + \Delta\phi_g \\ \delta\left(t_0^+\right) &= \frac{\pi}{2} + \theta_0 - \theta_{g0}^+ = \delta_0 - \Delta\phi_g \end{aligned} \tag{5.35}$$

The S-VSC rotor position θ_r is a state variable and does not change instantaneously. The angle variations are as follows:

$$\begin{aligned} \frac{d\theta_r}{dt} &= \omega_r \cdot \omega_b \\ \frac{d\theta_g}{dt} &= \omega_g \cdot \omega_b \\ \frac{d\delta}{dt} &= \left(\omega - \omega_g\right)\omega_b \end{aligned} \tag{5.36}$$

Therefore, this block generates the output Y_{Grid} (i.e. the grid voltage Δe_g^{dq}) depending on the following inputs U_{Grid}:

$$\begin{aligned} U_{Grid} &= \left[\Delta\delta, \Delta E_g, \Delta\phi_g\right]'_{3\times1} \\ Y_{Grid} &= \left[\Delta e_g^d, \Delta e_g^q\right]'_{2\times1} \end{aligned} \tag{5.37}$$

and from the matrix D_{Grid}, obtained by linearizing (5.32).

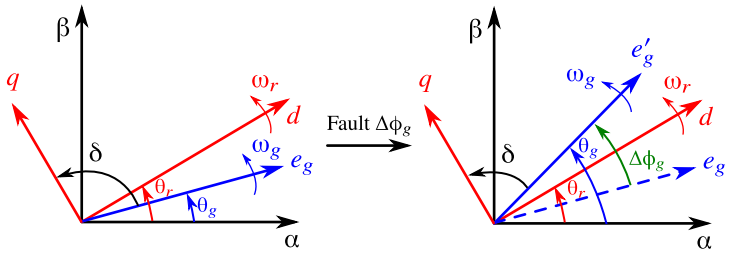

Figure 5.5: Vector diagram of the grid voltage and the (d,q) S-VSC rotating reference frames. The angle $\Delta\phi_g$ is defined as the load angle variation after a fault event.

5.3.5 Aggregated Model

After having defined every dynamic and algebraic blocks, the aggregated model can be obtained. First, it is necessary to list the aggregated state variables X_s, inputs U and outputs Y:

$$\begin{aligned} X_s &= [X_{LCL}, X_{Inv}, X_{Elt}, X_{Power}]'_{16\times1} \\ U &= \left[U_{LCL}, U_{Inv}, U_{Elt}, U_{Power}, U_{Ref}, U_{Grid}\right]'_{27\times1} \\ Y &= \left[Y_{LCL}, Y_{Inv}, Y_{Elt}, Y_{Power}, Y_{Ref}, Y_{Grid}\right]'_{19\times1} \end{aligned} \tag{5.38}$$

Then, the aggregated model matrices, which are as follows:

$$\begin{aligned} A_a &= \begin{bmatrix} A_{LCL} & 0 & 0 & 0 \\ 0 & A_{Inv} & 0 & 0 \\ 0 & 0 & A_{Elt} & 0 \\ 0 & 0 & 0 & A_{Power} \end{bmatrix}_{16\times16} \\ B_a &= \begin{bmatrix} B_{LCL} & 0 & 0 & 0 & \dots & 0 \\ 0 & B_{Inv} & 0 & 0 & \dots & 0 \\ 0 & 0 & B_{Elt} & 0 & \dots & 0 \\ 0 & 0 & 0 & B_{Power} & \dots & 0 \end{bmatrix}_{16\times27} \\ C_a &= \begin{bmatrix} C_{LCL} & 0 & 0 & 0 \\ 0 & C_{Inv} & 0 & 0 \\ 0 & 0 & C_{Elt} & 0 \\ 0 & 0 & 0 & C_{Power} \\ \vdots & \vdots & \vdots & \vdots \\ 0 & 0 & 0 & 0 \end{bmatrix}_{19\times16} \\ D_a &= \begin{bmatrix} D_{LCL} & 0 & 0 & 0 & 0 & 0 \\ 0 & D_{Inv} & 0 & 0 & 0 & 0 \\ 0 & 0 & D_{Elt} & 0 & 0 & 0 \\ 0 & 0 & 0 & D_{Power} & 0 & 0 \\ 0 & 0 & 0 & 0 & D_{Ref} & 0 \\ 0 & 0 & 0 & 0 & 0 & D_{Grid} \end{bmatrix}_{19\times29}. \end{aligned} \tag{5.39}$$

It must be noted that the matrices B_a and C_a are extended with a number of null elements equal to the number of inputs (8 in total) and outputs (4 in total) of the two algebraic blocks.

5.3.6 Connection Matrices

The last step is represented by the connection matrices T. They are obtained by connecting the inputs U and the outputs Y of the aggregated system to the global system inputs U_s and outputs Y_s. The matrix T_{ss} is zero, as there is no direct feed-through from the system inputs to the system outputs. The detailed expressions of the connection matrices are available in Appendix B.

$$\begin{matrix} T_{uy_{27\times19}} & T_{us_{27\times5}} \\ T_{sy_{6\times19}} & T_{ss_{6\times5}} = 0_{6\times5} \end{matrix} \tag{5.40}$$

5.3.7 Derivation of the Global State Space Model

After having obtained all the necessary matrices, by applying (5.8), the final global state-space system representation (matrices A_s, B_s, C_s, D_s) is obtained. The state-space model is now ready for the analysis and the simulation. Such model could have been also obtained following a monolithic way. However, thanks to CCM, the modeling phase can be tackled more easily and quick and straightforward modifications are possible, in case either the controller or the physical system change. A practical and straightforward example of this advantage is changing the current feedback of the current controller. In fact, for grid-connected converters interfaced with LCL filters to the grid, two types of current feedbacks are usually adopted: grid side current feedback and converter side current feedback [5].

In the case of the S-VSC, the converter side current feedback is adopted. Therefore, the outputs of the LCL filter block Y_{LCL} include the converter side current and not the grid side currents. In case the control strategy is modified and the current feedback is shifted to the grid side current, then, only the Y_{LCL} vector and the relative matrices C_{LCL} and D_{LCL} must be altered. Every other component remains the same. Moreover, the interconnection matrices are kept constant as well, being the two feedbacks equivalent from the point of view of signal routing.

Another example of the easiness of reconfiguration by adding new blocks is the addition of an external droop controller. If the plant is required a primary frequency regulation, then an extra proportional frequency controller can added, generating the necessary active power references for the inner control. Thanks to the adopted CCM, the S-VSC model is not modified, but a simple extra algebraic block is included before the reference calculation block. This extra component will receive as inputs the nominal and the actual grid frequency and generate the active droop power reference, which is then added to the external power references of the converter.

5.4 S-VSC State-Space Model Discussion and Validation

After having derived the S-VSC in state-space form, it is possible to numerically calculate the poles λ of the S-VSC, by solving:

$$det(A_s - \lambda I) = 0 \tag{5.41}$$

The result is displayed as pole map in Fig. 5.6 and they are also listed in Table 5.1. The parameters of the system have been chosen according to the experimental setup used for later validation and are available in Table 5.2. The usual comments about the stability and damping of the system can be stated. Moreover, the pole map representation helps visually distinguishing the poles of the system as follows:

- The high frequency poles (1 - 4), related to the LCL filter (in the range of 2 kHz);
- The equivalent poles of the digital control (5 - 8, 11, 12);
- The poles (9, 10) of the virtual stator of the S-VSC and the grid (50 Hz);
- The low frequency poles (13 - 16) of the electromechanical part of the S-VSC (i.e., excitation control, damper winding and swing equation) in the range of 1 Hz.

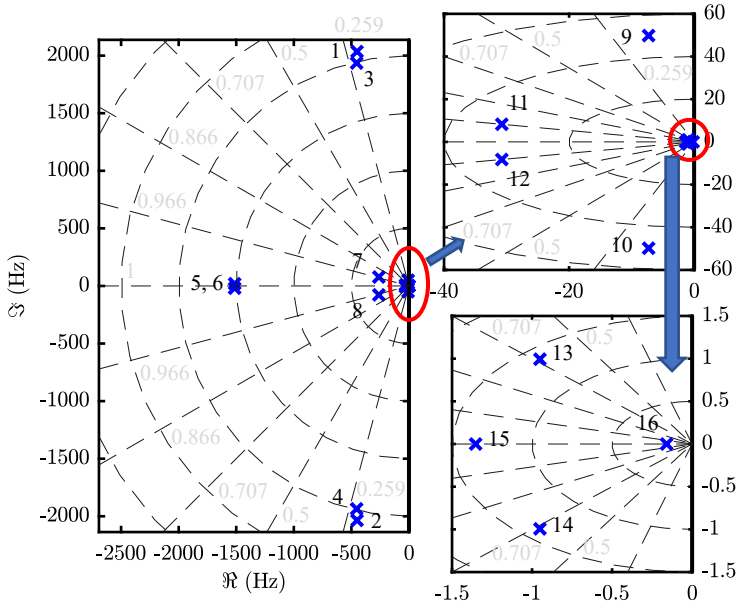

Figure 5.6: Pole map of the S-SVC. The poles are numbered according to Table 5.1.

Then, the analysis of the participation factors [2] can be done, in order to clearly define which state variables influence the single poles. The participation factor p_{ik} of the k-th state to the i-th mode is defined as:

$$p_{ik} = \Phi_{ik} \cdot \Psi_{ki} \tag{5.42}$$

where Φ_{ik} is the k-th value of the right eigenvector Φ_i and Ψ_{ki} is the k-th value of the left eigenvector Ψ_i.

Table 5.1 shows the results from (5.42), correlating the states and the modes of the system. Thanks to this analysis, the poles of the system can be linked to the physical quantities that influence them.

Table 5.1: Poles and participation factors. Only significant factors are displayed (larger than 0.1)

Poles	1-2	3-4	5-6	7-8	9-10	11-12	13-14	15	16
f_0 (Hz)	2084.58	1988.07	1513.86	272.92	50.34	31.85	1.38	1.35	0.16
τ (ms)	0.35	0.35	0.11	0.61	21.87	5.17	167.39	117.67	999.67
ζ	0.216	0.229	~1	0.959	0.145	0.966	0.691	–	–
i_{id}	0.2065	0.2079	0.1532	0.2639	–	–	–	–	–
i_{iq}	0.2065	0.2079	0.1532	0.2609	–	–	–	–	–
i_{gd}	–	–	–	–	0.2740	–	–	–	–
i_{gq}	–	–	–	–	0.2810	–	–	–	–
v_{gd}	0.2471	0.2475	–	–	–	–	–	–	–
v_{gq}	0.2471	0.2474	–	–	–	–	–	–	–
x_{id}	–	–	–	–	–	0.5750	–	–	–
x_{iq}	–	–	–	–	–	0.5759	–	–	–
x_{pd}	–	–	0.6859	0.1876	–	–	–	–	–
x_{pq}	–	–	0.6863	0.1875	–	–	–	–	–
λ_d	–	–	–	0.4200	0.2282	–	–	–	–
λ_q	–	–	–	0.4178	0.2199	–	–	–	–
λ_{rq}	–	–	–	–	–	–	2.2608	5.5357	–
ω_r	–	–	–	–	–	–	1.6308	-2.2624	–
δ	–	–	–	–	–	–	1.6362	-2.2699	–
λ_e	–	–	–	–	–	–	–	–	1.0002

This preliminary analysis is useful from the point of view of a multi-timescale study. In fact, the poles whose time constants are too small or too large can be excluded to simplify the model. An example related to the considered case study is the simplification of the model to analyze the low frequency behavior of the system (e.g., inertial behavior of a power system during a frequency drop), by neglecting the high frequency poles, related to the LCL filter and the current controller. Since these poles are orders of magnitude faster than the electromechanical dynamics of the S-VSC, they can be approximated with a direct feed-through with no dynamics. The individual blocks and their interconnections can be easily rearranged to obtain the needed simplified model.

Table 5.2: Inverter and S-VSC parameters for the state-space model and of the experimental setup

Parameter	**Value**	**Parameter**	**Value**
V_b	$230\sqrt{2}$ V	S_b	15 kVA
L_f	2 mH	C_f	5 µF
L_{fg}	1 mH	L_g	3 mH
k_p	3.77 Ω	k_i	710.6 Ω/s
L_s	0.1 pu	R_s	0.02 pu
H	4 s	k_e	0.22
L_{rq}	1.048 pu	τ_{rq0}	0.278 s
$f_s = f_{sw}$	10 kHz	V_{DC}	700 V

Besides, a change of the parameters of the system can be studied wit the state-space model. The variation of the Short Circuit Ratio (SCR) of the connection to the grid is a useful example. This analysis can be especially important for wind power applications connected to very weak grids. Due to the often isolated geographical positions, long cables or overhead lines, SCR ranging down to 1.5 or even less have been reported [119].

The SCR of the system is swept from 10 to 1.5 and the resulting pole map is shown in Fig. 5.7. The S-SVC damper and excitation control parameters are tuned according to the modified grid impedance. As it can be seen from the pole map, the poles of the LCL filter (1 - 4) change their frequency, as the grid side inductance is modified. The S-VSC stator poles (9, 10) are also influenced, being the stator in an equivalent series connection with the grid inductance. The effect is a lower damping of such poles, that can be however compensated by increasing the virtual stator resistance R_s. Finally, the low frequency mechanical poles (13 - 15) do not alter significantly their damping, thanks to the tuning algorithm described Chapter 3, but only change their natural frequency. The excitation control pole (16) is not modified, as it is tuned as described in Chapter 3 to always guarantee the desired time constant.

In addition to the presented analysis, the state-space model can be used for other studies. For example, the pole map can be obtained for different operating points (i.e. operation under load), or the pole variation due to the parametric uncertainty of the physical components (i.e. grid inductance estimation, filter parameters) on the tuning procedure of both the controllers and the S-VSC.

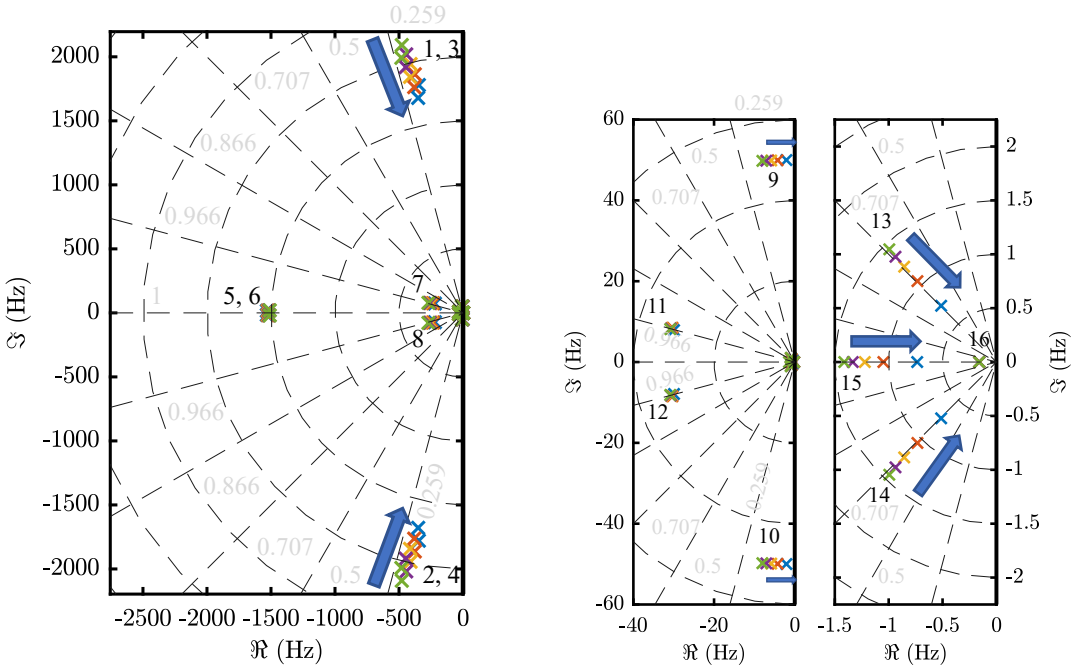

(a) (b)

Figure 5.7: Pole map of the S-SVC when the SCR changes from 10 to 1.5. The arrows indicate a decrease in the SCR. The poles are numbered according to Table 5.1. From left to right:
a) Complete pole map;
b) Magnifications of the lower frequency poles.

5.4.1 Experimental Validation

The obtained state-space model was then verified experimentally. In this case, the S-VSC has been implemented on a dSPACE 1007, controlling a 15 kVA three-phase inverter connected to a grid emulator, as shown in Fig. 5.8. The digital control is executed at f_s = 10 kHz, which also corresponds to the switching frequency f_{sw} of the converter.

The parameters of both the experimental setup and the S-VSC are listed in Table 5.2.

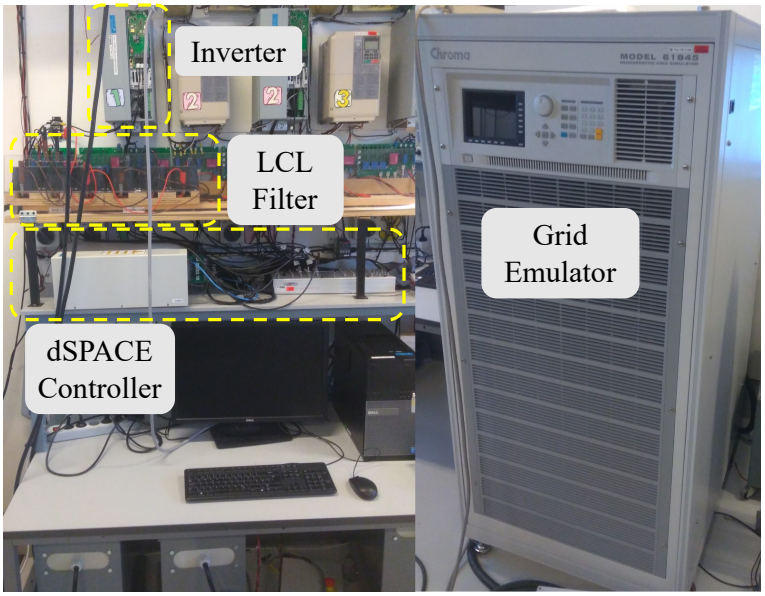

Figure 5.8: Experimental setup where the controller is based on dSPACE.

The state-space model has been validated performing tests using all the five available inputs ΔP^*_{ext}, ΔQ^*_{ext}, $\Delta\omega_g$, ΔE_g and $\Delta\phi_g$:

1. Step active power reference variation ΔP^*_{ext};
2. Step reactive power reference variation ΔQ^*_{ext};
3. Step drop of Grid frequency $\Delta\omega_g$;
4. Grid voltage drop ΔE_g with phase jump $\Delta\phi_g$.

The active power flow into the grid and the frequency of the S-VSC are compared with the outputs of the state-space model in the first test (Fig. 5.9). The active power reference rises from 0.2 pu to 0.3 pu at $t = 0.2$ s. The choice of the power levels have been chosen in order to perform a more general test of the state-space model. In fact, the current reference calculation block strongly depends on the initial active and reactive power references P^*_0 and Q^*_0. Therefore, a non zero initial active power operating point has been chosen, better to validate this aspect of the model. As it can be seen from Fig. 5.9 both the S-VSC virtual speed ω_r and the mean values of the injected active power are consistent to the results from the state-space model. The state space-model, in fact, describes the moving average behavior of the system and does not take into account the switching behavior of the converter and the non-ideal measurement process (e.g. noise, delays), which on the other hand affect the experimental setup.

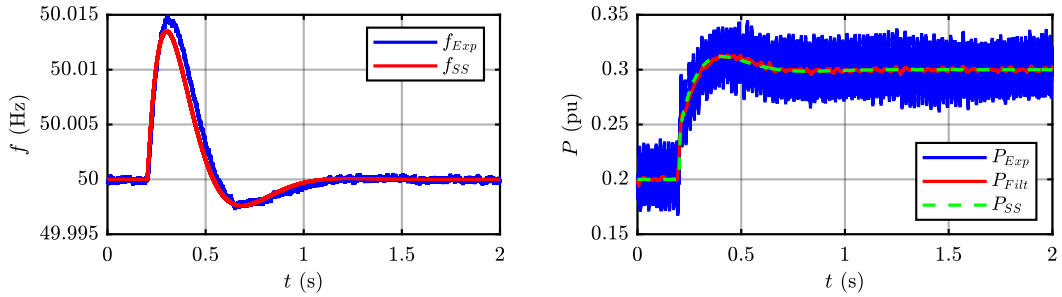

(a) (b)

Figure 5.9: Test 1: Step in active power reference ΔP^*_{ext} from 0.2 pu to 0.3 pu.
From left to right:
a) S-VSC virtual rotor speed (Hz) from experimental test (Exp) and state-space model (SS);
b) Active power injected from the inverter (pu) from experimental test (Exp), filtered active power (Filt) and output of the state-space model (SS).

In the second test (Fig. 5.10), the reactive power injection is validated. In this test, the reactive power reference rises from 0.1 pu to 0.2 pu. Similarly to the previous Test, the initial non-zero operating point has been chosen better to test the current reference calculation block of the model. Also in this case, the state-space model of the S-VSC is accurate enough to simulate the step transient of the reactive power reference. Again, the state-space model does not include the switching and non-ideal behavior of the experimental setup. This non-ideal behavior can be neglected when dealing with longer timescales, such as in Test 2. In fact, these aspects act with much shorter time constants and do not significantly affect the behavior during these transients (operating in the time scale of seconds).

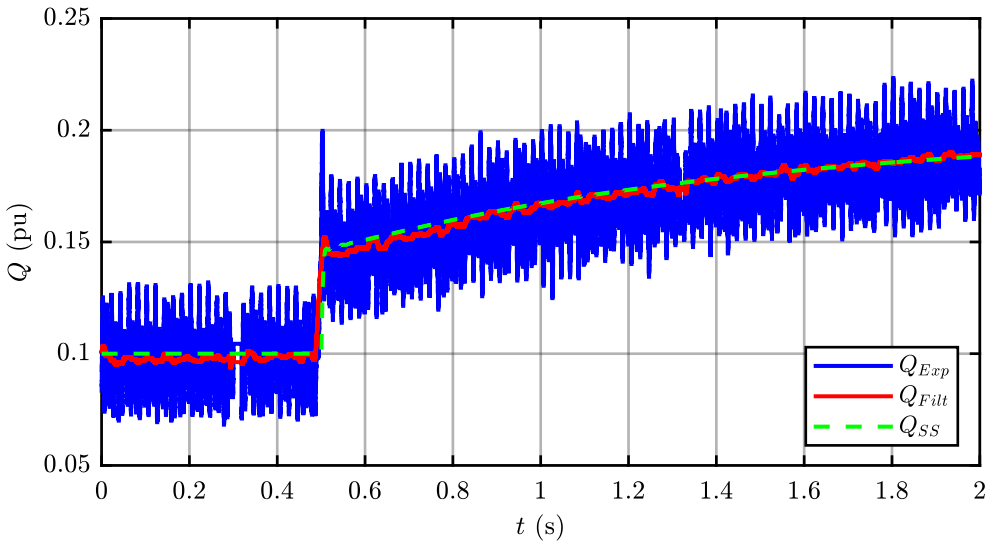

Figure 5.10: Test 2: Reactive power reference ΔQ^*_{ext} step from 0.1 pu to 0.2 pu. Reactive power injected from the inverter (pu) from experimental test (exp), filtered reactive power (Filt) and output of the state-space model (SS).

The third test (Fig. 5.11) validates the model against the input relative to the grid frequency variation $\Delta\omega_g$. A step frequency variation of -0.2 Hz has been applied by the grid emulator. The S-VSC compensates the grid frequency drop by injecting inertial active power into the grid. The state-space model is able to predict both the S-VSC frequency ω_r profile, as demonstrated in Fig. 5.11a, and the extent of active power injected, as shown in Fig. 5.11b. The frequency variations can be studied using the state-space model, as obtained here, for system level studies, when analyzing frequency regulation and inertial support in the power system. This kind of analysis can also help studying the different inertial action resulting from the tuning of the S-VSC (the parameters of interest are in this case the inertia constant H and the virtual damper parameters τ_{rq0} and L_{rq}, which are directly related to the electromechanical damping ζ of the virtual machine, as it was described in Chapter 3).

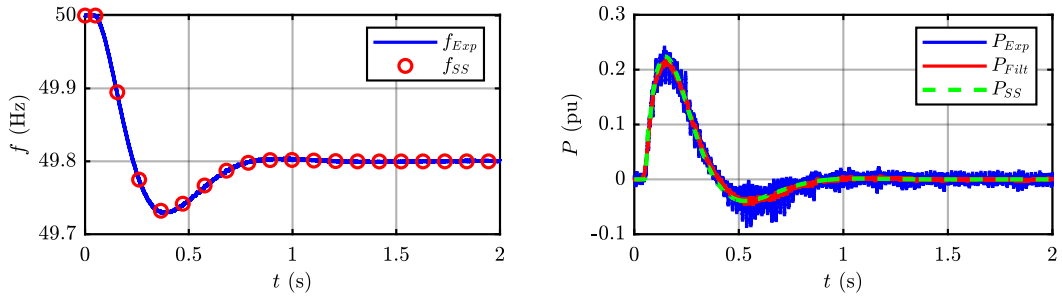

(a) (b)

Figure 5.11: Test 3: Grid frequency step drop $\Delta\omega_g$ from 50 Hz to 49.8 Hz.
From left to right:
a) S-VSC virtual rotor speed ω_r (Hz) from experimental test (Exp) and state-space model (SS);
b) Active power injected into the grid (pu) from experimental test (Exp), filtered active power (Filt) and output of the state-space model (SS).

Finally, the fourth test (Fig. 5.12) validates the state-space system in case of a realistic grid fault. The fault is emulated by stepping the grid voltage amplitude down to 95 % of its nominal value and applying a phase jump of $-5°$. In such tests, the quantities of interest are the reactive power injected into the grid (Fig. 5.12a), supporting the grid voltage, and the virtual excitation flux of the S-VSC λ_e (Fig. 5.12b) to evaluate the time constant of the excitation control. As expected, the state-space model predicts well both the trend and the amplitude of such quantities, therefore being a good analysis tool to study the S-VSC tuning and response.

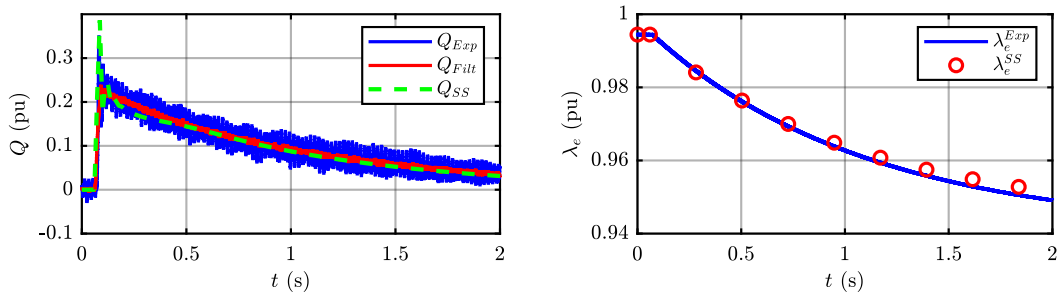

(a) (b)

Figure 5.12: Test 4: Grid voltage drop $\Delta E_g = -5$ % with phase jump $\Delta\phi_g = -5°$.
From left to right:
a) Reactive power injected into the grid (pu) from experimental test (Exp), filtered reactive power (Filt) and output of the state-space model (SS);
b) S-VSC virtual excitation flux λ_e from the experimental test (Exp) and state-space model (SS).

5.5 Conclusions and Summary of VSMs State-Space Modeling

In this chapter, **the CCM-based step-by-step algorithm to derive the state-space model of a grid-connected converter equipped with advanced cascaded controllers has been presented**. This modeling approach is suitable when tackling cascaded controllers with interconnected signals thanks to its modular structure. Moreover, it enables an easy modification or reconfiguration of the system, without fully remodeling it.

This method can be employed to obtain the state-space model of grid-tied inverters equipped with advanced cascaded controllers or emerging control techniques, such as the S-VSC with the goal of studying and simulating the stability of a power system with a high penetration of renewable energy sources. Besides, state-space models are practical in case of multi-timescale analysis of the power system: the eigenvalues of the system under study can be obtained, as well as their correlation to its state variables. Simplified models can, therefore, be obtained, by neglecting high or low frequency phenomena which are out of the scope of the analysis.

The state-space models obtained thanks to CCM represent a useful tool for both power electronics engineers and grid operators. The first can obtain preliminary information about the weak spots of the converters they are designing and test their behavior under different operating conditions (normal and abnormal). From the grid operator perspective, such state-space models could be provided by the manufacturers with different level of details [6, 7] and then be integrated in a more system-level analysis.

Chapter 6

Conclusions

6.1 Summary of the Thesis Contributions

This dissertation dealt with the analysis, implementation and validation of a new VSM model called Simplified Virtual Synchronous Compensator (S-VSC). This model operates as a parallel VSM structure, only providing ancillary services to the grid.

The main results of this research can be summarized as:

- The S-VSC model is intended as a plug-in controller for a traditional grid-feeding, current controlled inverter, as the majority of the RES converters and fast chargers. The advantage of this solution is the easy current limitation and the larger control bandwidth, compared to a voltage-controlled inverter.

- The S-VSC generates additive power contributions to the inverter references, to guarantee grid services (inertia emulation and compensation of current harmonics) and grid support during symmetrical and asymmetrical faults with reactive power only. In the literature, however, the virtual machines are always in charge of processing the full power references. Therefore the S-VSC always operates at low load, featuring higher transient stability and damping;

- Two damping methods are proposed (see 3.3): the RQ damping, using an equivalent q-axis damper winding and a Lead-lag damping, which is based on the filtering of the feedback active power. Both methods are providing an effecting electromechanical damping to the S-VSC and feature both a full damping-droop decoupling and reduced sensitivity to grid disturbances;

- A focus on the harmonic compensation capabilities of VSMs and their experimental assessment for the proposed S-VSC model;

- The extension of the CCM state-space modeling technique to study the S-VSC in system level integration.

During the PhD activity, a total of 18 papers were published. 6 of them about the emulation of SGs (2 journal and 4 conference papers). Moreover, three prizes were won for the research activity.

6.2 Future Developments

The following main future developments of this research are foreseeable at the moment:

- Further system level studies of the S-VSC, including its transient stability during faults and a comparison with traditional SGs and other VSM implementations;
- Integration strategies of the S-VSC in ultra fast charging stations, introducing local energy storage management logic;
- Black start and grid forming capabilities of the S-VSC, which has been studied for grid-connected application only so far;
- Fault current in case of asymmetrical faults and comparison with the existing strategies [5];
- S-VSC capable of injecting large short circuit currents during voltage dips (i.e., greater than 1 pu), thanks to hardware modifications.

Appendix A

List of Acronyms and Symbols

Δ Small Signal Variation

h Harmonic Order

j Imaginary Unit

s Laplace Operator

A.1 List of Acronyms

AVR Automatic Voltage Regulator

CCM Component Connection Method

CVSM Cascaded Virtual Synchronous Machine

EV Electric Vehicle

KHI Kawasaki Heavy Industries

MPPT Maximum Power Point Tracking

PCC Point of Common Coupling

PI Proportional Integral

PLC Power Loop Controller

PLL Phase Locked Loop

PV PhotoVoltaic

RES Renewable Energy Source

RoCoF Rate of Change of Frequency

SG Synchronous Generator

S-VSC Simplified Virtual Synchronous Compensator

SPC Synchronous Power Controller

THD Total Harmonic Distortion

TSO Transmission System Operator

UFC Ultra Fast Charger

VISMA VIrtual Synchronous MAchine

VSC Virtual Synchronous Compensator

VSM Virtual Synchronous Machine

VSG Virtual Synchronous Generator

A.2 List of Parameters

C_f LCL Filter Capacitance

D_p Droop-damping Gain

D_{PLL} PLL-damping Gain

D_q Voltage Droop Gain

f_n Nominal Grid Frequency

f_{BW}^i Bandwidth of the Current Controller

f_{sw} Converter Switching Frequency

H Inertia Constant

I_{max} Maximum Current

J Inertia of a Rotating Shaft

K Synchronverter Excitation Control Gain

k_{droop} Active Droop Gain

K_d VSYNC PLL Gain 1

k_d Proportional Term of the PI-based Damping

k_e Excitation Control Gain

k_{ff} Excitation Control Feed-forward Gain

k_g SPC-LL Droop Gain

k_H SPC-PI Integral Gain

k_h Integral Term of the PI-based Damping

K_i VSYNC PLL Gain 2

k_i Integral Gain

k_i^{PLL} PLL Integral Gain

k_p Proportional Gain

k_p^{PLL} PLL Proportional Gain

k_d Synchronizing Power

k_X SPC-PI Proportional Gain

L_f Converter Side LCL Filter Inductance

L_{fg} Grid Side LCL Filter Inductance

L_g Grid Equivalent Inductance

$\tilde{L}_g$ Estimated Grid Inductance

L_s Virtual Stator Inductance

L_d d-axis Self Inductance

L_q q-axis Self Inductance

L_D d-axis Damper Winding Self Inductance

L_Q q-axis Damper Winding Self Inductance

L_{rq} q-axis Simplified Damper Winding Self Inductance

L_{qt} Total q-axis Inductance of the S-VSC with RQ-based Damping

L_e Excitation Winding Self Inductance

L_t Transformer Inductance

M_{dD} d-axis Mutual Inductance (stator-damper)

M_{ed} d-axis Mutual Inductance (stator-excitation)

M_{eD} d-axis Mutual Inductance (excitation-damper)

M_{qQ} q-axis Mutual Inductance (stator-damper)

R_f Converter Side LCL Filter Resistance

R_{fg} Grid Side LCL Filter Resistance

R_g Grid Resistance

R_d LCL Filter Damping Resistance

R_s Virtual Stator Resistance

R_d d-axis Stator Resistance

R_q q-axis Stator Resistance

R_D d-axis Damper Winding Resistance

R_Q q-axis Damper Winding Resistance

R_{rq} q-axis Simplified Damper Winding Resistance

R_e Excitation Winding Resistance

R_D Active Droop Coefficient

P_{max} Maximum Transferable Active

S_b Base Power

T_{max} Maximum Torque

T_{min} Minimum Torque

V_b Base Voltage

X_g Grid Reactance

X_s Stator Reactance

X_{tot} Total Reactance

Z_q Total q-axis Impedance of the S-VSC with RQ-based Damping

ζ Damping factor

τ_d Active Droop Filter Time Constant

τ_e Excitation Control Time Constant

τ_{rq} q-axis Short Circuit Time Constant

τ_{rq0} q-axis Simplified Damper Winding Time Constant

τ_p Lead-lag Damping Pole Time Constant

τ_z Lead-lag Damping Zero Time Constant

ω_b Base Frequency

ω_n Nominal Grid Frequency

ω_{zi} Frequency of the Zero of the PI Current Controller

A.3 List of Variables

$\hat{E}$ Peak Value of the Virtual Back emf

g Equivalent Voltage Applied by the Modified Synchronverter

e Virtual Back emf

e_i^* Reference Voltage for the PWM Modulator

E_g Amplitude of the Thévenin Grid Voltage

e_g Thévenin Grid Voltage

i_i Converter Side Current

i_g Grid Side Current

i^* Reference Current, Limited

i^{ref} Reference Current, Non Limited

i_d d-axis Current

i_q q-axis Current

i_e Excitation Current

i_D d-axis Damper Winding Current

i_Q q-axis Damper Winding Current

i_{rq} q-axis Simplified Damper Winding Current

i_i^f Filtered Converter Side Current

i_v Virtual Current

$M_f i_f$ Excitation Flux Linkage of the Synchronverter

P_{ref} Reference Active Power from the PLL of the VSYNC

P_{set} Active Power Setpoint

P^* Active Power Reference

P_d Damping Power

P_e Electrical Active Power

P_i Active Power Injected by the Inverter

P_m Mechanical Power

P_v^* Virtual Active Power Reference

P_v Virtual Active Power

P_v^f Filtered Virtual Active Power

Q_{set} Reactive Power Setpoint

Q^* Reactive Power Reference

Q_d Voltage Droop Reactive Power Reference

Q_e Reactive Power

Q_e Reactive Power Injected by the Inverter

Q_m Mechanical Power

Q_v^* Virtual Reactive Power Reference

Q_v Virtual Reactive Power

T_d Damping Torque

T_e Electromagnetic Torque

T_m Mechanical Torque

v_{dc} dc-Link Voltage

v_c LCL Filter Capacitor Voltage

v_d d-axis Stator Voltage

v_q q-axis Stator Voltage

v_e Excitation Winding Voltage

v_g Measured Grid Voltage

v_{pcc} Voltage at the Point of Common Coupling

$\hat{v}$ CVSM Input Voltage of the Virtual Impedance

V_{set} Voltage Setpoint

$\hat{V}_g$ Peak Value of the Measured Grid Voltage

x_{LL} State Variable of the Lead-lag Filter of the S-VSC

δ Load Angle

θ_r Rotor Position

θ_g Grid Voltage Vector Position

λ_d d-axis Flux Linkage

λ_q q-axis Flux Linkage

λ_e Excitation Flux Linkage

λ_{ff} Feed-forward Excitation Flux Linkage

λ_D d-axis Damper Winding Flux Linkage

λ_Q q-axis Damper Winding Flux Linkage

λ_{rq} q-axis Simplified Damper Winding Flux Linkage

ϕ_g Phase Variation of the Grid Voltage

ω^* Reference Frequency

ω_g Actual Grid Frequency

ω_{PLL} PLL Measured Frequency

ω_r Rotor Frequency

$\dot{\omega}_r$ Rotor Frequency Derivative

Appendix B

State-Space Matrices of the S-VSC

B.1 LCL Filter

$$A_{LCL} =$$

$$\begin{bmatrix}
-\omega_b\frac{R_f+R_d}{L_i} & \omega_{r0}\omega_b & \omega_b\frac{R_d}{L_i} & 0 & -\frac{\omega_b}{L_i} & 0 \\
-\omega_{r0}\omega_b & -\omega_b\frac{R_f+R_d}{L_i} & 0 & \omega_b\frac{R_d}{L_i} & 0 & -\frac{\omega_b}{L_i} \\
\omega_b\frac{R_d}{L_{fg}+L_g} & 0 & -\omega_b\frac{R_{fg}+R_g+R_d}{L_{fg}+L_g} & \omega_{r0}\omega_b & \frac{\omega_b}{L_{fg}+L_g} & 0 \\
0 & \omega_b\frac{R_d}{L_{fg}+L_g} & -\omega_{r0}\omega_b & -\omega_b\frac{R_{fg}+R_g+R_d}{L_{fg}+L_g} & 0 & \frac{\omega_b}{L_{fg}+L_g} \\
\frac{\omega_b}{C_f} & 0 & -\frac{\omega_b}{C_f} & 0 & 0 & \omega_{r0}\omega_b \\
0 & \frac{\omega_b}{C_f} & 0 & -\frac{\omega_b}{C_f} & -\omega_{r0}\omega_b & 0
\end{bmatrix} \tag{B.1}$$

$$B_{LCL} =$$

$$\begin{bmatrix}
\frac{\omega_b}{L_i} & 0 & 0 & 0 & \omega_b I_{i0}^q \\
0 & \frac{\omega_b}{L_i} & 0 & 0 & -\omega_b I_{i0}^d \\
0 & 0 & -\frac{\omega_b}{L_{fg}+L_g} & 0 & \omega_b I_{g0}^q \\
0 & 0 & 0 & -\frac{\omega_b}{L_{fg}+L_g} & -\omega_b I_{g0}^d \\
0 & 0 & 0 & 0 & \omega_b V_{c0}^q \\
0 & 0 & 0 & 0 & -\omega_b V_{c0}^d
\end{bmatrix} \tag{B.2}$$

$$C_{LCL} =$$

$$\begin{bmatrix} 1 & 0 & 0 & 0 & 0 & 0 \\ 0 & 1 & 0 & 0 & 0 & 0 \\ R_d & 0 & -R_d & 0 & 1 & 0 \\ 0 & R_d & 0 & -R_d & 0 & 1 \\ \dfrac{L_g R_d}{L_{fg}+L_g} & 0 & \dfrac{R_g L_{fg} + R_{fg} L_g - L_g R_d}{L_{fg}+L_g} & 0 & \dfrac{L_g}{L_{fg}+L_g} & 0 \\ 0 & \dfrac{L_g R_d}{L_{fg}+L_g} & 0 & \dfrac{R_g L_{fg} + R_{fg} L_g - L_g R_d}{L_{fg}+L_g} & 0 & \dfrac{L_g}{L_{fg}+L_g} \end{bmatrix} \tag{B.3}$$

$$D_{LCL} =$$

$$\begin{bmatrix} 0 & 0 & 0 & 0 & 0 \\ 0 & 0 & 0 & 0 & 0 \\ 0 & 0 & 0 & 0 & 0 \\ 0 & 0 & 0 & 0 & 0 \\ 0 & 0 & \dfrac{L_{fg}}{L_{fg}+L_g} & 0 & 0 \\ 0 & 0 & 0 & \dfrac{L_{fg}}{L_{fg}+L_g} & 0 \end{bmatrix} \tag{B.4}$$

B.2 Digital Current Controller

$$A_{Inv} =$$

$$\begin{bmatrix} 0 & 0 & 0 & 0 \\ 0 & 0 & 0 & 0 \\ \dfrac{4}{T_d} & 0 & -\dfrac{2}{T_d} & 0 \\ 0 & \dfrac{4}{T_d} & 0 & -\dfrac{2}{T_d} \end{bmatrix} \tag{B.5}$$

$$B_{Inv} =$$

$$\begin{bmatrix} k_i & 0 & -k_i & 0 \\ 0 & k_i & 0 & -k_i \\ k_p \dfrac{4}{T_d} & 0 & -k_p \dfrac{4}{T_d} & \omega_{r0} L_i \dfrac{4}{T_d} \\ 0 & k_p \dfrac{4}{T_d} & -\omega_{r0} L_i \dfrac{4}{T_d} & -k_p \dfrac{4}{T_d} \end{bmatrix} \tag{B.6}$$

$$C_{Inv} =$$

$$\begin{bmatrix} -1 & 0 & 1 & 0 \\ 0 & -1 & 0 & 1 \end{bmatrix} \tag{B.7}$$

$$B_{Inv} = \begin{bmatrix} -k_p & 0 & k_p & -\omega_{r0} L_i \\ 0 & -k_p & \omega_{r0} L_i & k_p \end{bmatrix} \tag{B.8}$$

B.3 S-VSC Electromagnetic Part Matrices

$$A_{Elt} = \begin{bmatrix} -\omega_b \dfrac{R_s}{L_s} & \omega_{r0}\omega_b & 0 \\ -\omega_{r0}\omega_b & -\omega_b \dfrac{R_s}{L_s} & \omega_b \dfrac{R_s}{L_s} \\ 0 & \dfrac{L_{rq}}{\tau_{rq0} L_s} & -\dfrac{1 + L_{rq}/L_s}{\tau_{rq0}} \end{bmatrix} \tag{B.9}$$

$$B_{Elt} = \begin{bmatrix} \omega_b & 0 & \omega_b \Lambda_{q0} & \omega_b \dfrac{R_s}{L_s} \\ 0 & \omega_b & -\omega_b \Lambda_{d0} & 0 \\ 0 & 0 & 0 & 0 \end{bmatrix} \tag{B.10}$$

$$C_{Elt} = \begin{bmatrix} -\dfrac{1}{L_s} & 0 & 0 \\ 0 & -\dfrac{1}{L_s} & \dfrac{1}{L_s} \end{bmatrix} \tag{B.11}$$

$$D_{Elt} = \begin{bmatrix} 0 & 0 & 0 & \dfrac{1}{L_s} \\ 0 & 0 & 0 & 0 \end{bmatrix} \tag{B.12}$$

B.4 S-VSC Power Loops Matrices

$$A_{Power} = \begin{bmatrix} 0 & 0 & 0 \\ \omega_b & 0 & 0 \\ 0 & 0 & 0 \end{bmatrix} \tag{B.13}$$

$$B_{Power} = \begin{bmatrix} 0 & 0 & -\frac{I_{vd0}}{2H} & -\frac{I_{vq0}}{2H} & -\frac{V_{gd0}}{2H} & -\frac{V_{gq0}}{2H} & 0 \\ 0 & 0 & 0 & 0 & 0 & 0 & -\omega_b \\ 0 & 0 & k_e\frac{I_{vq0}}{V_{g0}} & -k_e\frac{I_{vd0}}{V_{g0}} & -k_e\frac{V_{gq0}}{V_{g0}} & k_e\frac{V_{gd0}}{V_{g0}} & 0 \end{bmatrix} \tag{B.14}$$

$$C_{Power} = \begin{bmatrix} 0 & 0 & 0 \\ 0 & 0 & 0 \\ 1 & 0 & 0 \\ 0 & 1 & 0 \\ 0 & 0 & 1 \end{bmatrix} \tag{B.15}$$

$$D_{Power} = \begin{bmatrix} 0 & 0 & I_{vd0} & I_{vq0} & V_{gd0} & V_{gq0} & 0 \\ 0 & 0 & -I_{vq0} & I_{vd0} & V_{gq0} & -V_{gd0} & 0 \\ 0 & 0 & 0 & 0 & 0 & 0 & 0 \\ 0 & 0 & 0 & 0 & 0 & 0 & 0 \\ 0 & 0 & 0 & 0 & 0 & 0 & 0 \end{bmatrix} \tag{B.16}$$

B.5 Current Reference Calculation

$$D_{Ref} = [D_1 \quad D_2] \tag{B.17}$$

$$D_1 = \begin{bmatrix} \frac{v_{gd0}}{V_{g0}^2} & \frac{v_{gq0}}{V_{g0}^2} & \frac{v_{gd0}}{V_{g0}^2} & \frac{v_{gq0}}{V_{g0}^2} \\ \frac{v_{gq0}}{V_{g0}^2} & -\frac{v_{gd0}}{V_{g0}^2} & \frac{v_{gq0}}{V_{g0}^2} & -\frac{v_{gd0}}{V_{g0}^2} \end{bmatrix} \tag{B.18}$$

$$D_2 = \begin{bmatrix} \frac{v_{gd0}}{V_{g0}^2} & \frac{v_{gq0}}{V_{g0}^2} & \frac{P_0^*(v_{gq0}^2 - v_{gd0}^2) - 2Q_0^* v_{gd0} v_{gq0}}{V_{g0}^4} & \frac{Q_0^*(v_{gd0}^2 - v_{gq0}^2) - 2P_0^* v_{gd0} v_{gq0}}{V_{g0}^4} \\ \frac{v_{gq0}}{V_{g0}^2} & -\frac{v_{gd0}}{V_{g0}^2} & -\frac{2P_0^* v_{gd0} v_{gq0} + Q_0^*(v_{gq0}^2 - v_{gd0}^2)}{V_{g0}^4} & \frac{P_0^*(v_{gd0}^2 - v_{gq0}^2) + 2Q_0^* v_{gd0} v_{gq0}}{V_{g0}^4} \end{bmatrix} \tag{B.19}$$

B.6 Grid Perturbation Matrices

$$D_{Grid} = \begin{bmatrix} e_{gq0} & \frac{e_{gd0}}{E_{g0}} & -e_{gq0} \\ -e_{gd0} & \frac{e_{gq0}}{E_{g0}} & e_{gd0} \end{bmatrix} \tag{B.20}$$

B.7 Connection Matrices

Only the non-zero elements are given:

$$\begin{aligned}
& T_{uy}(1,7)=1 \quad T_{uy}(2,8)=1 \quad T_{uy}(3,18)=1 \quad T_{uy}(4,19)=1 \quad T_{uy}(5,13)=1 \\
& T_{uy}(6,16)=1 \quad T_{uy}(7,17)=1 \quad T_{uy}(8,1)=1 \quad T_{uy}(9,2)=1 \quad T_{uy}(10,3)=1 \\
T_{uy_{27\times19}} \;:\; & T_{uy}(11,4)=1 \quad T_{uy}(12,13)=1 \quad T_{uy}(13,15)=1 \quad T_{uy}(14,3)=1 \quad T_{uy}(15,4)=1 \\
& T_{uy}(16,9)=1 \quad T_{uy}(17,10)=1 \quad T_{uy}(21,11)=1 \quad T_{uy}(22,12)=1 \quad T_{uy}(23,3)=1 \\
& T_{uy}(24,4)=1 \quad T_{uy}(25,14)=1 \\
T_{us_{27\times5}} \;:\; & T_{us}(18,3)=1 \quad T_{us}(19,1)=1 \quad T_{us}(20,2)=1 \quad T_{us}(26,4)=1 \quad T_{us}(27,5)=1 \\
& T_{sy}(1,1)=\frac{3}{2}V_{g0}^{d} \quad T_{sy}(1,3)=\frac{3}{2}I_{g0}^{d} \quad T_{sy}(1,2)=\frac{3}{2}V_{g0}^{q} \quad T_{sy}(1,4)=\frac{3}{2}I_{g0}^{q} \\
T_{sy_{6\times19}} \;:\; & T_{sy}(2,2)=\frac{3}{2}V_{g0}^{q} \quad T_{sy}(2,4)=\frac{3}{2}I_{g0}^{d} \quad T_{sy}(2,1)=-\frac{3}{2}V_{g0}^{d} \quad T_{sy}(2,3)=-\frac{3}{2}I_{g0}^{d} \\
& T_{sy}(3,13)=1 \quad T_{sy}(4,14)=1 \quad T_{sy}(5,3)=1 \quad T_{sy}(6,4)=1
\end{aligned} \tag{B.21}$$

Bibliography

[1] Aaron Wiener. "Germany's nuclear power phaseout turns off environmentalists". In: *Los Angeles Times* (Apr. 20, 2019). URL: https://www.latimes.com/world/la-xpm-2012-apr-20-la-fg-germany-nuclear-20120421-story.html (visited on 10/05/2020).

[2] Prabha Kundur. *Power System Stability and Control*. McGraw-Hill Education, Jan. 22, 1994. 1208 pp. ISBN: 978-0-07-035958-1.

[3] Pieter Tielens and Dirk Van Hertem. "The relevance of inertia in power systems". In: *Renewable and Sustainable Energy Reviews* 55 (Mar. 2016), pp. 999–1009. ISSN: 13640321. DOI: 10.1016/j.rser.2015.11.016.

[4] Australian Energy Market Operator (AEMO). *Power System Requirements*. July 2020.

[5] Remus Teodorescu, Marco Liserre, and Pedro Rodriguez. *Grid Converters for Photovoltaic and Wind Power Systems*. John Wiley & Sons, July 28, 2011. 455 pp. ISBN: 978-1-119-95720-1.

[6] Terna. *Terna Grid Code, Allegato A68 - CENTRALI FOTOVOLTAICHE - Condizioni generali di connessione alle reti AT Sistemi di protezione regolazione e controllo*. July 2018.

[7] Terna. *Terna Grid Code, Allegato A17 - CENTRALI EOLICHE - Condizioni generali di connessione alle reti AT Sistemi di protezione regolazione e controllo*. July 2018.

[8] VDE. *VDE-AR-N 4120 - Connection and Operation to High-Voltage Grid and their Operation*. 2018.

[9] *IEC 61400-21-1:2019 - Wind energy generation systems - Part 21-1: Measurement and assessment of electrical characteristics*. 2019.

[10] J. Fang et al. "On the Inertia of Future More-Electronics Power Systems". In: *IEEE Journal of Emerging and Selected Topics in Power Electronics* 7.4 (2019), pp. 2130–2146. ISSN: 2168-6777. DOI: 10.1109/JESTPE.2018.2877766.

[11] Australian Energy Market Operator (AEMO). *Analysis of the South Australian Blackout - 28 September 2016*. Mar. 2017.

[12] Australian Energy Market Operator (AEMO). *New South Wales and Victoria Separation Event on 4 January 2020*. Sept. 2020.

[13] *EN 50160 - Voltage characteristics of electricity supplied by public electricity networks*. 2010.

[14] Terna. *Terna Grid Code, Allegato A14 - Partecipazione alla regolazione di tensione*. May 2000.

[15] VDE. *VDE-AR-N 4110 - Connection and Operation to Medium-Voltage Grid*. 2018.

[16] VDE. *VDE-AR-N 4105 - Connection and Operation of Power Generating Plants to Low-Voltage Grid*. 2018.

[17] Mads Graungaard Taul et al. "Current Reference Generation based on Next Generation Grid Code Requirements of Grid-Tied Converters during Asymmetrical Faults". In: *IEEE Journal of Emerging and Selected Topics in Power Electronics* (2019), pp. 1–1. ISSN: 2168-6777, 2168-6785. DOI: 10.1109/JESTPE.2019.2931726.

[18] *IEC 61000-4-7:2002 - Electromagnetic compatibility (EMC) - Part 4-7: Testing and measurement techniques - General guide on harmonics and interharmonics measurements and instrumentation, for power supply systems and equipment connected thereto*. 2002.

[19] Marta Molinas. "Impedance-based Stability Evaluation of power electronics dominated power systems". IEEE PELS-IES Delhi Chapter Expert Lecture. Indian Institute of Technology Delhi and Delhi Technological University, New Delhi, India, 2019.

[20] C. Li. "Unstable Operation of Photovoltaic Inverter From Field Experiences". In: *IEEE Transactions on Power Delivery* 33.2 (Apr. 2018), pp. 1013–1015. ISSN: 0885-8977. DOI: 10.1109/TPWRD.2017.2656020.

[21] *IEC 61400-21-3:2019 - Wind energy generation systems - Part 21-3: Measurement and assessment of electrical characteristics - Wind turbine harmonic model and its application*. 2019.

[22] Robert Eriksson, Niklas Modig, and Katherine Elkington. "Synthetic inertia versus fast frequency response: a definition". In: *IET Renewable Power Generation* 12.5 (Apr. 9, 2018), pp. 507–514. ISSN: 1752-1416, 1752-1424. DOI: 10.1049/iet-rpg.2017.0370.

[23] H. Akagi. "Active Harmonic Filters". In: *Proceedings of the IEEE* 93.12 (Dec. 2005), pp. 2128–2141. ISSN: 0018-9219. DOI: 10.1109/JPROC.2005.859603.

[24] Solar Power Europe. *Global Market Outlook 2020-2024*. 2020.

[25] Global Wind Energy Council (GWEC). *Global Wind Report 2019*. 2019.

[26] IEA-PVPS. *Trends in PV applications 2019*. 2019.

[27] Business Insider. *Global Electric Vehicle Market Sales*. 2018.

[28] IEA. *Global EV Outlook 2020*. 2020.

[29] Erik Kirschbaum. "Germany to close all 84 of its coal-fired power plants, will rely primarily on renewable energy". In: *Los Angeles Times* (Jan. 26, 2019). URL: https://www.latimes.com/world/europe/la-fg-germany-coal-power-20190126-story.html (visited on 10/05/2020).

[30] Arbeitsgemeinschaft Energiebilanzen (AGEB). *Bruttostromerzeugung in Deutschland für 2016 bis 2018 (German Electrical Energy Generation 2016-2018)*. 2019.

[31] Yong Chen et al. "Comparison of methods for implementing virtual synchronous machine on inverters". In: International Conference on Renewable Energies and Power Quality (ICREPQ'12). Santiago de Compostela (Spain), Mar. 2012, pp. 755–759. DOI: 10.24084/repqj09.444.

[32] Qing-Chang Zhong and George Weiss. "Synchronverters: Inverters That Mimic Synchronous Generators". In: *IEEE Transactions on Industrial Electronics* 58.4 (Apr. 2011). Number: 4, pp. 1259–1267. ISSN: 0278-0046, 1557-9948. DOI: 10.1109/TIE.2010.2048839.

[33] George Weiss and Qing-Chang Zhong. "Static synchronous generators". Pat. WO2010055322A2. Ramot At Tel Aviv University Ltd Ulive Enterprises Limited. May 20, 2010.

[34] Qing-Chang Zhong et al. "Self-Synchronized Synchronverters: Inverters Without a Dedicated Synchronization Unit". In: *IEEE Transactions on Power Electronics* 29.2 (Feb. 2014). Number: 2, pp. 617–630. ISSN: 1941-0107. DOI: 10.1109/TPEL.2013.2258684.

[35] K. Sakimoto, Y. Miura, and T. Ise. "Stabilization of a power system with a distributed generator by a Virtual Synchronous Generator function". In: 8th International Conference on Power Electronics - ECCE Asia. May 2011, pp. 1498–1505. DOI: 10.1109/ICPE.2011.5944492.

[36] Toshinobu Shintai, Yuushi Miura, and Toshifumi Ise. "Reactive power control for load sharing with virtual synchronous generator control". In: Proceedings of The 7th International Power Electronics and Motion Control Conference. Vol. 2. June 2012, pp. 846–853. DOI: 10.1109/IPEMC.2012.6258956.

[37] Jia Liu, Yushi Miura, and Toshifumi Ise. "Comparison of Dynamic Characteristics Between Virtual Synchronous Generator and Droop Control in Inverter-Based Distributed Generators". In: *IEEE Transactions on Power Electronics* 31.5 (May 2016), pp. 3600–3611. ISSN: 1941-0107. DOI: 10.1109/TPEL.2015.2465852.

[38] Toshinobu Shintai, Yushi Miura, and Toshifumi Ise. "Oscillation Damping of a Distributed Generator Using a Virtual Synchronous Generator". In: *IEEE Transactions on Power Delivery* 29.2 (Apr. 2014), pp. 668–676. ISSN: 1937-4208. DOI: 10.1109/TPWRD.2013.2281359.

[39] Ralf Hesse, Hans-Peter Beck, and Dirk Turschner. "Conditioning device for energy supply networks". Pat. WO2009022198A2. Technische Universität Clausthal. Feb. 19, 2009.

[40] H. Beck and R. Hesse. "Virtual synchronous machine". In: 2007 9th International Conference on Electrical Power Quality and Utilisation. Oct. 2007, pp. 1–6. DOI: 10.1109/EPQU.2007.4424220.

[41] Ralf Hesse, Dirk Turschner, and Hans-Peter Beck. "Micro grid stabilization using the virtual synchronous machine (VISMA)". In: *Renewable Energy and Power Quality Journal* 1.7 (Apr. 2009), pp. 676–681. ISSN: 2172038X. DOI: 10.24084/repqj07.472.

[42] Yong Chen et al. "Dynamic properties of the virtual synchronous machine (VISMA)". In: *Renewable Energy and Power Quality Journal* (May 2011), pp. 755–759. ISSN: 2172038X, 2172038X. DOI: 10.24084/repqj09.444.

[43] Yong Chen et al. "Improving the grid power quality using virtual synchronous machines". In: 2011 International Conference on Power Engineering, Energy and Electrical Drives (POWERENG). Malaga, Spain: IEEE, May 2011, pp. 1–6. ISBN: 978-1-4244-9845-1. DOI: 10.1109/PowerEng.2011.6036498.

[44] Yong Chen et al. "Investigation of the Virtual Synchronous Machine in the island mode". In: 2012 3rd IEEE PES Innovative Smart Grid Technologies Europe (ISGT Europe). Berlin, Germany: IEEE, Oct. 2012, pp. 1–6. DOI: 10.1109/ISGTEurope.2012.6465648.

[45] Krishnakumar R. Vasudevan et al. "Synchronverter: A Comprehensive Review of Modifications, Stability Assessment, Applications and Future Perspectives". In: *IEEE Access* 8 (2020), pp. 131565–131589. ISSN: 2169-3536. DOI: 10.1109/ACCESS.2020.3010001.

[46] George Weiss and Vivek Natarajan. "Modifications to the synchronverter algorithm to improve its stability and performance". In: 2017 International Symposium on Power Electronics (Ee). Novi Sad: IEEE, Oct. 2017, pp. 1–6. ISBN: 978-1-5386-3502-5. DOI: 10.1109/PEE.2017.8171684.

[47] Moshe Blau and George Weiss. "Synchronverters used for damping inter-area oscillations in two-area power systems". In: *Renewable Energy and Power Quality Journal* (Apr. 2018), pp. 45–50. ISSN: 2172038X. DOI: 10.24084/repqj16.209.

[48] Zhikang Shuai et al. "Characteristics and Restraining Method of Fast Transient Inrush Fault Currents in Synchronverters". In: *IEEE Transactions on Industrial Electronics* 64.9 (Sept. 2017), pp. 7487–7497. ISSN: 0278-0046, 1557-9948. DOI: 10.1109/TIE.2017.2652362.

[49] Javier Roldán-Pérez, Alberto Rodríguez-Cabero, and Milan Prodanovic. "Parallel current-controlled synchronverters for voltage and frequency regulation in weak grids". In: *The Journal of Engineering* 2019.17 (June 1, 2019), pp. 3516–3520. ISSN: 2051-3305. DOI: 10.1049/joe.2018.8218.

[50] Shuan Dong, Yongning Chi, and Yan Li. "Active Voltage Feedback Control for Hybrid Multiterminal HVDC System Adopting Improved Synchronverters". In: *IEEE Transactions on Power Delivery* 31.2 (Apr. 2016), pp. 445–455. ISSN: 0885-8977, 1937-4208. DOI: 10.1109/TPWRD.2015.2420657.

[51] Pedro Rodriguez Cortés et al. "Synchronous power controller for a generating system based on static power converters". Pat. WO2012117131A1. S.A. Abengoa Solar New Technologies. Sept. 7, 2012.

[52] Pedro Rodriguez Cortés et al. "Virtual admittance controller based on static power converters". Pat. WO2012117133A1. Abengoa Solar New Technologies S.A. Sept. 7, 2012.

[53] Pedro Rodriguez Cortés et al. "Virtual controller of electromechanical characteristics for static power cnverters". Pat. WO2012117132A1. S.A. Abengoa Solar New Technologies. Sept. 7, 2012.

[54] P. Rodriguez, I. Candela, and A. Luna. "Control of PV generation systems using the synchronous power controller". In: 2013 IEEE Energy Conversion Congress and Exposition. Sept. 2013, pp. 993–998. DOI: 10.1109/ECCE.2013.6646811.

[55] Weiyi Zhang et al. "An active power synchronizing controller for grid-connected power converters with configurable natural droop characteristics". In: 2015 IEEE 6th International Symposium on Power Electronics for Distributed Generation Systems (PEDG). June 2015, pp. 1–7. DOI: 10.1109/PEDG.2015.7223055.

[56] Weiyi Zhang, Daniel Remon, and Pedro Rodriguez. "Frequency support characteristics of grid-interactive power converters based on the synchronous power controller". In: *IET Renewable Power Generation* 11.4 (2017), pp. 470–479. ISSN: 1752-1424. DOI: 10.1049/iet-rpg.2016.0557.

[57] P. Rodríguez et al. "Flexible Grid Connection and Islanding of SPC-Based PV Power Converters". In: *IEEE Transactions on Industry Applications* 54.3 (May 2018), pp. 2690–2702. ISSN: 0093-9994. DOI: 10.1109/TIA.2018.2800683.

[58] Weiyi Zhang et al. "Frequency Support Properties of the Synchronous Power Control for Grid-Connected Converters". In: *IEEE Transactions on Industry Applications* 55.5 (Sept. 2019), pp. 5178–5189. ISSN: 1939-9367. DOI: 10.1109/TIA.2019.2928517.

[59] Yuko Hirase et al. “A grid-connected inverter with virtual synchronous generator model of algebraic type”. In: *Electrical Engineering in Japan* 184.4 (Sept. 2013), pp. 10–21. ISSN: 04247760. DOI: 10.1002/eej.22428.

[60] Yuko Hirase et al. “Analysis of Resonance in Microgrids and Effects of System Frequency Stabilization Using a Virtual Synchronous Generator”. In: *IEEE Journal of Emerging and Selected Topics in Power Electronics* 4.4 (Dec. 2016), pp. 1287–1298. ISSN: 2168-6785. DOI: 10.1109/JESTPE.2016.2581818.

[61] J. Driesen and K. Visscher. “Virtual synchronous generators”. In: 2008 IEEE Power and Energy Society General Meeting - Conversion and Delivery of Electrical Energy in the 21st Century. July 2008, pp. 1–3. DOI: 10.1109/PES.2008.4596800.

[62] M. P. N. van Wesenbeeck et al. “Grid tied converter with virtual kinetic storage”. In: 2009 IEEE Bucharest PowerTech. June 2009, pp. 1–7. DOI: 10.1109/PTC.2009.5282048.

[63] Mihaela Albu et al. “Storage selection for DG applications containing virtual synchronous generators”. In: 2009 IEEE Bucharest PowerTech (POWERTECH). Bucharest, Romania: IEEE, June 2009, pp. 1–6. ISBN: 978-1-4244-2234-0. DOI: 10.1109/PTC.2009.5281969.

[64] Tom Loix et al. “Layout and performance of the power electronic converter platform for the VSYNC project”. In: 2009 IEEE Bucharest PowerTech (POWERTECH). Bucharest, Romania: IEEE, June 2009, pp. 1–8. ISBN: 978-1-4244-2234-0. DOI: 10.1109/PTC.2009.5282160.

[65] Vu Van Thong et al. “Virtual synchronous generator: Laboratory scale results and field demonstration”. In: 2009 IEEE Bucharest PowerTech (POWERTECH). Bucharest, Romania: IEEE, June 2009, pp. 1–6. ISBN: 978-1-4244-2234-0. DOI: 10.1109/PTC.2009.5281790.

[66] T. Vu Van et al. “Virtual synchronous generator: An element of future grids”. In: 2010 IEEE PES Innovative Smart Grid Technologies Conference Europe (ISGT Europe). Gothenburg, Sweden: IEEE, Oct. 2010, pp. 1–7. ISBN: 978-1-4244-8508-6. DOI: 10.1109/ISGTEUROPE.2010.5638946.

[67] Salvatore D’Arco, Jon Are Suul, and Olav B. Fosso. “Control system tuning and stability analysis of Virtual Synchronous Machines”. In: 2013 IEEE Energy Conversion Congress and Exposition. Sept. 2013, pp. 2664–2671. DOI: 10.1109/ECCE.2013.6647045.

[68] Salvatore D’Arco, Jon Are Suul, and Olav B. Fosso. “Small-signal modeling and parametric sensitivity of a virtual synchronous machine in islanded operation”. In: *International Journal of Electrical Power & Energy Systems* 72 (Nov. 1, 2015), pp. 3–15. ISSN: 0142-0615. DOI: 10.1016/j.ijepes.2015.02.005.

[69] Salvatore D'Arco, Jon Are Suul, and Olav B. Fosso. "A Virtual Synchronous Machine implementation for distributed control of power converters in SmartGrids". In: *Electric Power Systems Research* 122 (May 1, 2015), pp. 180–197. ISSN: 0378-7796. DOI: 10.1016/j.epsr.2015.01.001.

[70] Olve Mo, Salvatore D'Arco, and Jon Are Suul. "Evaluation of Virtual Synchronous Machines With Dynamic or Quasi-Stationary Machine Models". In: *IEEE Transactions on Industrial Electronics* 64.7 (July 2017), pp. 5952–5962. ISSN: 1557-9948. DOI: 10.1109/TIE.2016.2638810.

[71] Ujjwol Tamrakar et al. "Virtual Inertia: Current Trends and Future Directions". In: *Applied Sciences* 7.7 (July 2017), p. 654. DOI: 10.3390/app7070654.

[72] Meng Chen, Dao Zhou, and Frede Blaabjerg. "Modelling, Implementation, and Assessment of Virtual Synchronous Generator in Power Systems". In: *Journal of Modern Power Systems and Clean Energy* 8.3 (May 2020), pp. 399–411. ISSN: 2196-5420. DOI: 10.35833/MPCE.2019.000592.

[73] Hasan Alrajhi Alsiraji and Ramadan El-Shatshat. "Comprehensive assessment of virtual synchronous machine based voltage source converter controllers". In: *Transmission Distribution IET Generation* 11.7 (2017). Number: 7, pp. 1762–1769. ISSN: 1751-8695. DOI: 10.1049/iet-gtd.2016.1423.

[74] Wenhua Wu et al. "Sequence-Impedance-Based Stability Comparison Between VSGs and Traditional Grid-Connected Inverters". In: *IEEE Transactions on Power Electronics* 34.1 (Jan. 2019), pp. 46–52. ISSN: 0885-8993, 1941-0107. DOI: 10.1109/TPEL.2018.2841371.

[75] Wenhua Wu et al. "Sequence Impedance Modeling and Stability Comparative Analysis of Voltage-Controlled VSGs and Current-Controlled VSGs". In: *IEEE Transactions on Industrial Electronics* 66.8 (Aug. 2019), pp. 6460–6472. ISSN: 0278-0046, 1557-9948. DOI: 10.1109/TIE.2018.2873523.

[76] Qing-Chang Zhong and George Weiss. "Static synchronous generators for distributed generation and renewable energy". In: 2009 IEEE/PES Power Systems Conference and Exposition (PSCE). Seattle, WA, USA: IEEE, Mar. 2009, pp. 1–6. ISBN: 978-1-4244-3810-5. DOI: 10.1109/PSCE.2009.4840013.

[77] Vivek Natarajan and George Weiss. "Synchronverters With Better Stability Due to Virtual Inductors, Virtual Capacitors, and Anti-Windup". In: *IEEE Transactions on Industrial Electronics* 64.7 (July 2017), pp. 5994–6004. ISSN: 1557-9948. DOI: 10.1109/TIE.2017.2674611.

[78] Hui Li et al. "A New Power Decoupling Control Strategy of Synchronverter Based on Current Feedback". In: *DEStech Transactions on Environment, Energy and Earth Sciences* (appeec June 26, 2018). ISSN: 2475-8833. DOI: 10.12783/dteees/appeec2018/23515.

[79] Yang Li, Rong Qi, and Shan Wang. "New Control Schemes of Output Power Decoupling Based on Synchronverter". In: 2018 21st International Conference on Electrical Machines and Systems (ICEMS). Jeju: IEEE, Oct. 2018, pp. 1980–1985. ISBN: 978-89-86510-20-1. DOI: 10.23919/ICEMS.2018.8549241.

[80] Shuan Dong and Yu Christine Chen. "Adjusting Synchronverter Dynamic Response Speed via Damping Correction Loop". In: *IEEE Transactions on Energy Conversion* 32.2 (June 2017), pp. 608–619. ISSN: 0885-8969, 1558-0059. DOI: 10.1109/TEC.2016.2645450.

[81] Hassan Bevrani, Toshifumi Ise, and Yushi Miura. "Virtual synchronous generators: A survey and new perspectives". In: *International Journal of Electrical Power & Energy Systems* 54 (Jan. 1, 2014), pp. 244–254. ISSN: 0142-0615. DOI: 10.1016/j.ijepes.2013.07.009.

[82] Fabio Mandrile, Enrico Carpaneto, and Radu Bojoi. "Grid-Tied Inverter with Simplified Virtual Synchronous Compensator for Grid Services and Grid Support". In: 2019 IEEE Energy Conversion Congress and Exposition (ECCE). Sept. 2019, pp. 4317–4323. DOI: 10.1109/ECCE.2019.8912266.

[83] Fabio Mandrile, Enrico Carpaneto, and Radu Bojoi. "VSG Simplified Damper Winding: Design Guidelines". In: IECON 2019 - 45th Annual Conference of the IEEE Industrial Electronics Society. Vol. 1. Oct. 2019, pp. 3962–3967. DOI: 10.1109/IECON.2019.8926981.

[84] Fabio Mandrile, Enrico Carpaneto, and Radu Bojoi. "Virtual Synchronous Generator with Simplified Single-Axis Damper Winding". In: 2019 IEEE 28th International Symposium on Industrial Electronics (ISIE). June 2019, pp. 2123–2128. DOI: 10.1109/ISIE.2019.8781233.

[85] Fabio Mandrile, Enrico Carpaneto, and Radu Bojoi. "Grid-Feeding Inverter with Simplified Virtual Synchronous Compensator Providing Grid Services and Grid Support". In: *IEEE Transactions on Industry Applications* (2020). Early Access. ISSN: 0093-9994, 1939-9367. DOI: 10.1109/TIA.2020.3028334.

[86] Fabio Mandrile et al. "Simple Tuning Method of Virtual Synchronous Generators Reactive Control". In: *2020 IEEE Energy Conversion Congress and Exposition (ECCE)*. In press. Detroit, MI, USA, 2020.

[87] D. Grahame Holmes and Thomas A. Lipo. *Pulse width modulation for power converters: principles and practice*. IEEE Press series on power engineering. Piscataway, NJ: IEEE Press, 2003. 724 pp. ISBN: 978-0-471-20814-3.

[88] X. Yan and S. Y. A. Mohamed. "Comparison of virtual synchronous generators dynamic responses". In: 2018 IEEE 12th International Conference on Compatibility, Power Electronics and Power Engineering (CPE-POWERENG 2018). Apr. 2018, pp. 1–6. DOI: 10.1109/CPE.2018.8372573.

[89] L. Asiminoaei et al. “Implementation and Test of an Online Embedded Grid Impedance Estimation Technique for PV Inverters”. In: *IEEE Transactions on Industrial Electronics* 52.4 (Aug. 2005). Number: 4, pp. 1136–1144. ISSN: 0278-0046. DOI: 10.1109/TIE.2005.851604.

[90] Tomi Roinila and Tuomas Messo. “Online Grid-Impedance Measurement Using Ternary-Sequence Injection”. In: *IEEE Transactions on Industry Applications* 54.5 (Sept. 2018), pp. 5097–5103. ISSN: 0093-9994, 1939-9367. DOI: 10.1109/TIA.2018.2825938.

[91] Adrian V. Timbus et al. “Line Impedance Estimation Using Active and Reactive Power Variations”. In: 2007 IEEE Power Electronics Specialists Conference. Orlando, FL, USA: IEEE, 2007, pp. 1273–1279. ISBN: 978-1-4244-0654-8. DOI: 10.1109/PESC.2007.4342176.

[92] Ana Vidal et al. “A Method for Identification of the Equivalent Inductance and Resistance in the Plant Model of Current-Controlled Grid-Tied Converters”. In: *IEEE Transactions on Power Electronics* 30.12 (Dec. 2015). Number: 12, pp. 7245–7261. ISSN: 0885-8993, 1941-0107. DOI: 10.1109/TPEL.2015.2395817.

[93] Jarno Kukkola, Mikko Routimo, and Marko Hinkkanen. “Real-Time Grid Impedance Estimation Using a Converter”. In: 2019 IEEE Energy Conversion Congress and Exposition (ECCE). Baltimore, MD, USA: IEEE, Sept. 2019, pp. 6005–6012. ISBN: 978-1-72810-395-2. DOI: 10.1109/ECCE.2019.8912681.

[94] Qing Liu, Tommaso Caldognetto, and Simone Buso. “Review and Comparison of Grid-Tied Inverter Controllers in Microgrids”. In: *IEEE Transactions on Power Electronics* 35.7 (July 2020), pp. 7624–7639. ISSN: 1941-0107. DOI: 10.1109/TPEL.2019.2957975.

[95] R. I. Bojoi et al. “Current control strategy for power conditioners using sinusoidal signal integrators in synchronous reference frame”. In: *IEEE Transactions on Power Electronics* 20.6 (Nov. 2005), pp. 1402–1412. ISSN: 0885-8993. DOI: 10.1109/TPEL.2005.857558.

[96] E. Mollerstedt and B. Bernhardsson. “Out of control because of harmonics-an analysis of the harmonic response of an inverter locomotive”. In: *IEEE Control Systems Magazine* 20.4 (Aug. 2000), pp. 70–81. ISSN: 1066-033X. DOI: 10.1109/37.856180.

[97] E. A. A. Coelho, P. C. Cortizo, and P. F. D. Garcia. “Small-signal stability for parallel-connected inverters in stand-alone AC supply systems”. In: *IEEE Transactions on Industry Applications* 38.2 (Mar. 2002), pp. 533–542. ISSN: 0093-9994. DOI: 10.1109/28.993176.

[98] J. L. Agorreta et al. "Modeling and Control of N-Paralleled Grid-Connected Inverters With LCL Filter Coupled Due to Grid Impedance in PV Plants". In: *IEEE Transactions on Power Electronics* 26.3 (Mar. 2011). Number: 3, pp. 770–785. DOI: 10.1109/TPEL.2010.2095429.

[99] Nathaniel Bottrell, Milan Prodanovic, and Timothy C. Green. "Dynamic Stability of a Microgrid With an Active Load". In: *IEEE Transactions on Power Electronics* 28.11 (Nov. 2013), pp. 5107–5119. ISSN: 0885-8993, 1941-0107. DOI: 10.1109/TPEL.2013.2241455.

[100] Fabio Mandrile et al. "State-Space Modeling Techniques of Emerging Grid-Connected Converters". In: *Energies* 13.18 (Sept. 15, 2020), p. 4824. ISSN: 1996-1073. DOI: 10.3390/en13184824.

[101] X. Wang and F. Blaabjerg. "Harmonic Stability in Power Electronic-Based Power Systems: Concept, Modeling, and Analysis". In: *IEEE Transactions on Smart Grid* 10.3 (May 2019). Number: 3, pp. 2858–2870. ISSN: 1949-3053. DOI: 10.1109/TSG.2018.2812712.

[102] J. Sun. "Small-Signal Methods for AC Distributed Power Systems–A Review". In: *IEEE Transactions on Power Electronics* 24.11 (Nov. 2009), pp. 2545–2554. ISSN: 0885-8993. DOI: 10.1109/TPEL.2009.2029859.

[103] J. Sun. "Impedance-Based Stability Criterion for Grid-Connected Inverters". In: *IEEE Transactions on Power Electronics* 26.11 (Nov. 2011), pp. 3075–3078. ISSN: 0885-8993. DOI: 10.1109/TPEL.2011.2136439.

[104] X. Wang, F. Blaabjerg, and W. Wu. "Modeling and Analysis of Harmonic Stability in an AC Power-Electronics-Based Power System". In: *IEEE Transactions on Power Electronics* 29.12 (Dec. 2014). Number: 12, pp. 6421–6432. ISSN: 0885-8993. DOI: 10.1109/TPEL.2014.2306432.

[105] X. Wang, L. Harnefors, and F. Blaabjerg. "Unified Impedance Model of Grid-Connected Voltage-Source Converters". In: *IEEE Transactions on Power Electronics* 33.2 (Feb. 2018). Number: 2, pp. 1775–1787. ISSN: 0885-8993. DOI: 10.1109/TPEL.2017.2684906.

[106] B. Wen et al. "Analysis of D-Q Small-Signal Impedance of Grid-Tied Inverters". In: *IEEE Transactions on Power Electronics* 31.1 (Jan. 2016). Number: 1, pp. 675–687. ISSN: 0885-8993. DOI: 10.1109/TPEL.2015.2398192.

[107] Huakun Liu, Xiaorong Xie, and Wei Liu. "An Oscillatory Stability Criterion Based on the Unified dq -Frame Impedance Network Model for Power Systems With High-Penetration Renewables". In: *IEEE Transactions on Power Systems* 33.3 (May 2018), pp. 3472–3485. ISSN: 0885-8950, 1558-0679. DOI: 10.1109/TPWRS.2018.2794067.

[108] G. Francis et al. "An algorithm and implementation system for measuring impedance in the D-Q domain". In: 2011 IEEE Energy Conversion Congress and Exposition. Sept. 2011, pp. 3221–3228. DOI: 10.1109/ECCE.2011.6064203.

[109] Mohamed Belkhayat. "Stability criteria for AC power systems with regulated loads". PhD thesis. Purdue University, Jan. 1, 1997. 121 pp.

[110] J. M. Uudrill. "Dynamic Stability Calculations for an Arbitrary Number of Interconnected Synchronous Machines". In: *IEEE Transactions on Power Apparatus and Systems* PAS-87.3 (Mar. 1968). Number: 3, pp. 835–844. ISSN: 0018-9510. DOI: 10.1109/TPAS.1968.292199.

[111] G. Gaba, S. Lefebvre, and D. Mukhedkar. "Comparative analysis and study of the dynamic stability of AC/DC systems". In: *IEEE Transactions on Power Systems* 3.3 (Aug. 1988), pp. 978–985. ISSN: 0885-8950, 1558-0679. DOI: 10.1109/59.14550.

[112] S. Arabi et al. "Small signal stability program analysis of SVC and HVDC in AC power systems". In: *IEEE Transactions on Power Systems* 6.3 (Aug. 1991). Number: 3, pp. 1147–1153. ISSN: 08858950. DOI: 10.1109/59.119259.

[113] Peng Hou et al. "Harmonic stability analysis of offshore wind farm with component connection method". In: *IECON 2017 - 43rd Annual Conference of the IEEE Industrial Electronics Society*. IECON 2017 - 43rd Annual Conference of the IEEE Industrial Electronics Society. Beijing: IEEE, Oct. 2017, pp. 4926–4932. ISBN: 978-1-5386-1127-2. DOI: 10.1109/IECON.2017.8216850.

[114] Yanbo Wang. "Stability Assessment of Inverter-Fed Power System". PhD thesis. Aalborg, Denmark: Aalborg University, 2017.

[115] Roberto Rosso, Soenke Engelken, and Marco Liserre. "Analysis of the Behavior of Synchronverters Operating in Parallel by Means of Component Connection Method (CCM)". In: 2018 IEEE Energy Conversion Congress and Exposition (ECCE). Portland, OR: IEEE, Sept. 2018, pp. 2228–2235. ISBN: 978-1-4799-7312-5. DOI: 10.1109/ECCE.2018.8558426.

[116] Roberto Rosso, Soenke Engelken, and Marco Liserre. "Analysis of the Parallel Operation Between Synchronverters and PLL-Based Converters". In: 2019 IEEE Energy Conversion Congress and Exposition (ECCE). Baltimore, MD, USA: IEEE, Sept. 2019, pp. 2583–2590. ISBN: 978-1-72810-395-2. DOI: 10.1109/ECCE.2019.8912996.

[117] Roberto Rosso, Soenke Engelken, and Marco Liserre. "Robust Stability Investigation of the Interactions Among Grid-Forming and Grid-Following Converters". In: *IEEE Journal of Emerging and Selected Topics in Power Electronics* 8.2 (June 2020), pp. 991–1003. ISSN: 2168-6777, 2168-6785. DOI: 10.1109/JESTPE.2019.2951091.

[118] Robert Dimitrovski et al. “Comprehensive computer program for SSTI analysis of AC/DC power systems based on the component connection method”. In: *International Journal of Electrical Power & Energy Systems* 111 (Oct. 2019), pp. 508–516. ISSN: 01420615. DOI: 10.1016/j.ijepes.2019.04.024.

[119] Philip C. Kjaer et al. “Comparison of Experiences with Wind Power Plants with Low SCR”. In: IEEE PES General Meeting. Technical Panel. Denver, CO, USA, 2015.

This Ph.D. thesis has been typeset by means of the TEX-system facilities. The typesetting engine was pdfLATEX. The document class was `toptesi`, by Claudio Beccari, with option `tipotesi =scudo`. This class is available in every up-to-date and complete TEX-system installation.